LHCb-PUB-2016-007
March 9, 2016

Study of prototype sensors for the Upstream Tracker Upgrade

A. Abba[8], M. Artuso[2], S. Blusk[2], A. Bursche[5], A. Davis[3], A. Dendek[4], B. Dey[5], S. Ely[2], D. Forshaw[2], J. Fu[1], M. Kelsey[2], F. Lionetto[5], P. Manning[2], R. Mountain[2], N. Neri[1], A.Papula[7], M. Petruzzo[1], M. Pikies[4], M. Rudolph[2], M. Sokoloff[3], S. Stone[2], T. Szumlak[4], J. C. Wang[2]

[1] *Instituto Nazionale di Fisica Nucleare - Sezione di Milano, Italy*
[2] *Syracuse University, Syracuse, NY USA*
[3] *University of Cincinnati, Cincinnati, OH USA*
[4] *AGH - University of Science and Technology, Faculty of Physics and Applied Computer Science, Kraków, Poland*
[5] *Physik-Institut, Universität Zürich, Zürich, Switzerland*
[6] *European Organization for Nuclear Research (CERN), Geneva, Switzerland*
[7] *Massachusetts Institute of Technology, Cambridge, MA USA*
[8] *Nuclear Instruments srl, IT-22045 Lumbrugo (CO), Italy*

Abstract

Three testbeams were carried out in 2015 to test the performance of prototype sensors for the Upstream Tracker. Two of the testbeams were devoted to studying full size n-in-p sensors, and one was devoted to testing mini-sensors, all from Hamamatsu. Results on the performance of these Upstream Tracker sensor prototypes are presented.

Contents

1 Introduction

The Upstream Tracker (UT) detector is a key part of the LHCb Upgrade, replacing the current TT stations. A detailed description of the UT is given in the Technical Design Report [1]. The UT detector consists of four silicon planes, each about 1.53 m in width and 1.34 m in height. Each plane is composed of 1.5 m long *staves* that are tiled with ~10 cm x 10 cm silicon wafers. Consecutive wafers are mounted on opposite sides of the stave to ensure no gaps along the height, and adjacent staves are also overlapped to ensure no gaps in the horizontal direction. A cartoon of the UT detector is shown in Fig. 1. The majority of the detector area utilizes sensors with an approximate pitch of 190 μm, however the inner region features sensors with half the pitch (95 μm) to cope with higher occupancy. Both n-in-p and p-in-n technologies are being considered for the outer region, but for the inner region, only n-in-p sensors are being considered due to better radiation hardness.

In the innermost region of UT (radius of 34.2 mm) the maximum fluence expected for the sensors, according to the simulation, is $1.4 \times 10^{14} n_{eq} cm^{-2}$, corresponding to about 12 MRad. To allow for a safety margin, we assume a maximum fluence of $\sim 4 \times 10^{14} n_{eq} cm^{-2}$, or about 40 MRad.

1.1 Brief review of 2014 testbeam results

Micron mini-sensors (250 µm thick and $\sim$ 1 cm^2 $\times$ 1 cm^2) were tested in 2014 with integrated fluences up to 4×10^{14} $\mathrm{n_{eq}}$ cm^{-2}, which corresponds to the expected maximum fluence, as described above [2]. Six n-in-p and 1 p-in-n sensors were tested at the SPS, using the TPIX telescope to provide a precise measurement of the beam particles' trajectories. The DAQ readout was based on the Alibava system [3–5], which was replaced for the 2015 testbeam campaigns, as will be described later.

The key results of the testbeam were that there is a gradual loss in charge collection efficiency (CCE) between zero dose and 4×10^{14} n_{eq} cm^{-2} of about 15%. The signal-to-noise (S/N) dropped from about 22 to about 19 for these 250 µm thick n-in-p sensors (see Figs. 10 and 12 in Ref [2]). A large part of this loss occurs in the middle of two strips (see Fig. 15 in Ref [2]).

1.2 Goals of the 2015 testbeam campaign

The sensors tested in 2014 were mini-sensors fabricated by Micron Semiconductors, not full-length UT sensors. The goal of the 2015 testbeams was to test key features of the full-length sensors, fabricated by Hamamatsu, as well as perform additional tests using mini-sensors. In particular, the aims were to

- Measure the CCE of Type A sensors using two different styles of embedded pitch adapter;
- Characterize the CCE of a D-type sensor at the maximum expected fluence, and compare to zero or low fluence;
- Characterize the CCE of the D-type sensors near the 1/4-circle cutout region that surrounds the LHCb beampipe.
- Characterize and compare topside versus backside biasing of the sensors.

Note that measurements of the position resolution, cluster sizes, etc were not a primary goal of these testbeams. Three UT testbeams were carried out in 2015, each about 1 week

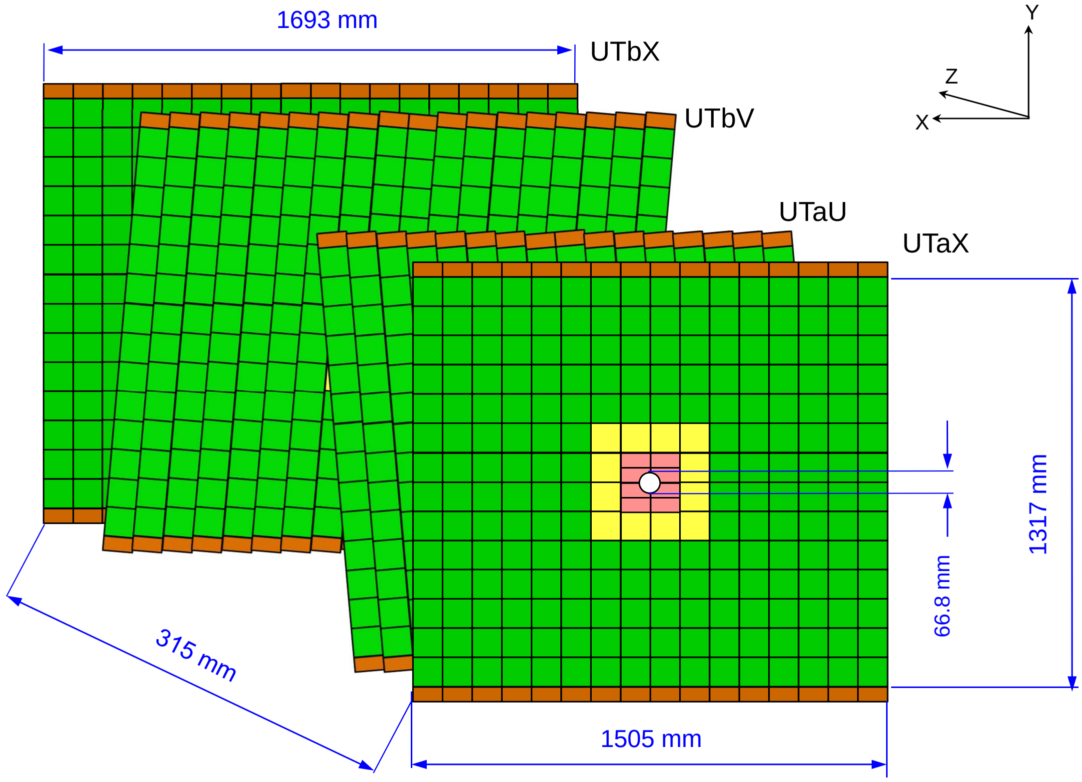

Figure 1: Cartoon showing the layout and dimensions of the four UT planes.

long. One was in July, a second in October, and a third in November. The July and October testbeams were aimed at studying the first three of these items using full length sensors. The November testbeam was used to perform studies relevant to the last item in the bullet list, using mini-sensors.

2 Experimental setup

2.1 Sensors

Pre-prototype sensors of type A and D were ordered from Hamamatsu, all in n-in-p technology. The sensors were designed to be 250 μm thick, but due to a manufacturing error at Hamamatsu, the delivered sensors were only 200 μm thick. While they acknowledged the error, and agreed to replace them at no cost to us, the replacements would come too late to make use of them in the July 2015 testbeam. The baseline design calls for 250 μm thick, 95 μm pitch D-type and 320 μm thick, 190 μm pitch A-type sensors. Due to the need to get early feedback on the sensor designs, we decided to move forward with testbeams to test the 200 μm thick sensors. This means we must correct the charge detected by factors of 1.25[1] for D-type and 1.60[2] for A-type to estimate what we expect in sensors with the correct thickness.

The A-type sensors are *half-width*, which we refer to as Type 1/2A. Instead of a 10 cm × 10 cm, 512-strip sensor, a 256-strip, 5 cm wide by 10 cm long sensor was designed. A cartoon of the Type 1/2-A sensor is shown in Fig. 2.

In order to match the pitch of the pads on the UT readout electronics ASIC (SALT ASIC), the 190 μm strip pitch of the Type A needs to be fanned down to 75 μm. Two different style of embedded PAs were designed to accomplish this. They are referred to as *FanUp* and *FanIn*. These two styles of pitch adapters are on opposite sides of the Type 1/2A sensor, as shown in Fig. 2. For the FanUp PA, there is an extra ∼500 μm inactive area where the signals are fanned in. That is, the second metal layer is outside the active area of the sensor. For the FanIn, the strips come closer to the edge of the sensor, and the 75 μm bond pads are in the active area. Therefore, the second metal layer overlaps the n-strips within the active area. The sensors also have bond pads on the 190 μm strips. In our tests, we had modules prepared that had connections made to the FanUp and FanIn PAs, as well as two where the connection was made directly to the 190 μm strips, in order to compare these different configurations.

Type D sensors are those that are closest to the beam pipe region, and have a 1/4-circle cutout in order to get as close to the beam pipe as possible to maximize the tracking acceptance. Because of the higher track density in the forward region, these sensors have a finer pitch of 95 μm and the strips are only half as long (5 cm, instead of 10 cm). A cartoon of the D-type sensor is shown in Fig. 3.

Replacement Hamamatsu sensors of the correct 250 μm thickness were received in July

[1]This is the ratio of 250 μm to 200 μm.
[2]This is the ratio of 320 μm to 200 μm.

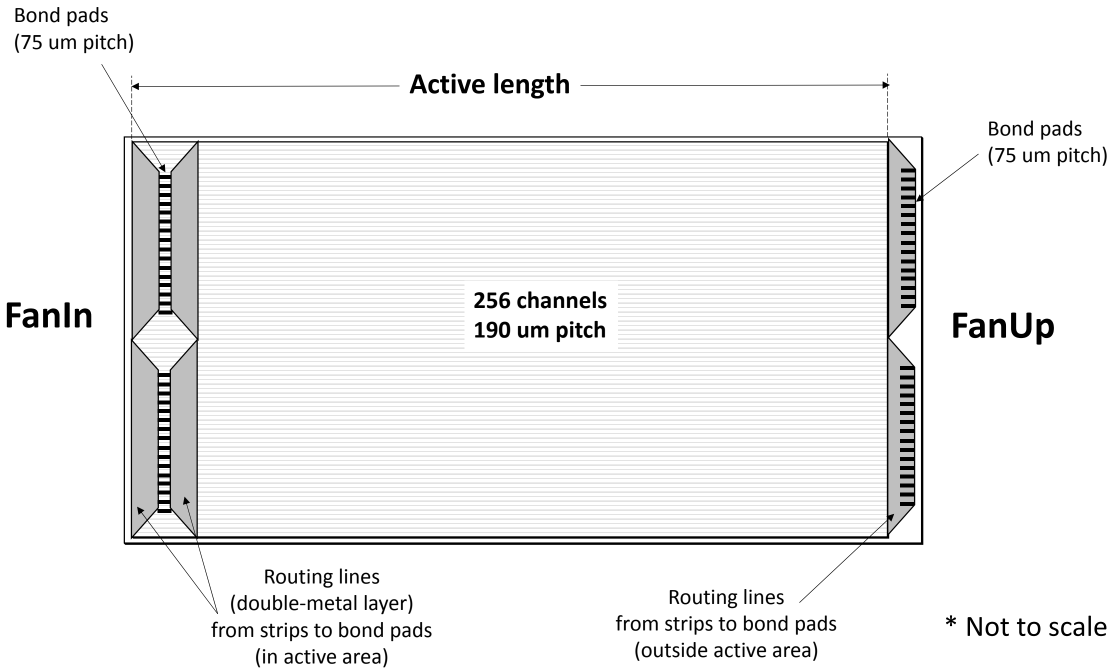

Figure 2: Cartoon of a Type 1/2 A sensor used in the 2015 testbeams.

2015, certainly too late to be used in the July 2015 testbeam. We decided though to test the mini-sensors that came with this shipment in the November testbeam with the specific aim of comparing the performance of sensors biased via the topside contact versus ones biased directly from the backside. In the topside biasing scheme, the sensor bias is brought to the sensor by wirebonding to a topside contact, and then the bias is brought to the backside by having a conducting side edge of the sensor. In this case, the back side of the sensor is passivated with a thin insulating layer, such as SiO_2, to protect the backside surface. In the backside biasing scheme, the back side of the detector is not passivated, so a conducting contact can be made directly to the back side of the detector. However, in this case, this HV plane is completely exposed, and can be more easily damaged in handling. Moreover, one must ensure that this larger area does not come near any other conducting surfaces that are at a different voltage. The topside biasing is the favored way to bring in the bias for UT, but there was concern expressed in the silicon EDR review that this biasing scheme be adequately tested.

The sensors that were tested in the three testbeams are summarized in Table 1. All of them were irradiated at the IRRAD facility at CERN, as described in the next section. Also, note that in the TimePix telescope, there were two stages, one in the middle of the telescope between the two halves and one in the back, as discussed below. The pointing

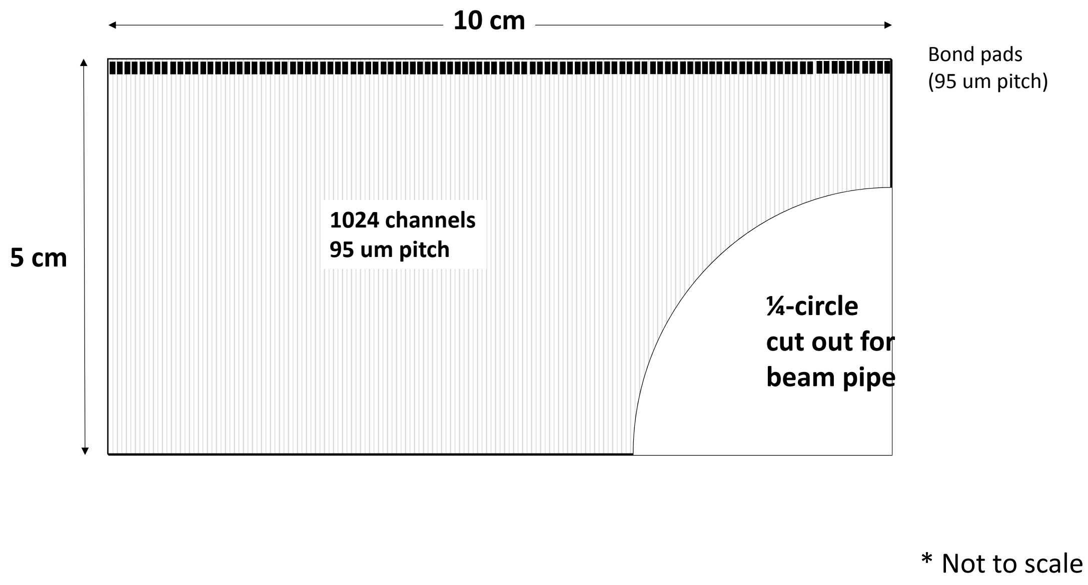

Figure 3: Cartoon of a Type D sensor used in the 2015 testbeams.

resolution is better when in the middle (MID) than in the back (BACK).

2.2 Sensor Irradiation

All sensors tested in the 2015 testbeams were irradiated at the IRRAD facility at CERN in June (Type 1/2 A and D sensors) and October (mini-sensors) of 2015 (see Tables 1 and 4). The IRRAD facility delivers 24 GeV/c protons from the proton synchrotron (PS) in "spills" of approximately 3.5×10^{11} protons every 12 seconds with a beam profile that is Gaussian in two dimensions and has a FWHM of 12x12 mm^2. A more detailed description of the IRRAD facility at CERN can be obtained at their website [6].

Hamamatsu mini-sensors were irradiated up to four fluences: 1.1×10^{14}, 6.4×10^{14}, 1.36×10^{15}, and 2.1×10^{15} n_{eq}/cm^2. Only mini-sensors irradiated to the first two fluences were tested in the 2015 testbeams, where the rest were tested in the laboratory. Individual doses were measured by placing 10x10 mm^2 aluminum foils with the sensors during irradiation and subsequently measuring the activation levels. The relative uncertainty of each fluence is $\pm 7\%$. In addition to Hamamatsu mini-sensors, 28 mini-sensors from Micron, with various technologies and geometries listed in Table 4, were irradiated to each fluence and tested in the laboratory.

Table 1: List of full size detectors tested in the 2015 testbeams. The letter in the board ID indicates if the sensor is A-type or D-type. All sensors tested are from Hamamatsu. The table is separated by test beam period (Jult, October and November). Acronyms: BP-TB = backside passivated - topside biasing, BUP-BB = backside unpassivated - backside biasing. MID = Sensor on middle stage, BACK = sensor on back stage.

Board ID	Peak Fluence (10^{14} $n_{\mathrm{eq}}/\mathrm{cm}^2$)	Comments
A4	0.33	July TB, conn. to 190 μm strips, 200 μm, MID
A6	0.33	July TB, FanIn, r/o via 75 μm embedded PA, 200 μm, MID
A9	0.0	July TB, conn. to 190 μm strips, 200 μm, MID
D7	4.6	July TB, 200 μm, BACK
D9	0.0	July TB, 200 μm, MID
D5	4.6	Oct TB, 200 μm, BACK
A8	0.33	Oct TB, FanUp, r/o via 75 μm embedded PA, 200 μm, BACK
Mini-A1-1	1.1	Nov TB, 1 cm x 1.8 cm, 250 μm, BUP-BB, MID
Mini-A1-2	1.1	Nov TB, 1 cm x 1.8 cm, 250 μm, BP-TB, MID
Mini-A2-1	6.4	Nov TB, 1 cm x 1.8 cm, 250 μm, BUP-BB, MID
Mini-A2-2	6.4	Nov TB, 1 cm x 1.8 cm, 250 μm, BP-TB, MID

Type 1/2A and full size D sensors were irradiated to a maximum fluence of 2.0×10^{13} and 4.6×10^{14} $\mathrm{n_{eq}/cm^2}$, respectively. Due to the limited size of the proton beam, these sensors were irradiated in a configuration where the strips were parallel to the beam. This allowed the full length of the sensor to be irradiated. The fluence of these sensors was again measured using activated Aluminum foils placed in with the sensors during irradiation. The Al. foils were segmented into six $5{\times}100$ mm^2 or $5{\times}50$ mm^2 strips for 1/2A and D sensors, respectively, to measure the irradiation profile across the sensors. Figure 4 shows the measured irradiation profile across the 1/2A and D type sensors in units of 1 MeV $\mathrm{n_{eq}}$ fluence. Full size type D sensors were placed in the beam such that the peak of irradiation is centered at the start of the 1/4 circular cutout (strip #672) and 1/2A sensors were positioned such that the peak of irradiation was roughly centered at channel #26 (± 5 channels), thus leaving the other side of the sensor to be used to test its unirradiated properties.

After irradiation all sensors are kept at -20 C, only warming up to room temperature during transport, laboratory measurements, and installation. Type 1/2A and D sensors, after leaving IRRAD, accumulated a total of 2.4 days of annealing at room temperature before installation. Hamamatsu mini-sensors, after leaving IRRAD, accumulated only 0.65 days of annealing at room temperature before installation. Measurements of the static properties (IV, CV, etc.) are given in Appendix A. The measured changes in leakage current in our irradiated detectors are consistent with previous measurements on Hamamatsu and Micron detectors [7].

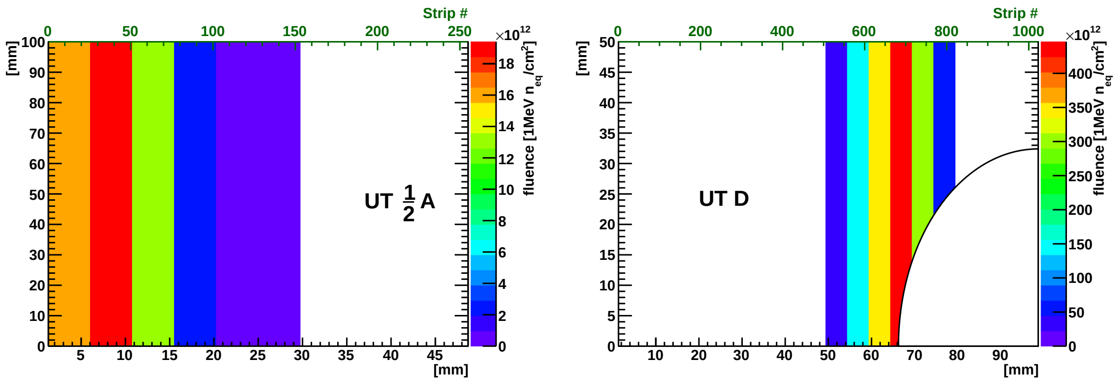

Figure 4: Measured irradiation profiles of 1/2A (left) and full size D (right) sensors, in 1 MeV n_{eq} fluence. Here the Y-axis runs parallel with the strips.

2.3 Detector mechanics

The detector module consisted of a sensor, a TT hybrid hosting 4 Beetle chips, and an adapter card, that translates the TT hybrid connector field/pinout to the one expected by the data acquisition (DAQ) system. Because the front end inputs of the Beetle chips have 40 µm pitch, an external glass pitch adapter (PA) was used to fan the signals from 40 µm pitch to either 95 µm (for the D-type sensors), or 190 µm (for the Type 1/2A). A photo of a Type D module is shown in Fig. 5.

For the Type 1/2A sensors, when reading out the detector via the 75 µm pitch sensor pads, there was a mismatch in pitch, since the glass PA had 95 µm pitch. Therefore, in these cases, the wirebonds were angled. For the Type D, and the Type A boards that were read out through direct connection to the strips, the pitches of the sensor and external PA were the same and the wirebonds were not angled.

A HV cable was directly connected to the adapter board, and the HV was routed through the connector and TT hybrid to a pad near the edge of the TT hybrid. A jumper was used to wirebond the HV from the TT hybrid to the sensor. Each board also had 1-2 RTDs to monitor the temperature of the module.

The detector was cooled by screwing the Al plate (see Fig. 5) holding the sensors against two Peltier devices (HP-199-1.4-15. from TE technology). A thin layer of thermal grease was placed between the modules and the Peltiers to reduce the thermal impedance. The Peltiers were recessed into a pair of copper blocks to efficiently transfer the heat that they generated into the block. That heat was then removed by having a copper tube passing through the blocks, which circulated a cold water/glycol mixture, provided by an external chiller. The module was placed in light-tight box which had nitrogen flowing to prevent condensation. A photograph of a module in the UT box, in the TimePix telescope is shown in Fig. 6. The UT box is mounted on a stage that can move up-down (y-axis) and left-right (x-axis), as well as provide a rotation about the y axis.

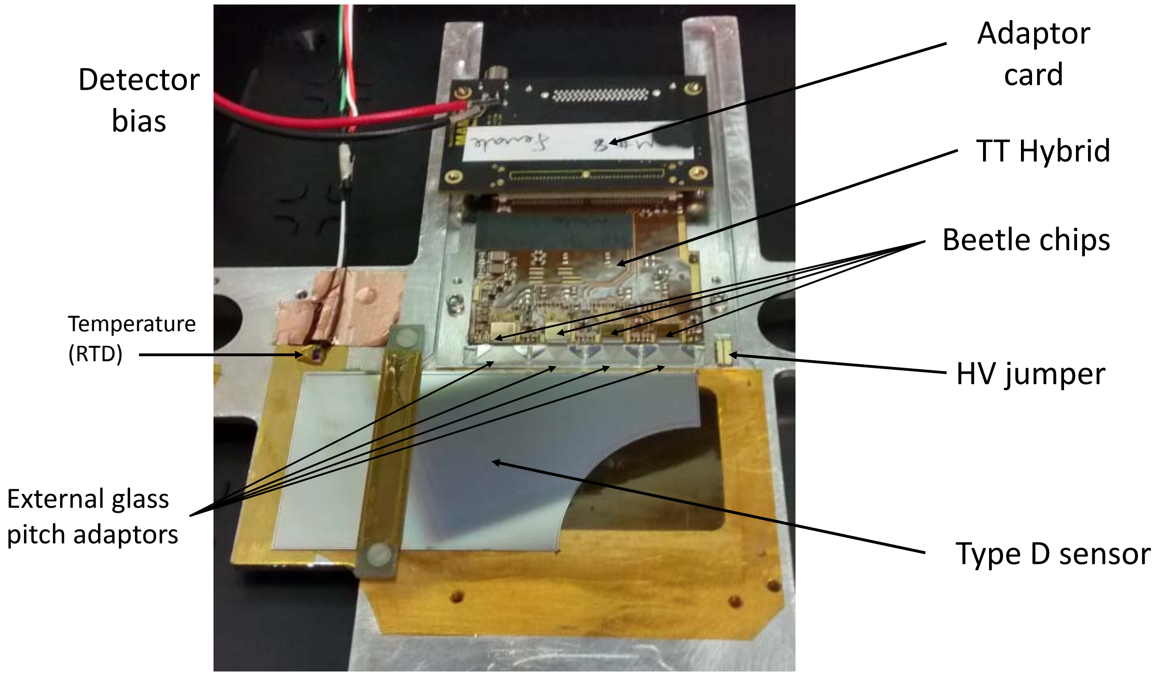

Figure 5: Photo of a Type D sensor used in the 2015 testbeams.

2.4 Data acquisition

For the 2015 testbeams, the readout and data acquisition (DAQ) were changed from an Alibava-based system to a system designed by the Milano group, in collaboration with Nuclear Instruments [8]. A detailed description of the DAQ (MAMBA DAQ) is given in Ref. [9]. The key improvements of this system over the Alibava-based system are:

- Ability to run at speeds as high as 1 MHz ;
- Ability to take an external clock (from TimePix), and timestamp each event. This allows the detector under test (DUT) and TimePix hit times to have a common clock, thus enabling the events to be more robustly matched offline;
- The ability to customize the firmware and software as needed;
- The ability to read out multiple Beetle chips, and even multiple hybrids, with a single MAMBA board, if needed.

A trigger was formed by the coincidence of pulses between two scintillation counters, one on either end of the TimePix telescope. The scintillators are only about 1.2 cm x

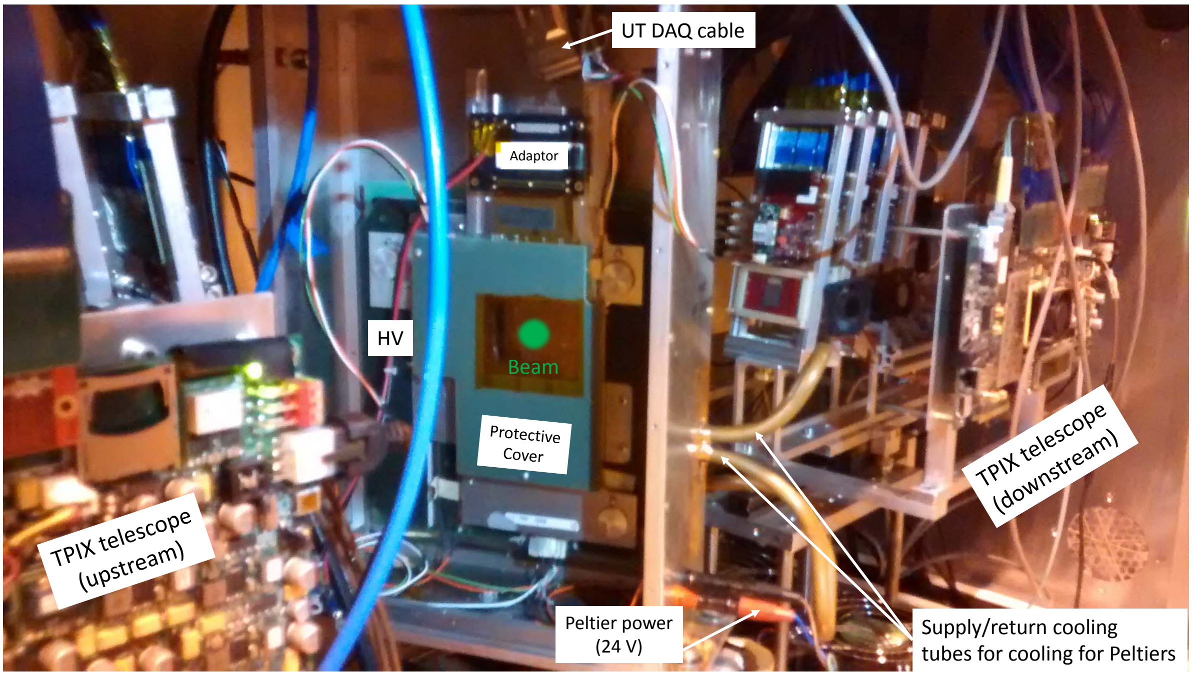

Figure 6: Photo of a UT module installed in the test beam box in the middle of the TimePix telescope.

1.2 cm in size, to match the dimensions of the TimePix sensor. If the MAMBA board was not in a busy state, it would read out the DUT and timestamp the event using the provided TimePix clock. A signal would also then be sent from the MAMBA board to the TimePix DAQ board (SPIDR board), to generate a trigger timestamp in the TimePix data stream. After correcting for a time offset between the trigger timestamp and the pixel hit times, the pixel hits associated with a trigger can be selected, and subsequently used to form pixel tracks associated with each trigger.

2.5 TimePix telescope

The TimePix telescope is described in detail in Ref. [10]. Briefly, the telescope uses two sets of four pixel planes for providing a precise measurement of beam particles' trajectories. Two stages exist to study a DUT, one in the middle between the two sets of pixel planes, and one in the back, outside the box. The planes are rotated by $\sim 10^{\circ}$ about the x and y axes to provide more charge sharing between pixels, which provides better hit resolution. Each pixel plane features pixels of size $55\,\mu\text{m} \times 55\,\mu\text{m}$, and at the center of the telescope, the pointing resolution is exquisite, about $2\,\mu\text{m}$. Some of the detectors were tested with the box placed in the middle of the telescope, and some were placed behind the telescope. In the latter case, the pointing resolution is about 12-15 μm instead of 2 μm. However, for most studies the 12-15 μm resolution is more than adequate.

2.6 Sectors tested

As the area of the UT sensors is quite large, and the beam is typically only ∼1 cm x 1 cm in size, it was decided to choose 6 points (sectors) on the Type A and 6 on the Type D sensors where bias and angle scans would be performed. The rough positions of the 6 sectors tested for the Type A and Type D sensors are shown in Figs. 7 and 8. For reference, the irradiation profiles are superimposed. Absolute position is noted on the bottom and strip number on the top, which is useful to correlate the irradiation fluence for each sector tested.

For the Type A, we aimed to take data in the most highly irradiated region (sectors 1 and 4), which corresponds to a peak fluence of 0.33×10^{14} n_{eq} cm^{-2}, a much lower fluence region (sectors 2 and 5), and lastly a region of virtually zero fluence (sectors 3 and 6). Note that the beam position for sectors 1–3 are intentionally aligned to highly illuminate the region of the embedded pitch adapters, which cover a region only a few mm's from the edge. When the FanUp sensors are tested, it is the FanUp side that is wirebonded to the Beetle, and so the beam particles are incident in the region of the PA. The FanIn side is on the opposite end, 10 cm away, and outside the luminous region of the beam. For the tests of the FanIn PA, the sensor is rotated, and it is the FanIn side that is directly wirebonded to the Beetle chips and illuminated by the beam.

For the Type D sensors, sectors 1, 2 and 3 are along the 1/4-circle cutout in regions, and correspond to regions of high irradiation ($\sim 4.6 \times 10^{14}$ n_{eq} cm^{-2}), lower irradiation ($\sim$ 0.5×10^{14} n_{eq} cm^{-2}), and negligible irradiation. Sectors 4, 5 and 6 are high and moderate irradiation, but away from the 1/4-circle cutout, and allow a comparison to the data near the cutout.

3 Software and data selection

The data from the DUT are reconstructed using the TbUT package within Kepler. Kepler is the package of algorithms that contains all the software used for testbeams in LHCb. Pedestals are determined from dedicated pedestal runs, and subtracted from the physics runs. Each physics run is processed twice. The output of the first pass is the noise of each channel σ_{noise}, which is subsequently used in the second pass to define the clustering thresholds in terms of the measured noise of the channel. In both passes, the channel-dependent pedestal is subtracted, and an event-by-event common mode noise is subtracted based on the average ADC of 32-channel groups. Within each pass, two iterations are performed in order to remove channels that may possibly have a signal in them.

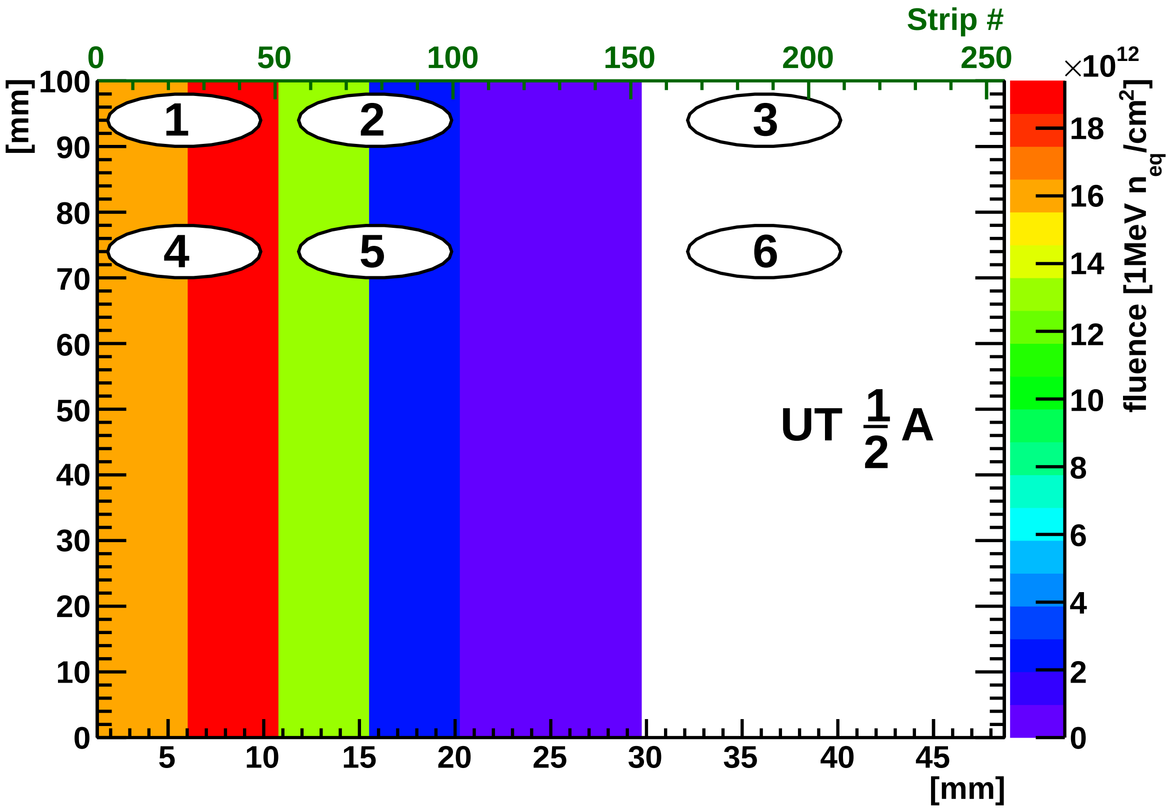

Figure 7: Sketch showing the locations (sectors) of where bias and angle scans were taken for the Type A sensors. The n_{eq} fluence received by the irradiated sensors is also indicated.

3.1 Noise in DUT

Within TbUT, the noise is compute as the root mean square (RMS) deviation of ADC values from zero, after exclusing possible signal. Offline, we do it in a more refined way; namely we fit the ADC distributions to a Gaussian function. Figure 9 shows the average value of the noise and the Gaussian width for boards A6, A8 and D5. Data from A6 was collected in July 2015, while A8 and D5 were collected in Oct 2015.

Two sample channels, ch# 155 and ch# 425 are selected and their ADC distributions are shown in Fig. 10 for the corresponding boards shown in Fig. 9.

For board A8, $\sigma_{\text{noise}} \sim 23 - 25$ ADC counts, and for board D5 it's typically about 17–22, depending on the channel number. However, in Board A6, the noise is much higher, around 40–50 ADC counts. As we will show later, this looks more like the overall gain is larger, as opposed to it being the case that board A6 has much larger noise. We note that during the October testbeam, sensor A6 was initially exhibiting very large baseline fluctuations that made seeing any beam signals impossible. To ameliorate this effect, we added a ground strap between the TT hybrid ground and the bias ground. In principle, the grounds should have been tied together at the hybrid, but the hybrid was showing

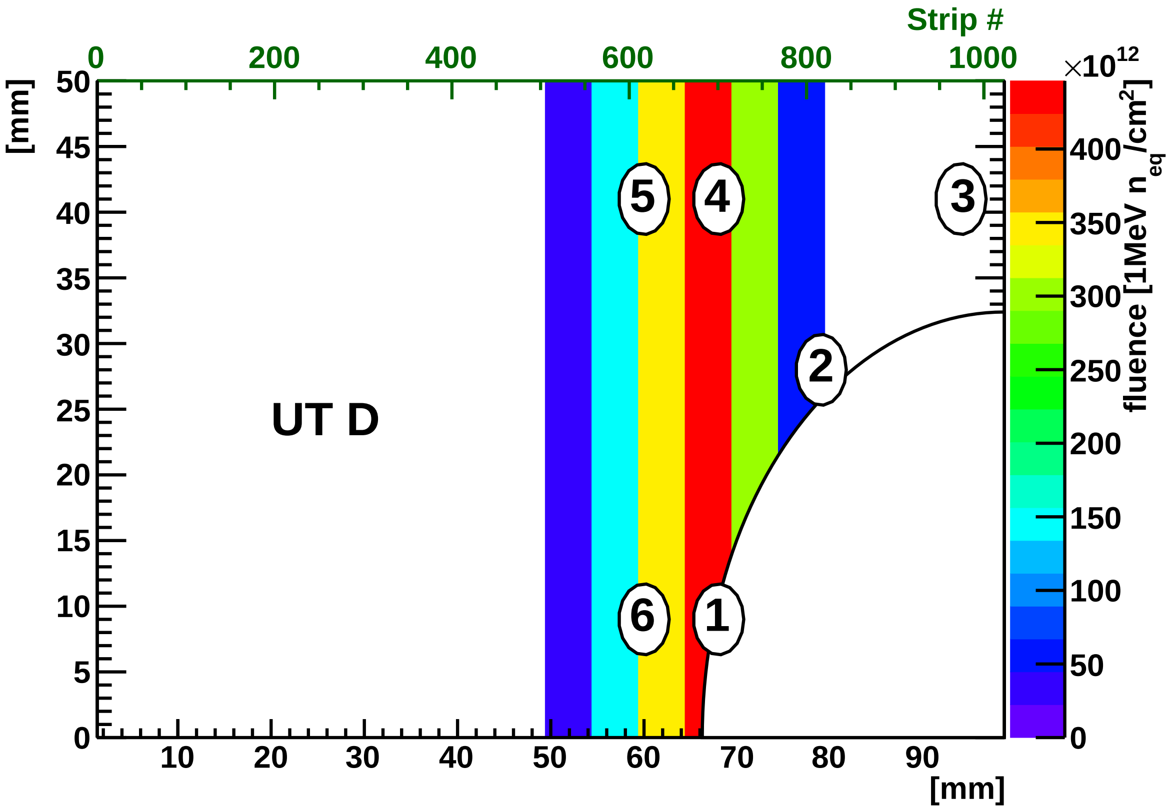

Figure 8: Sketch showing the locations (sectors) of where bias and angle scans were taken for the Type D sensors. The n_{eq} fluence received by the irradiated sensors is also indicated.

a non-negligible resistance between the two grounds. The addition of this ground strap reduced the large baseline fluctuations. Whether this has also somehow influenced the gain is not known at this point. Further bench tests are planned to understand better the noise in the MAMBA / DUT readout system. Several points should be noted here.

- The **mean** of the noise for A8 and D5 show large fluctuations, with values as large as about $\pm 1\sigma_{\text{noise}}$. On the other hand, for board A6 these fluctuations in the mean are not seen, even though the Gaussian width is significantly larger.

- There is a definite pattern that every 32^{nd} channel has larger noise; this is almost certainly an effect of cross-talk from the Beetle header. The sampling phase in in the MAMBA needs to be optimized to minimize this cross-talk. Unfortunately, there was no time to do this during the 2015 testbeams.

- In boards A6 and A8, channels 128-148 and 491–511 are not wirebonded to the silicon sensor. For those channels, σ_{noise} is in the range of about 16–18 ADC counts (compared to ∼23-25 for the connected channels) in board A6. In board A8, the unconnected channels also show a larger noise, roughly consistent with the same ratio of noise for the connected channels.

- In board A6 and A8, Beetle chips 1 and 3 are not present on the hybrid, since they were not needed. Therefore, there are no entries for ch 0-127 and 256-383.

Due to our full lack of understanding at this point of the absolute gain, most studies will focus on the signal-to-noise (S/N) ratio.

3.2 Time window of Beetle

When a signal arrives into the front end of the Beetle it goes through amplification and shaping stages, with an output shape that rises to a peak, and then falls off [11]. The front end is sampled every 25 ns using a 40 MHz clock, and the output is stored into an analog pipeline of depth 187. Unlike the LHC, where collisions are also at regular 25 ns intervals (ignoring the abort gaps, etc), the beam particles at the SPS arrive randomly and uniformly within the SPS spill of ∼3-4 seconds. That is, beam particles are not synchronized with the 40 MHz clock. For S/N studies, we select only those triggers that arrive at the *correct time* with respect to the 40 MHz clock so that the amplifier is sampled at a time corresponding to the peak output from the beam-particle induced charge deposition.

This is done by measuring the average charge collected as a function of the time within a 25 ns window relative to the clock's edge. Figure 11 (left) shows the TDC time of good DUT hits, which is, as expected, uniformly distributed with respect to the edge of the 40 MHz clock. The plot on the right shows the average charge on DUT clusters as a function of the TDC time (per 2.5 ns), which shows a peak in the 5^{th} bin (12.5 ns). To make better use of the data, we consider all time bins that have an average ADC response that is at least 97% of the peak response. Thus. for this particular sensor/run bins 4–6 are used for quantitative studies of charge collection, and hits with TDC time outside this window are rejected.

3.3 Cross-talk

It is known that there is cross-talk from one channel to another within the Beetle chip at the level of about a percent, and it differs between odd and even channels. There is an additional cross-talk effect having to do with the phase at which the ADC (on the MAMBA DAQ board) samples the signals coming from the Beetle chip. Depending on where this signal is sampled, a signal on channel N may lead to an artificial signal on channel $N-1$ or $N+1$. This is described in more detail in the 2014 testbeam analysis [2, 9]. We perform a similar study as done in previously. We look at the charge difference, $ADC(N-1) - ADC(N+1)$, in the neigboring strips about the peak strip N of a well-identified cluster. No requirement is made on the charge on either the peak or the neighboring strips' charges. This difference is plotted as a function of the charge in the peak strip, $ADC(N)$. On average, we expect that the amount of charge detected on the $N-1$ and $N+1$ strips should be equal, so that the distribution of $ADC(N-1) - ADC(N+1)$

should peak at zero. As in Refs. [2, 9], we split the sample into odd and even Beetle channel numbers.

We look at this $ADC(N-1) - ADC(N+1)$ vs $ADC(N)$ for each sector of each sensor being studied here. Since there are many such plots, most of them are relegated to Appendix B. Here, we show just one of them, here for Board A8, sector 6. Figure 12 shows the distributions of $ADC(N-1) - ADC(N+1)$ in bins of $ADC(N)$, when N corresponds to an odd channel number. The bins are 50 ADC wide. Each distribution is fit to a Gaussian function, and the mean and its uncertainty is extracted. Figure 13 presents the corresponding distributions for even N channel numbers. The mean of these distributions are then plotted as a function of $ADC(N)$, in Fig. 14, for (left) odd channel numbers and (right) even channel numbers. A linear fit to each is also shown. The fit is limited to the region of ADC>180, where the distributions tend to be more Gaussian; a linear extrapolation to ADC=0 is overlaid. The slopes are 0.128 ± 0.006 and 0.070 ± 0.006 for the odd and even channel numbers, respectively. If there was no cross-talk, the data would be consistent with a line of zero slope and and intercept at zero. The level of cross-talk here is at a similar level to what was observed in the Nov 2014 testbeam [2, 9] using the Alibava-based DAQ, although there, the even channels had the higher cross-talk.

We do observe that the slopes vary from board to board and sector to sector. Moreover, in some cases, the cross-talk is not nearly as linear as that seen here. The corresponding distributions for the other boards and sectors are compiled in Appendix B. Here, we summarize in Table 2 the slopes obtained, to give an idea of the variations seen. In general, the cross-talk effect is at the level of 5-10%, where in most cases, it is the $N-1$ strip that shows this excess of charge. Board D7 is an exception, where the slopes tend to be close to zero, or slightly negative. Board A4, sector 1, odd channels show a large slope; there appears to eb a change in slope in the 250-300 ADC range, which is not well reflected in this slope (see Fig. 68.) We do not correct the cluster charges for this cross-talk effect in the results to be shown, something to keep in mind.

3.4 Clustering in DUT

To form a cluster, there must be a *seed* strip that has a charge that exceeds $3\sigma_{\text{noise}}$. Up to 2 strips on either side are added if the charge exceeds $2.5\sigma_{\text{noise}}$. If the cluster seed is strip N, then the $N-2$ ($N+2$) strip is not considered, if the $N-1$ ($N+1$) strip is below the $2.5\sigma_{\text{noise}}$ threshold. The cluster charge is computed as the sum of all charges in the strips associated with the cluster after pedestal and common mode noise is subtracted. The position is computed using the charge-weighted average. The results that will be shown in Section 4 are at normal incidence, and therefore most of the clusters ($\sim$80% or so) are single-strip clusters.

3.5 Matching DUT hits with TimePix tracks

TimePix tracking information is added to the DUT ROOT tuples after the TimePix ROOT tuples are produced. For each triggered event in the DUT, we loop over all TimePix tracks,

Table 2: Summary of the slope of the cross-talk for each board and sector. Unless otherwise noted, the Type 1/2A results are for $V_{\text{bias}} = 300$ V, and the D type runs are at $V_{\text{bias}} = 400$ V.

Board	Sector	Odd ch slope	Even ch slope	Comment
A4(noFan)	1	0.21 ± 0.01	0.00 ± 0.01	possibly non-linear, large intercept
	2	0.13 ± 0.01	0.05 ± 0.01	
	3	0.11 ± 0.01	0.05 ± 0.01	
	4	0.09 ± 0.01	0.02 ± 0.01	
	5	0.13 ± 0.01	0.07 ± 0.01	
	6	0.01 ± 0.01	-0.01 ± 0.01	
A6(FanIn)	1	0.09 ± 0.01	0.09 ± 0.01	possibly non-linear, large intercept
	2	0.14 ± 0.01	0.07 ± 0.01	
	3	0.09 ± 0.01	0.07 ± 0.01	
	4	0.09 ± 0.01	0.07 ± 0.01	possibly non-linear, large intercept
	5	0.12 ± 0.01	0.08 ± 0.01	250 V bias
	6	0.12 ± 0.01	0.07 ± 0.01	
A8(FanUp)	1	0.16 ± 0.01	0.12 ± 0.01	
	2	0.15 ± 0.01	0.12 ± 0.01	
	3	0.12 ± 0.01	0.07 ± 0.01	
	4	0.13 ± 0.01	0.10 ± 0.01	
	5	0.17 ± 0.02	0.11 ± 0.01	
	6	0.13 ± 0.01	0.07 ± 0.01	
D5	1	0.14 ± 0.01	0.10 ± 0.01	
	2	0.15 ± 0.01	0.08 ± 0.01	
	3	0.11 ± 0.01	0.08 ± 0.01	
	4	0.10 ± 0.01	0.08 ± 0.01	
	5	0.10 ± 0.02	0.08 ± 0.01	
	6	0.12 ± 0.01	0.07 ± 0.01	
D7	1	-0.04 ± 0.04	0.02 ± 0.05	
	2	0.00 ± 0.01	-0.04 ± 0.01	
	3	0.00 ± 0.01	-0.03 ± 0.01	
	4	0.02 ± 0.01	-0.02 ± 0.01	
	5	-0.01 ± 0.01	-0.03 ± 0.01	
	6	-	-	

and require that the trigger time in the DUT matches the pixel track time. We correct for the time offset between the trigger and the pixel track time, where the pixel track time is the average time of the pixel hits used to form the track. The latency is typically about 625 ns, as its based on fixed delays within the pair of DAQs.

3.6 Alignment

Each detector is aligned so that the peak of the residual[3] distribution is centered on zero. For the studies here, we only account for translations in the direction perpendicular to the strips (x), translations along the beam axis (z), and rotations around the z axis.

[3]The residual is the distance between the projected TimePix track and the DUT hit.

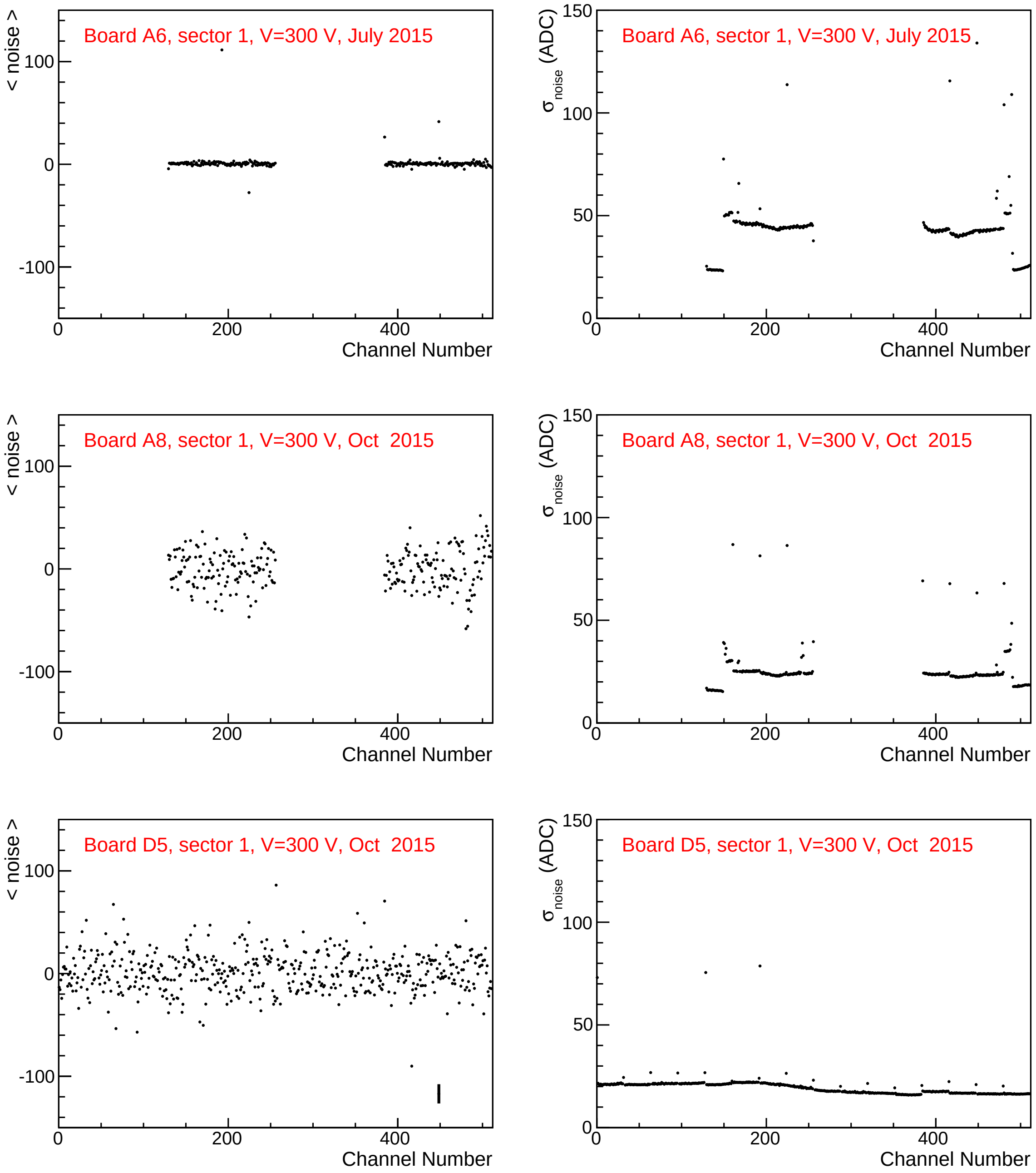

Figure 9: Mean (top left) and Gaussian width (top right) corresponding to the noise, obtained from Gaussian fits to the charge distribution, as a function of channel number for board A6. The middle (bottom) row are the corresponding set of plots for board A8 (D5).

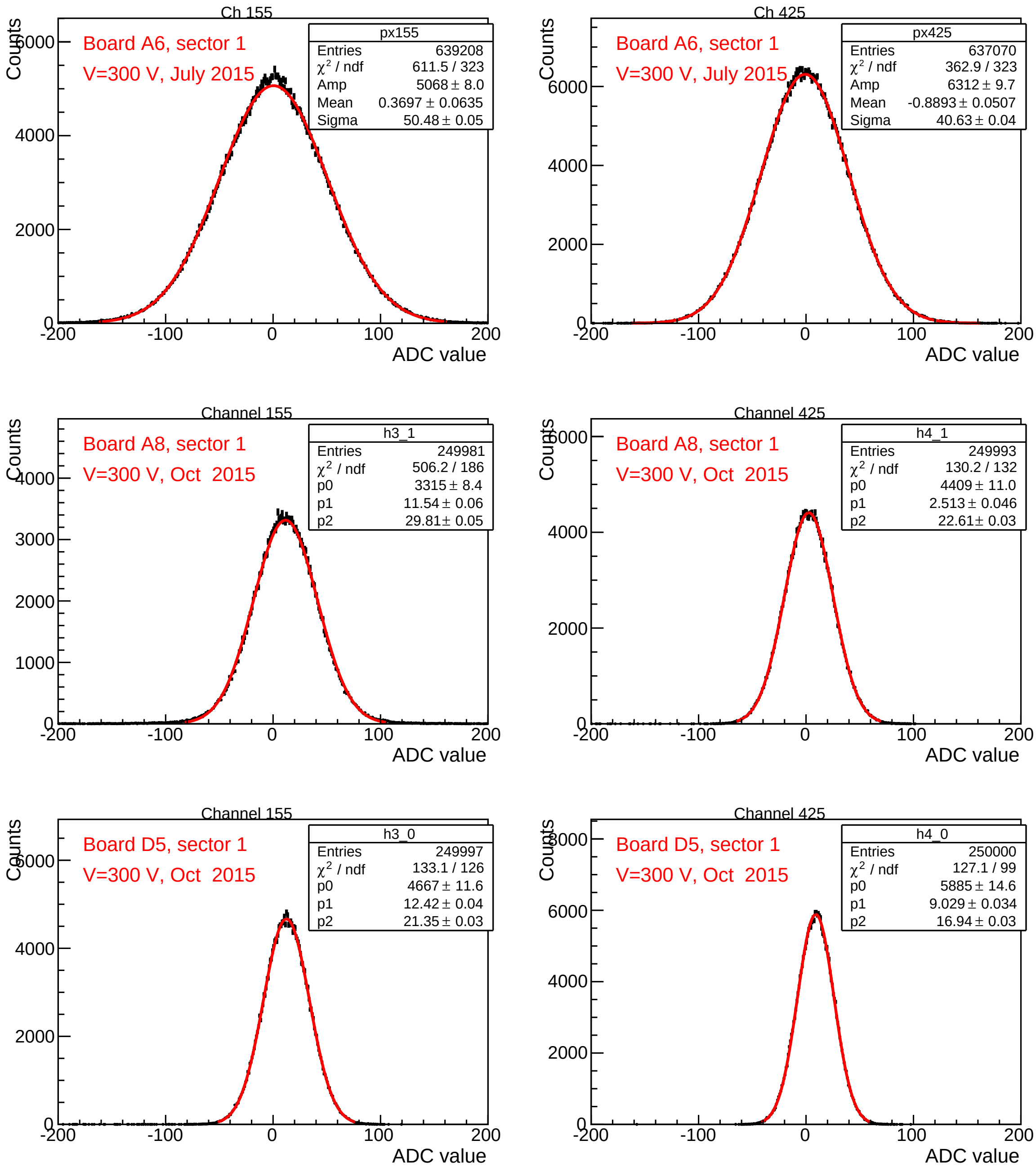

Figure 10: Examples of the ADC distributions used to compute the noise for (top) board A6, (middle) A8 and (bottom) D5, for channels 155 and 425.

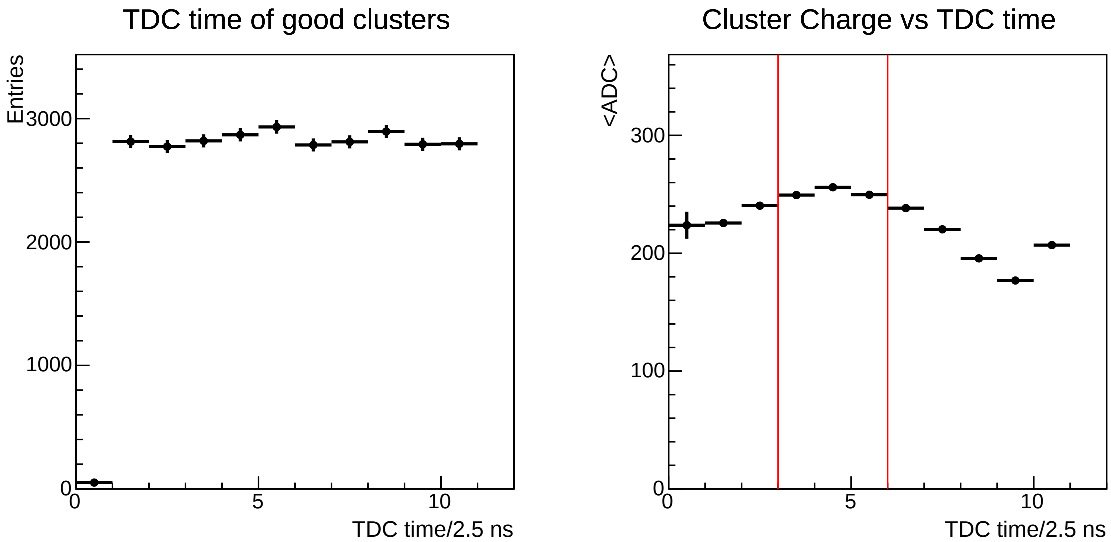

Figure 11: (Left) TDC time (in units of 2.5 ns) of DUT hits matched to tracks. (Right) Average ADC value of DUT hits as a function of the TDC time. The data is for sensor D7, sector 5, at 300 V. The red lines show the accepted events used for studying charge collection properties of the sensors.

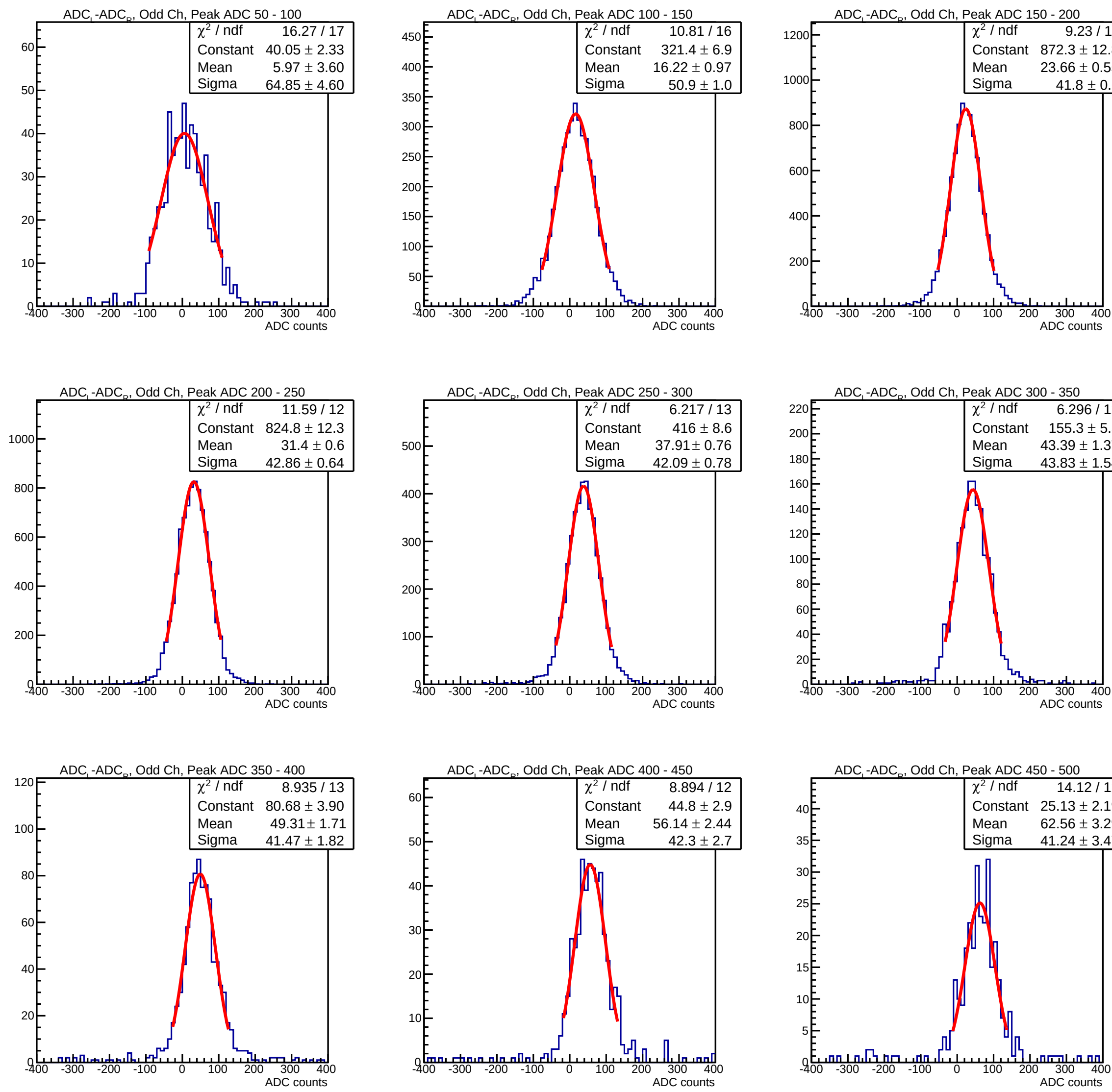

Figure 12: Distributions of $ADC(N-1) - ADC(N+1)$ in bins of $ADC(N)$ 50 ADC wide for **odd** Beetle channel numbers, for Board A8, sector 6. Each distribution is fit to a Gaussian function, and the fitted curve is overlaid.

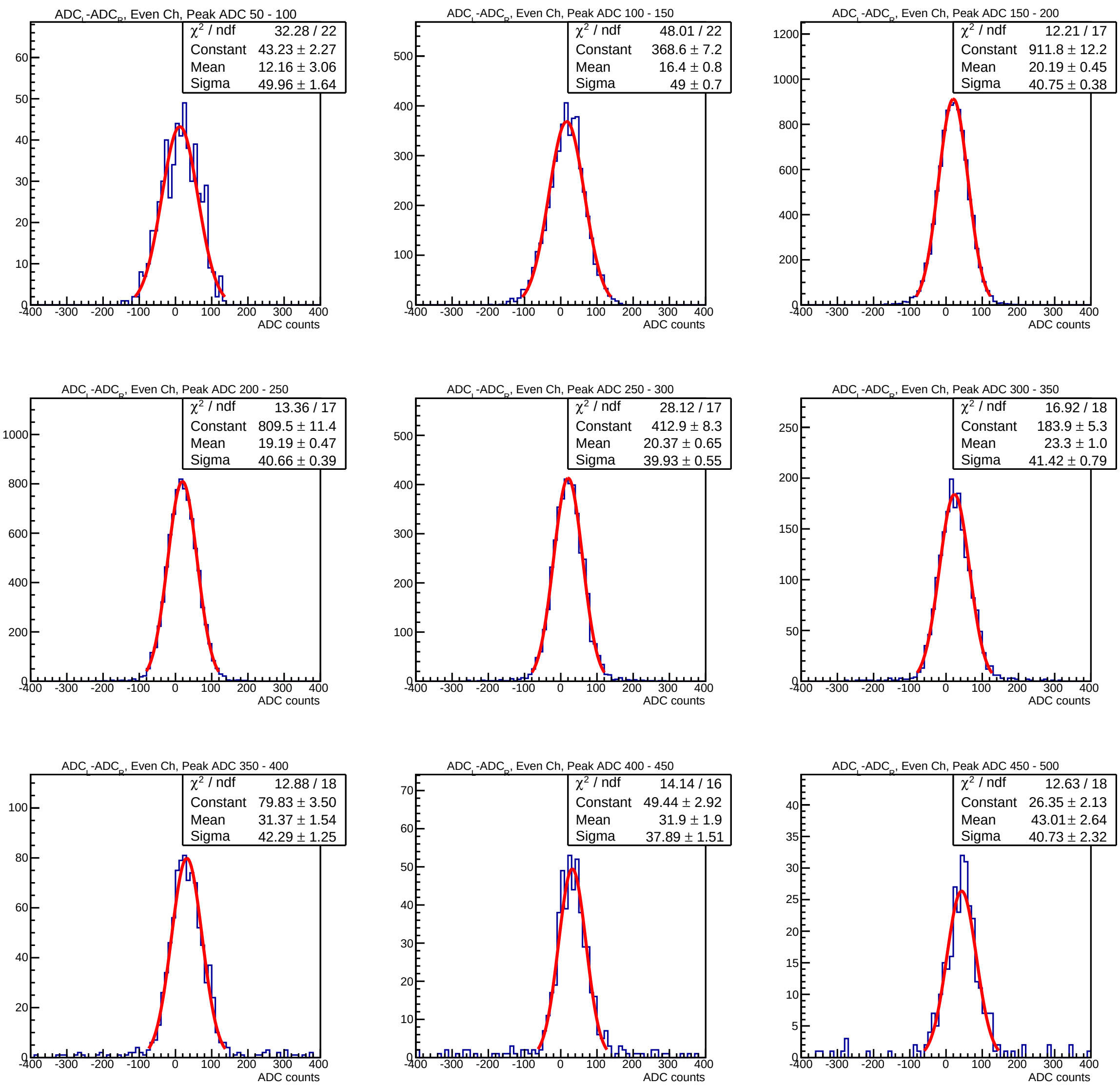

Figure 13: Distributions of $ADC(N-1) - ADC(N+1)$ in bins of $ADC(N)$ 50 ADC wide for **even** Beetle channel numbers, for Board A8, sector 6. Each distribution is fit to a Gaussian function, and the fitted curve is overlaid.

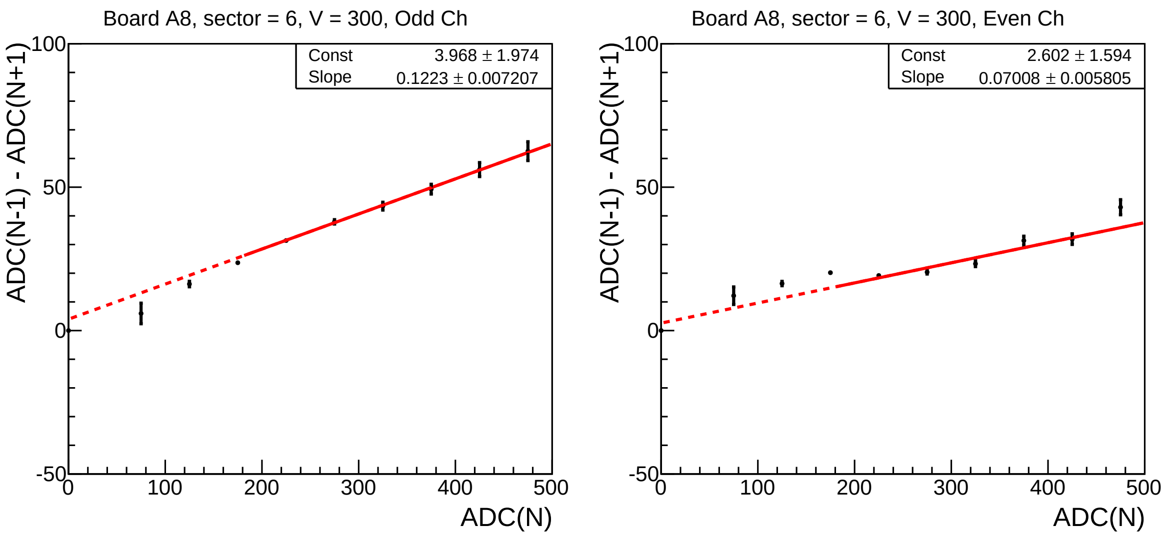

Figure 14: Graphs of $ADC(N-1) - ADC(N+1)$ versus $ADC(N)$, for (left) odd numbered Beetle channels and (right) even numbered Beetle channels, for Board A8, sector 6. A linear fit to each is overlaid, where the solid portion is the fit region and the dahsed line is an extrapolation. See text for details.

4 Results

In this section, we discuss some of the key results of the various sensors. First in Figs. 15 - 19, we show the strip numbers where beam was incident in the testbeam for each sector and sensor tested, which are reported on below. The radiation fluence for each of the sectors studied can be correlated with the fluences shown in Figs. 7 and 8.

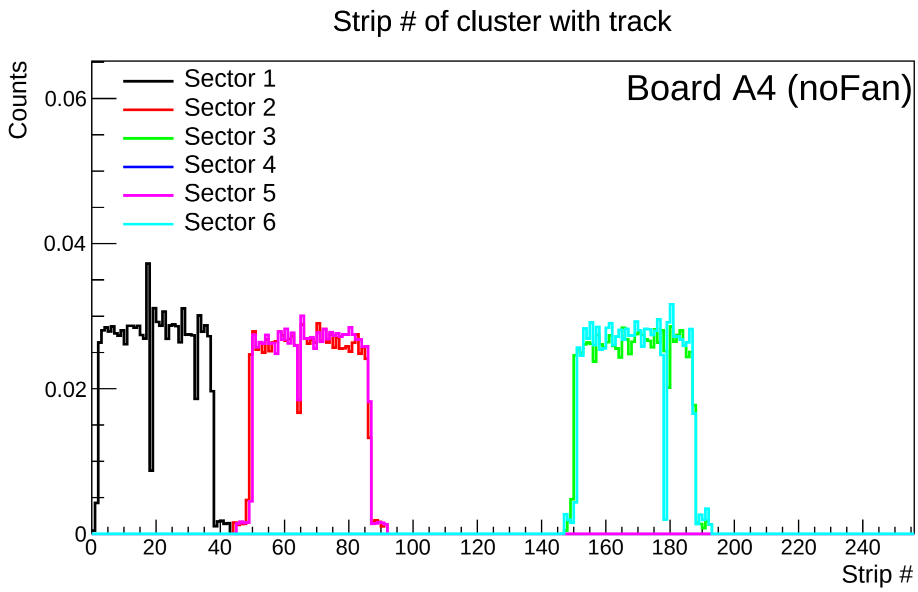

Figure 15: Beam profile in terms of strip number for Board A4.

4.1 Type 1/2A - FanIn Sensor (A6)

4.1.1 Efficiency near embedded pitch adapter of FanIn

The most important test of the Type A sensors is to test the performance in the region of the embedded pitch adapter. The FanIn sensor test was done when the detector was in the middle of the TimePix telescope, and therefore the pointing resolution of the tracks $\sim$2 μm.

Each track is projected to the DUT, and we search for a DUT cluster within 200 μm of the track in the x direction (the measurement direction of the DUT strips). The efficiency can be computed as the fraction of events where there is a DUT hit within 200 μm relative to the total number of track projections. Tracks are required to be within the nominal acceptance of the DUT. Figures 20 and 21 show the efficiency as a function of X and Y for each of the 6 sectors.

The efficiency vs X shows an *oscillation* of the efficiency for some of the sectors, which is largest for the irradiated sectors. This is due to the fact that the bin width is 100 μm, and, as will be shown shortly, the efficiency depends on where the track hits relative to the

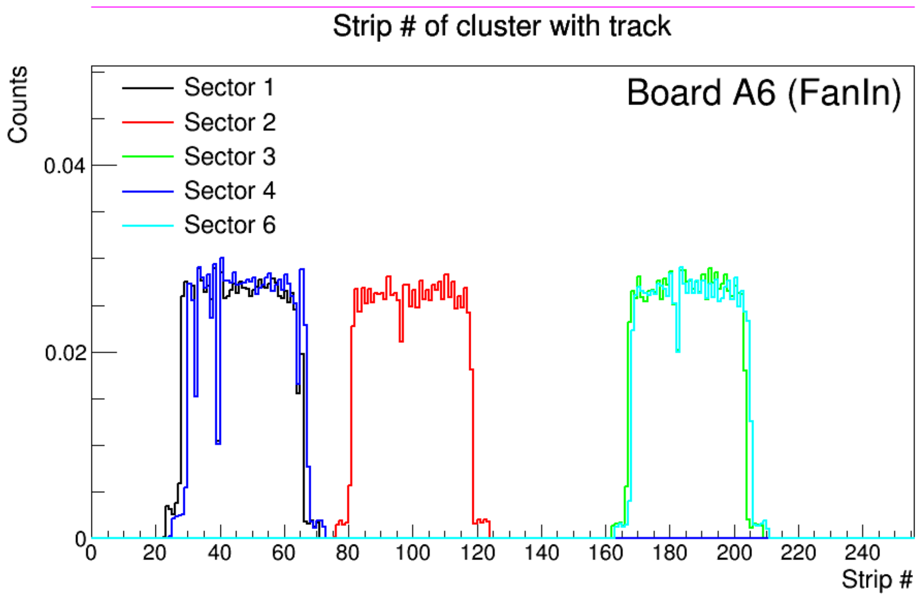

Figure 16: Beam profile in terms of strip number for Board A6.

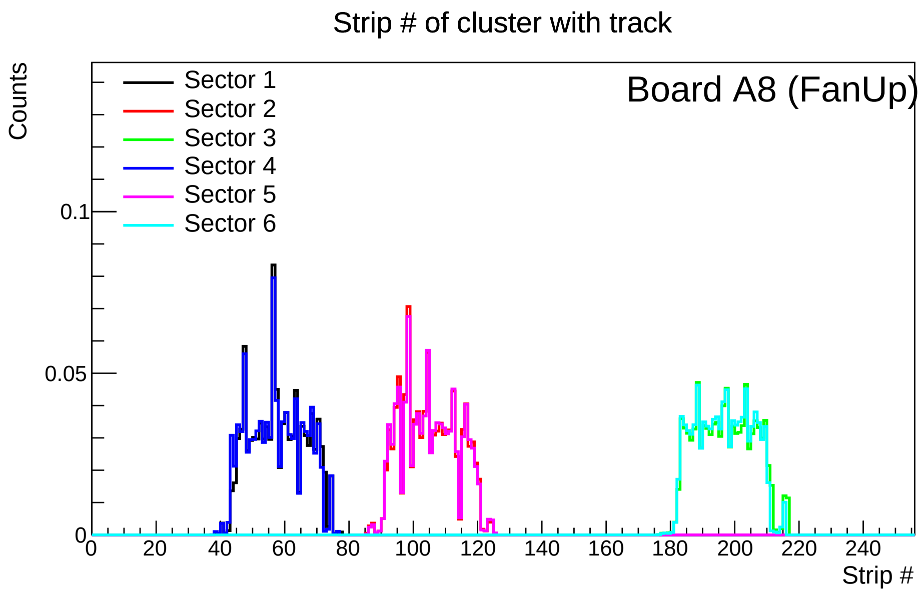

Figure 17: Beam profile in terms of strip number for Board A8.

center of the strip, which has a periodicity of 190 µm. Thus one ends up with a *beat-like* modulation of the efficiency. We also see a few regions along X where the efficiency drops substantially. This is due bad strips (possibly noisy, or bad wirebonds).

More importantly, we see that the efficiency is mostly flat along Y, but shows a significant drop near the largest Y values for sectors 1–3 (but not 4, 5, 6); this corresponds

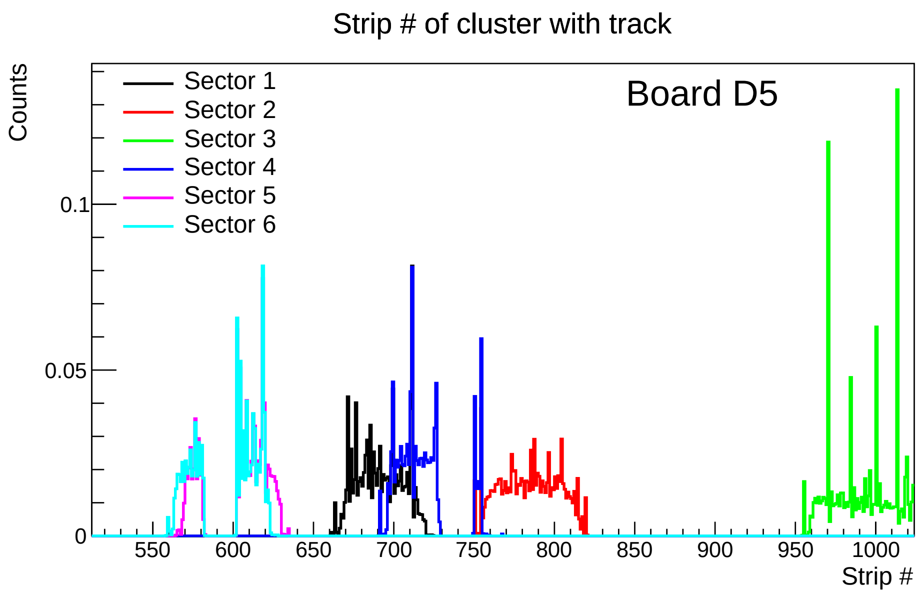

Figure 18: Beam profile in terms of strip number for Board D5.

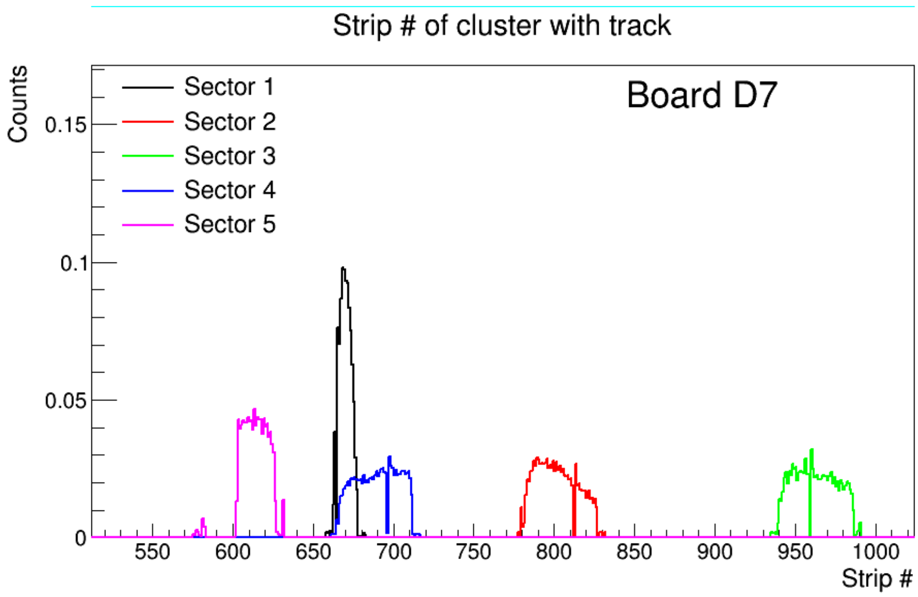

Figure 19: Beam profile in terms of strip number for Board D7. Sector 6 of board D7 had some issues, and is not shown.

to the top edge of the sensor, and is where we expect the embedded PA to be. To study this in more detail, we show in Fig. 22 the position (Y vs X) of the missed hits (red points) as determined from the TimePix track. The blue points are just for reference, and show the position of the track when it is within 10 μm of the center of a strip. Below the two

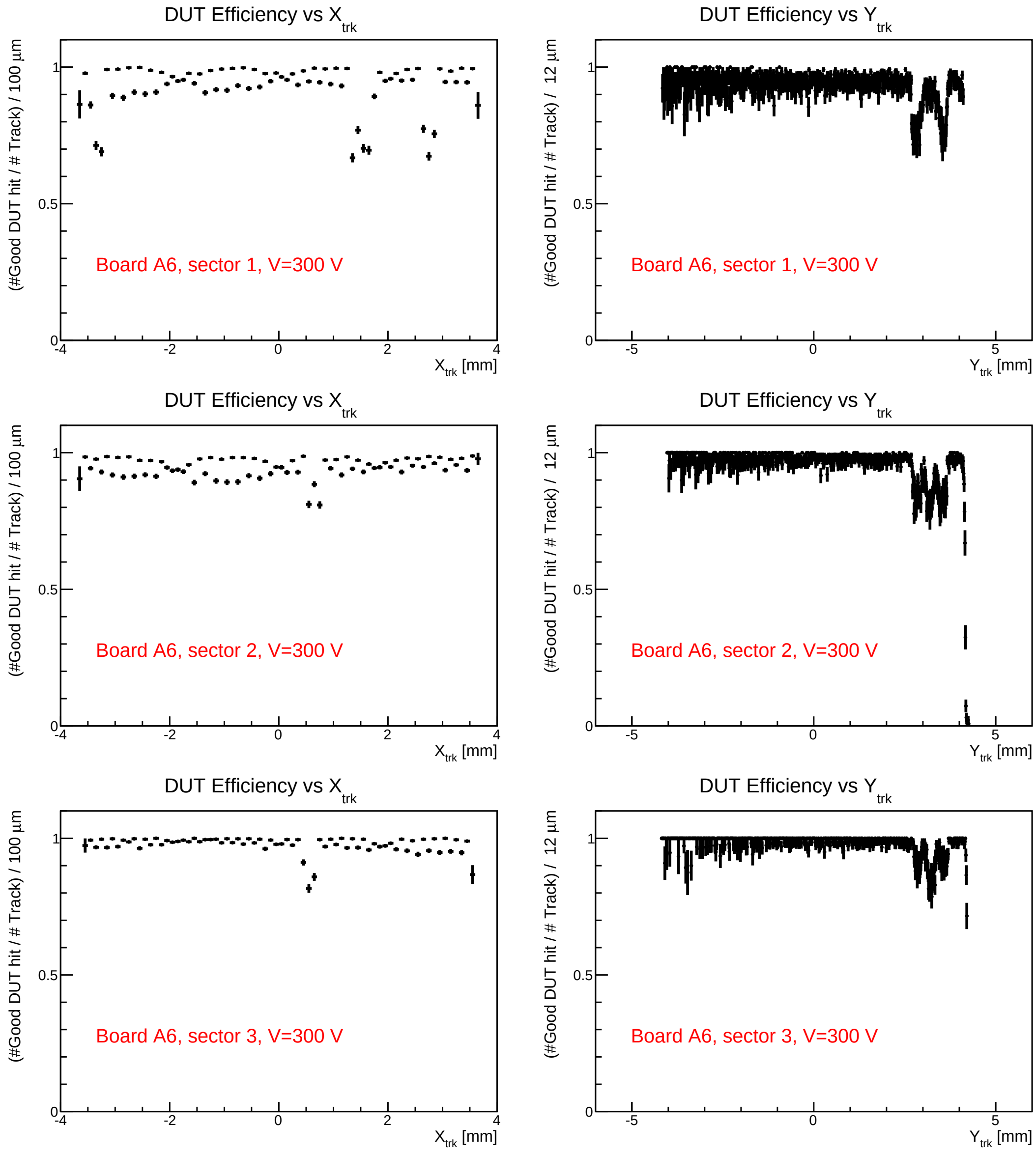

Figure 20: Efficiency as a function of the (left) X and (right) Y coordinate, for sectors 1, 2 and 3, as indicated, for the FanIn sensor.

data figures are the layouts of the FanIn pitch adapters. It is thus clear that: (i) there is an inefficient region where the double-metal layers cross the silicon strips, and (ii) this inefficient region tends to be in the middle between adjacent strips. The inefficiency also occurs in the region of the 75 μm bonds pads.

To better quantify the magnitude of the inefficiency two areas are selected: one in the pitch adapter region, and a second in a control region away from the pitch adapter. For each track, we compute an interstrip position ($\Delta X/P$), where δX is the difference in X between the track projection and the center of the closest strip. By construction, every

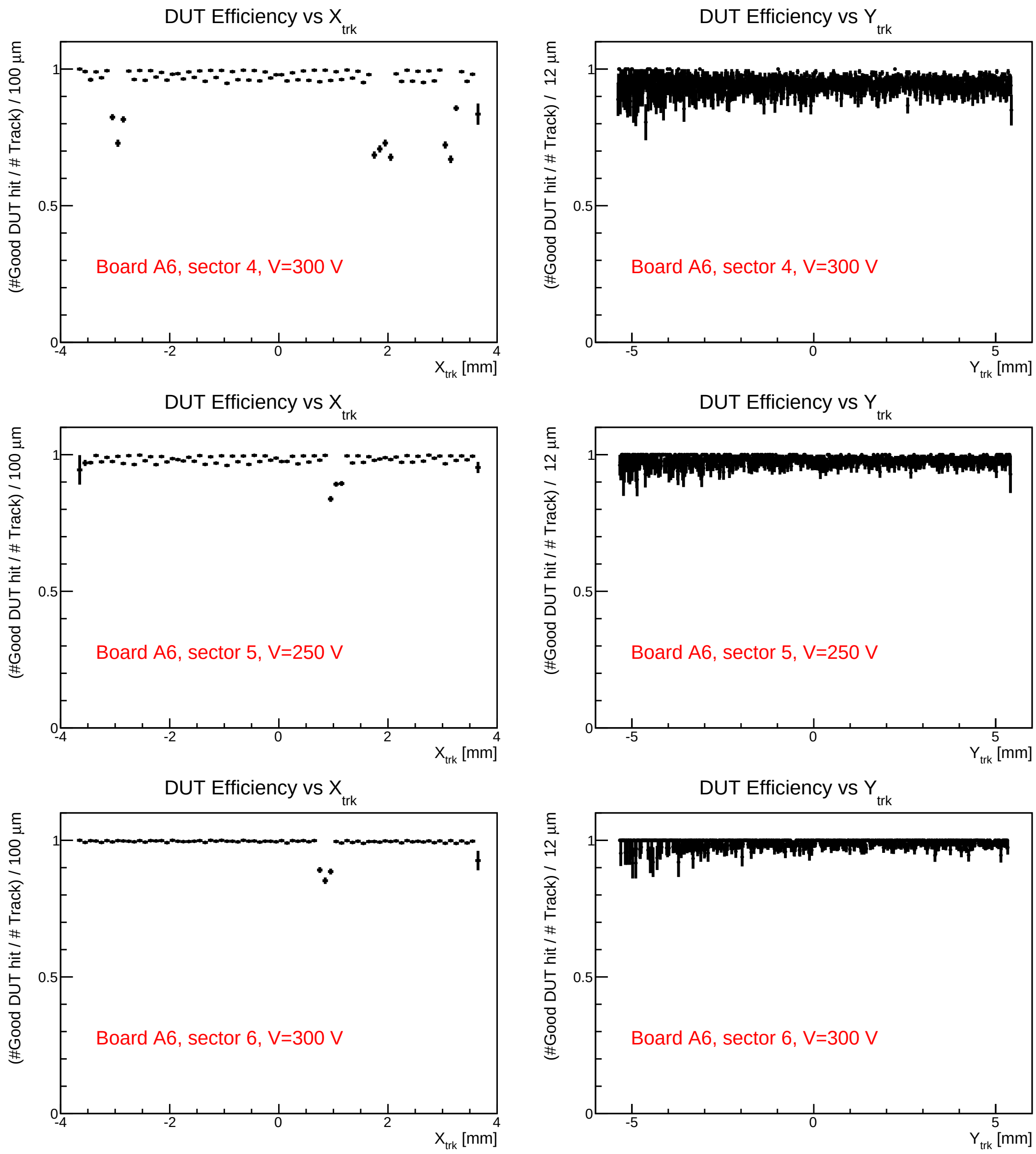

Figure 21: Efficiency as a function of the (left) X and (right) Y coordinate, for sectors 4, 5 and 6, as indicated, for the FanIn sensor.

track must have an interstrip position that is in the range [-0.5, 0.5], where 0.0 corresponds to the track striking the center of strip N, -0.5 is half-way between strip N-1 and N, and $+0.5$ is half-way between strip N and N+1. In this way, we can investigate the efficiency as a function of the interstrip position, as shown in Fig. 23.

We see that from about -0.3 to $+0.3$, or from -57 µm to +57 µm, corresponding to a region over the center of the strip, the PA and control region both give high efficiency. However, starting at about 57 µm from the strip center to the half-way point at 95 µm, there is a steep drop in the efficiency, which reaches about 10% in the last 0.1 unit ($\sim$10 µm)

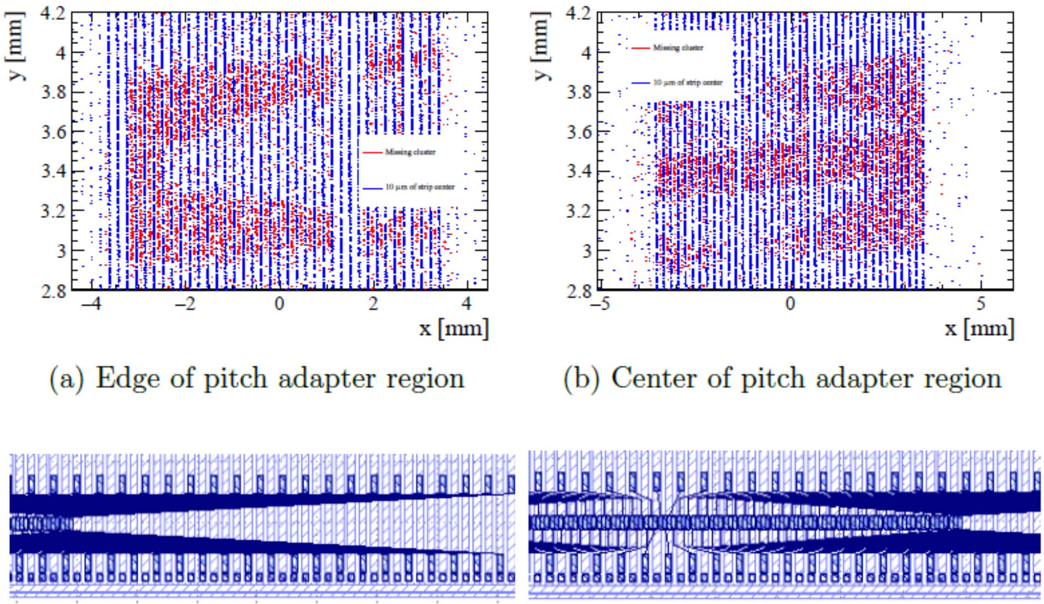

(a) Edge of pitch adapter region

(b) Center of pitch adapter region

(c)

(d)

Figure 22: (Top) Position (Y vs X) of the track when there are missing clusters (red points), and for referencing the location of the strips, the position of found clusters within 10 μm of the strip center (blue points), for two different regions of the FanIn pitch adapter. Below each is the layout of the FanIn embedded PA which corresponds to the regions above.

on either side. Thus we observe an unacceptably large loss in CCE in the region of the PA.

If no clusters are being collected on the strip closest to the track, then where is the charge going? We believe it is coupling to the other strips due to the second metal layer. To test this hypothesis, we select tracks that have $|\Delta X/P| > 0.4$, and compare the charge collected on (a) the nearest strip, and (b) the sum over the 100 closest strips, as shown in Fig. 24. Three distributions are overlaid in each case: the PA region (red points), a control region below the PA (blue points), and noise. The noise distribution is obtained by considering events where the track is vertically outside the the DUT acceptance.

For Fig. 24(a), we see that the control region shows a significant charge on the closest strip. However, the PA region has much lower charge. Although it is not consistent with pure noise, it is reduced sufficiently that the charge collected on the strip will generally not pass the requirements to form a cluster. If we sum up the charge on the nearest 100 strips, we see that PA and control region are much more similar, indicating that the charge deposited by the particle is not *being lost*, but rather it is being picked up on other strips.

Outside the PA region, the sensor seems to behave *normally*, but in the region of the

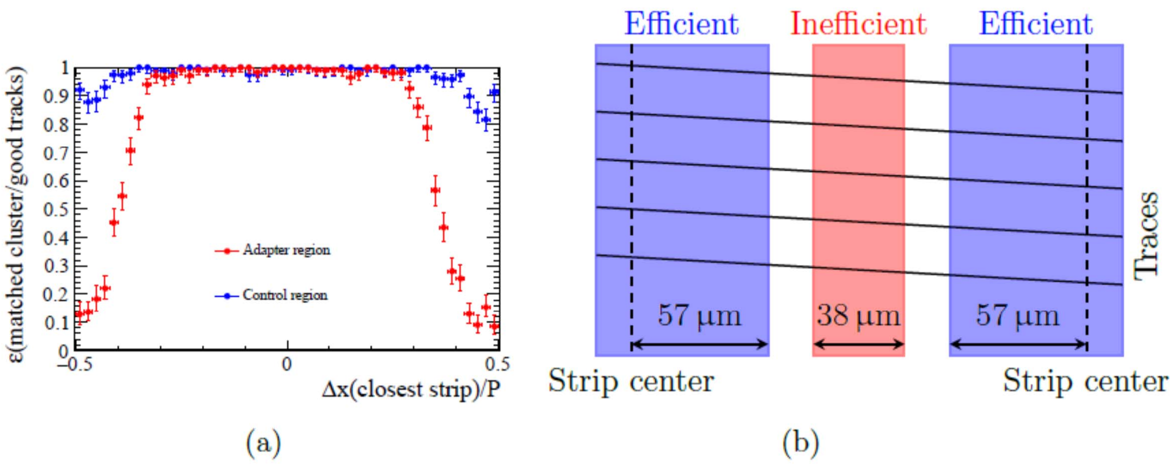

Figure 23: (Left) Efficiency versus interstrip position ($\Delta x/P$) for the PA region (red points) and a region away from the PA (blue points). (Right) Cartoon showing the highly efficient regions, and the regions of low efficiency.

PA, there is an unacceptable loss of CCE. This loss in efficiency is slightly dependent on irradiation, but is there even in the unirradiated section. In this middle region between the two strips there are p-stops, which inhibit the n-type strips from effectively shorting to each other. Perhaps there is some coupling between the p-stops and the second metal layer, that is causing the effect. This is only speculation at this point, and a detailed simulation could potentially provide some insight.

4.1.2 Signal to noise in FanIn

We now look at the signal, noise and S/N ratio as a function of bias voltage, for each of the 6 sectors. We reject the region of the PAs for this study. At each voltage, the cluster charge distribution is fit to a Landau function, convolved with a Gaussian resolution function. From the fit, the *signal* is given by the the most probable value (MPV) parameter of the Landau function. For each sector, we also compute the average noise over the strips used in forming the Landau distribution. The S/N is then readily computed from the signal and noise. Figure 25 shows the signal, noise, and S/N as a function of bias voltage for each of the 6 sectors. We see that the signals all rise up and plateau at a similar value of about 360 ADC counts. The noise shows a small increase as the bias voltage drops, except from the most highly irradiated sector, which appears to be flat. The S/N is consistent for sectors in the same irradiation zone (1,4), (2,5), (3,6). The largest S/N of about 8.5 is for the unirradiated sector, as one would naively expect. The S/N drops to about 8.0 and

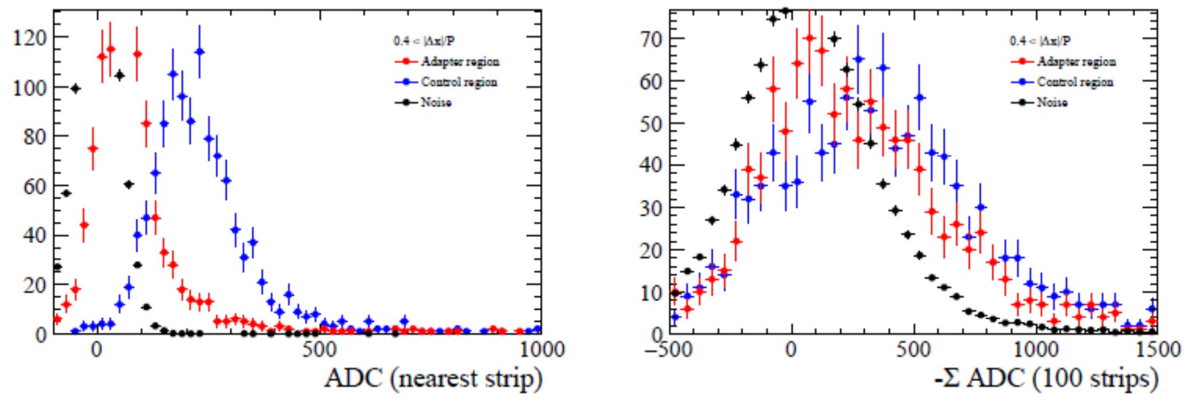

(a) Signal on nearest strip

(b) Sum of signal over 100 strips

Figure 24: (Left) Charge detected on closest strip to a track's projection for the adapter region, control region, and for pure noise. (Right) Charged detected on sum over 100 strips around the track's projection for the adapter region, control region, and for pure noise.

then 7.7 for sectors (2,5) and (1,4), respectively. If we assume the gain is stable, then the drop in S/N is due to larger noise in the irradiated sectors, not to a loss of charge collected. The fact that the signals all plateau at approximately the same value would indicate that the gain has not changed too much during the time that these data sets were recorded.

The Landau distributions for one particular sector, sector 3, are shown in Fig. 26. Clusters in the top area of the pitch adapter are removed from these distributions.

At this point, we reiterate that this is a 200 μm thick sensor. For a 320 μm thick sensor we would expect about a factor of 1.6 increase in charge collected. Assuming no increase in the noise, this would imply a S/N of about 12. Moreover, there was no time for optimizing the noise performance of the system in the testbeam, so there is good reason to believe the S/N will be even higher than this (although clearly it needs to be demonstrated).

4.1.3 Efficiency versus interstrip position in FanIn

We now look at the efficiency as a function of the relative interstrip position. For each track we find the two closest strips at the DUT, say N and $N+1$. Here, the interstrip position is defined as $(x_{trk} - x_N)/(x_{N+1} - x_N) - 0.5$, so the distribution varies from -0.5 to $+0.5$, where -0.5 means the track hits the center of the N^{th} strip and $+0.5$ means it hits the center of the $N+1^{th}$ strip. This definition differs from that shown in Fig. 23, where $x = 0$ corresponds to a track hitting the center of strip N, and -0.5 ($+0.5$) is halfway between strip $N-1$ and N (N and $N+1$).

Figure 27 shows the efficiency versus the interstrip position for each sector. For each sector, we show all the available bias voltages overlaid. One can clearly see that even at the highest voltages, there is a drop in the efficiency when the track hits right between the middle of two strips (zero, on the plots). It is this drop in efficiency at the middle of two strips, which causes the oscillatory efficiency in Fig. 20 and 21 as a function of X.

The drop in efficiency at the midpoint is easily understood. The clustering requires a seed strip with charge exceeding 3 times the noise. With a S/N of only about 7–8 on average, when the track hits the middle, the charge is shared/split between the two strips. If one get a cluster with a smaller signal (due just to the Landau fluctuations of charge deposition, or noise), it is quite possible that neither of the strips are above the 3σ threshold. The loss at the center increases with the radiation fluence; that is, sectors 3 and 6 have the lowest loss, and sectors 1 and 4 have the largest loss, which reflects the change in the S/N (see Fig. 25). It is therefore important that in the final detector we aim to maintain a S/N of at least 9-10. Clearly larger is better. This will minimize the potential loss of clusters when the charge is shared between two strips.

4.1.4 Cluster size and residuals

Figure 28 shows the residuals between the DUT hit and track for 1 and 2-strip clusters, for each sector, for tracks at normal incidence. The 1-strip clusters make up about 80-90% of the clusters, and show a fairly flat distribution, as would be expected. Sector 1 shows the largest fraction of 2-strip clusters, and the peak in the residual distribution is much narrower. This is consistent with that which was seen in the irradiated sensors in the 2014 testbeam. Namely, in irradiated detectors, there is an increase in charge sharing, giving rise to better position resolution.

It should be pointed out here that there is a known cross-talk effect between neighboring strips, which biases the charge on the *side strip* in a 2-strip cluster[4]. Upon examination, we see there is a skewing of the 2-strip residuals, particularly visible in the unirradiated sectors. This is almost certainly due to the asymmetric cross-talk, which is not corrected for in this analysis, since position resolution is not our primary objective in the studies presented here.

[4]Side strip(s) are any strips that exclude the seed strip in a cluster.

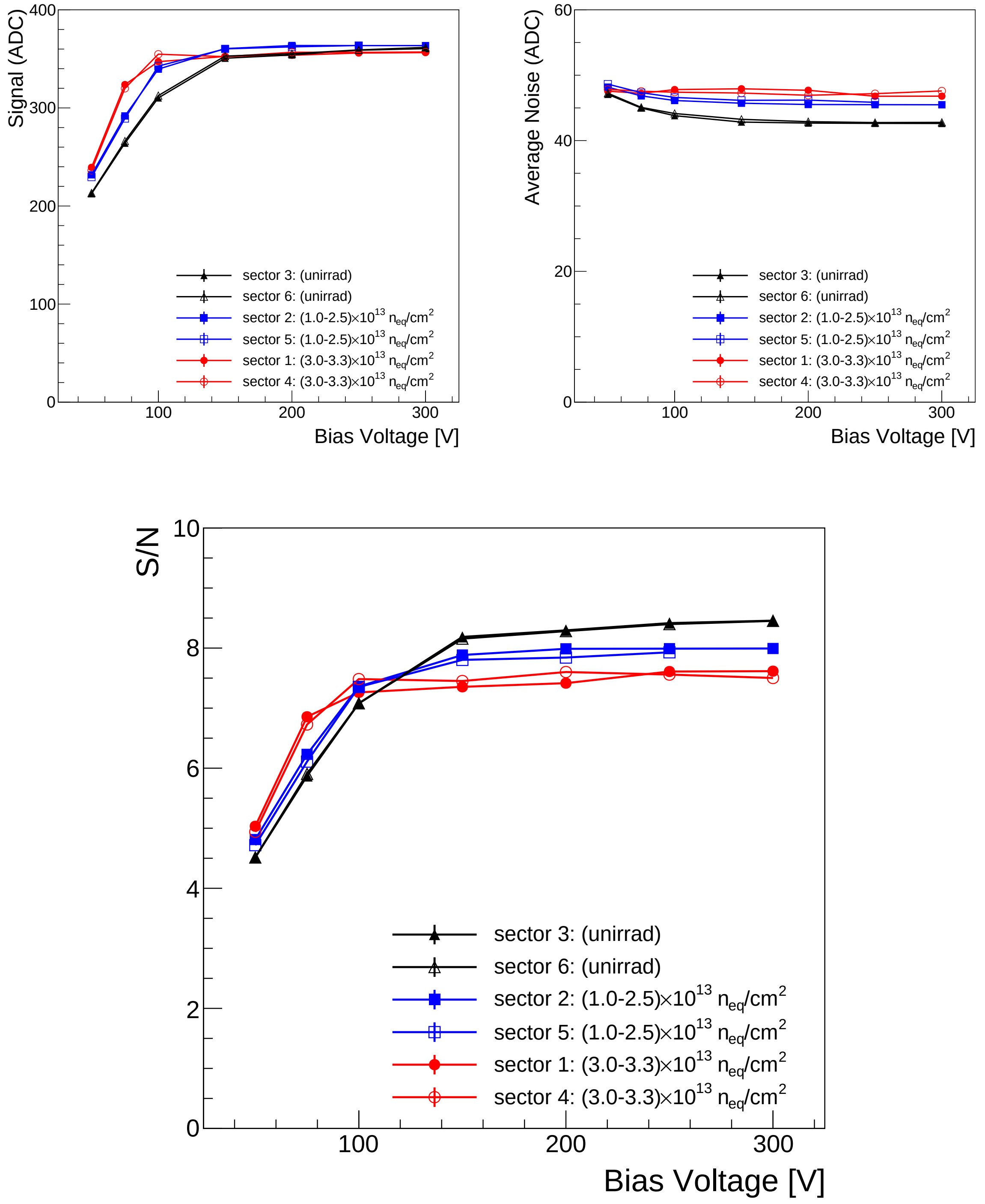

Figure 25: Signal, noise and S/N as a function of bias voltage for each of the 6 sectors, for Board A6 (FanIn).

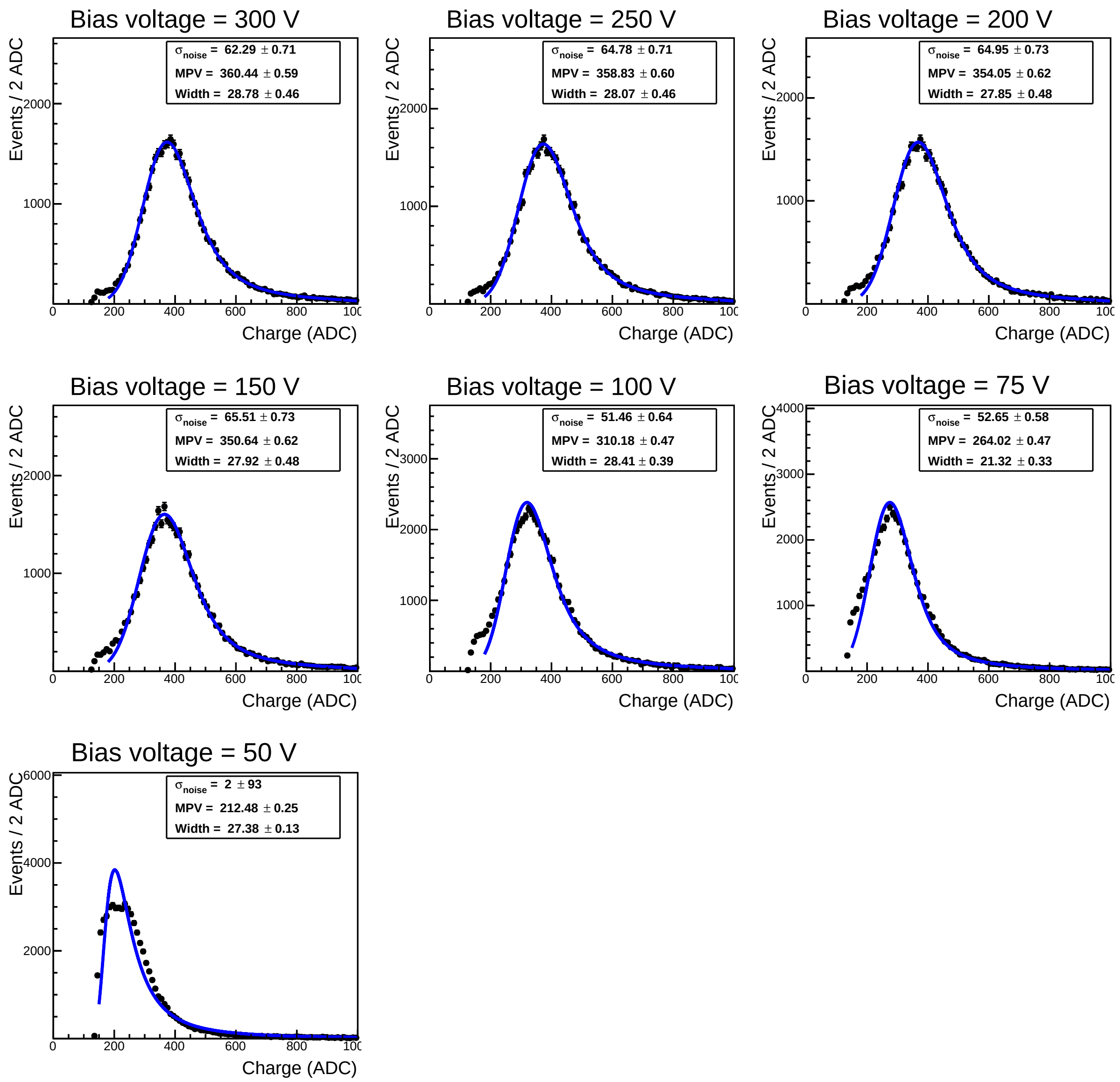

Figure 26: Charge collected in sector 3 of the FanIn sensor for several bias voltages from 50 V to 400 V for the FanIn sensor. Fits to the data using a Landau distribution convolved with a Gaussian function are overlaid.

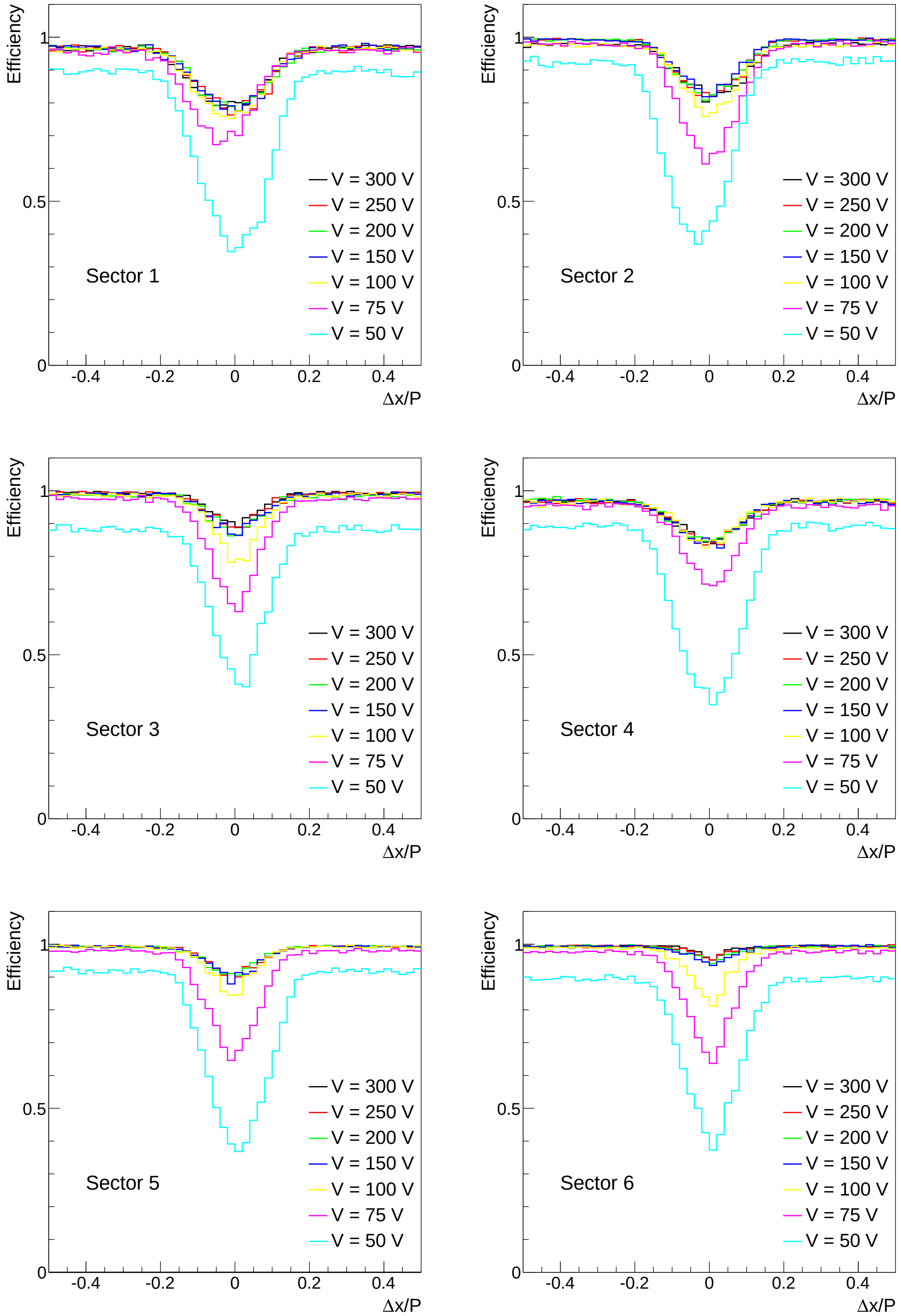

Figure 27: Efficiency versus interstrip position for several bias voltages, and each sector, for the FanIn sensor.

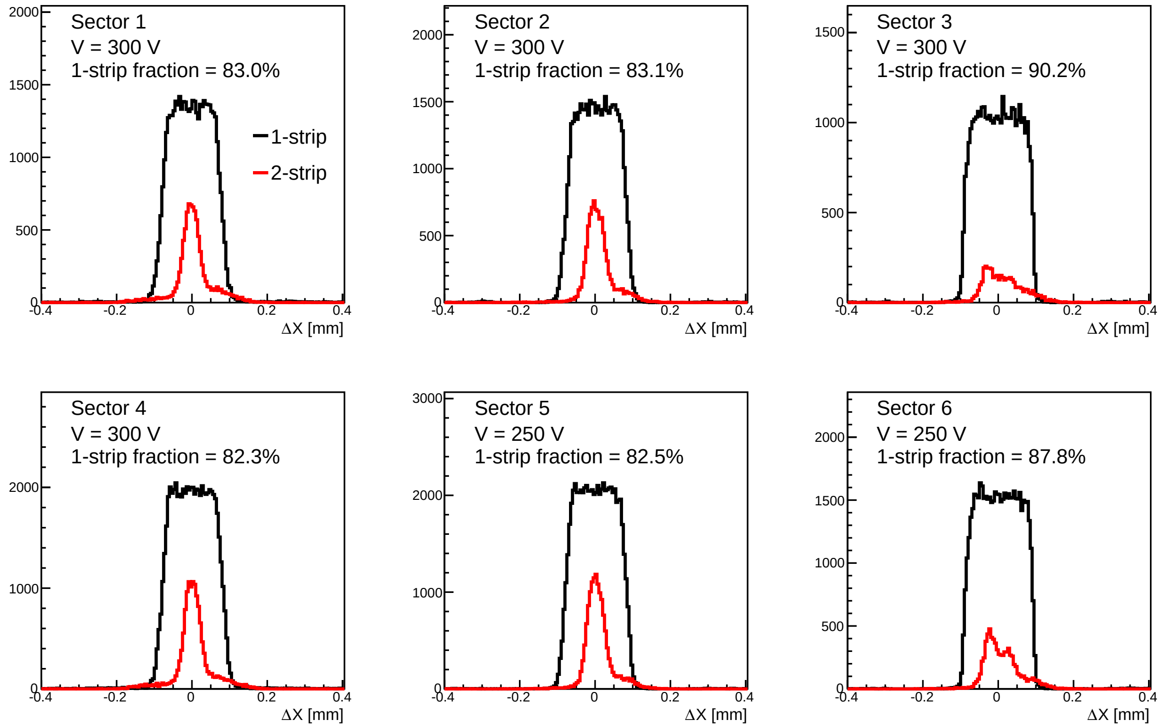

Figure 28: Residuals for 1 and 2-strip clusters for the 6 sectors of the FanIn sensor for tracks at normal incidence.

4.2 Type 1/2A - FanUp Sensor (A8)

For this sensor, the readout was also via the embedded PA 75 μm pitch pads, but for the FanUp, the second metal layer is not in the active region of the sensor. The data for the FanUp sensor was taken in October 2015, whereas the FanIn data was collected in the first (July 2015) testbeam period in 2015. Here, we present some of the corresponding plots that have been shown for the FanIn sensor previously.

4.2.1 Charge collection and signal to noise of FanUp sensor

Figure 29 shows a typical set of distributions of collected charge, here for sector 3, for bias voltages ranging from 75 V to 400 V . Overlaid are the Landau fits, which are not perfect, but adequate for our purposes.

Figure 30 shows the signal, noise and S/N for the FanUp sensor. A S/N in the range of 7.8–8.5 is reached, much like the FanIn sensor, at the highest voltage. However, we note that the both the signal and the noise are dramatically lower than for the FanIn sensor. Somehow, it appears that the gain of the system is quite different between the data-taking for the FanIn sensor (July 2015) and the FanUp sensor (October 2015). The cause of this apparent change in gain is not known.

4.2.2 Efficiency vs X and Y of FanUp sensor

Here, we investigate whether there is any indication of a loss of efficiency as one gets close to the top of the sensor, in the vicinity of the pitch-adapting traces. Figures 31 and 32 show the efficiency as a function of X and Y for each of the 6 sectors. No loss of efficiency is observed for the FanUp sensors. In sectors 1-3, the beam appears to cover a smaller region vertically. This is because part of the beam is off the top edge of the sensor.

4.2.3 Efficiency versus interstrip position of FanUp sensor

Figure 33 shows the efficiency versus the interstrip position for each sector of the FanUp sensor. For each sector, we show all the available bias voltages overlaid. One can clearly see that even at the highest voltages, there is a drop in the efficiency when the track hits right between the middle of two strips (zero, on the plots). It is this drop in efficiency at the middle of two strips, which causes the oscillatory efficiency in Fig. 31 and 32 as a function of X.

While these results are encouraging, we note that this study does not measure the absolute active length or area of the sensor. It shows that the DUT efficiency has a uniform acceptance up to a certain vertical location, and then it drops rapidly to zero. We *assume* that this corresponds to the nominal edge of the active area. To measure the size of the active area, we'd have to have the beam illuminate the full sensor, but the TimePix is only 1.2 cm^2, so we could not get tracking information over the full active area. Alternately, if the vertical motion controller is calibrated to sufficient precision, we could possibly take

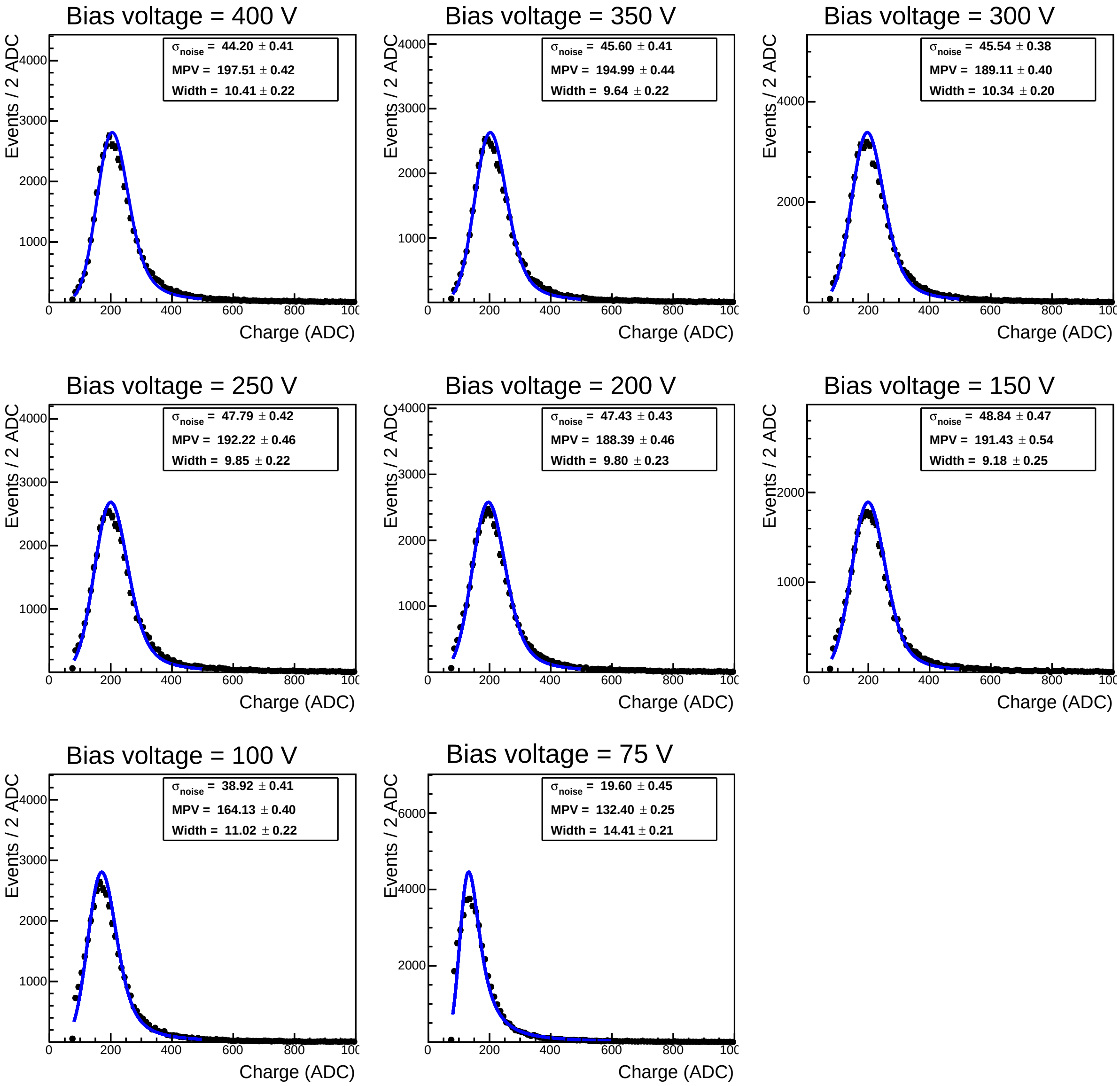

Figure 29: Charge collected in sector 3 of the FanUp sensor for several bias voltages from 75 V to 400 V for the FanUp sensor. Fits to the data using a Landau distribution convolved with a Gaussian function are overlaid.

data at the upper and lower edge, and account for the vertical translation of the stage to compute the active length of the sensor.

4.2.4 Cluster size and residuals for FanUp sensor

Figure 34 shows the residuals between the DUT hit and track for 1 and 2-strip clusters, for each sector. The results are very similar to those which are seen as for the FanIn sensor.

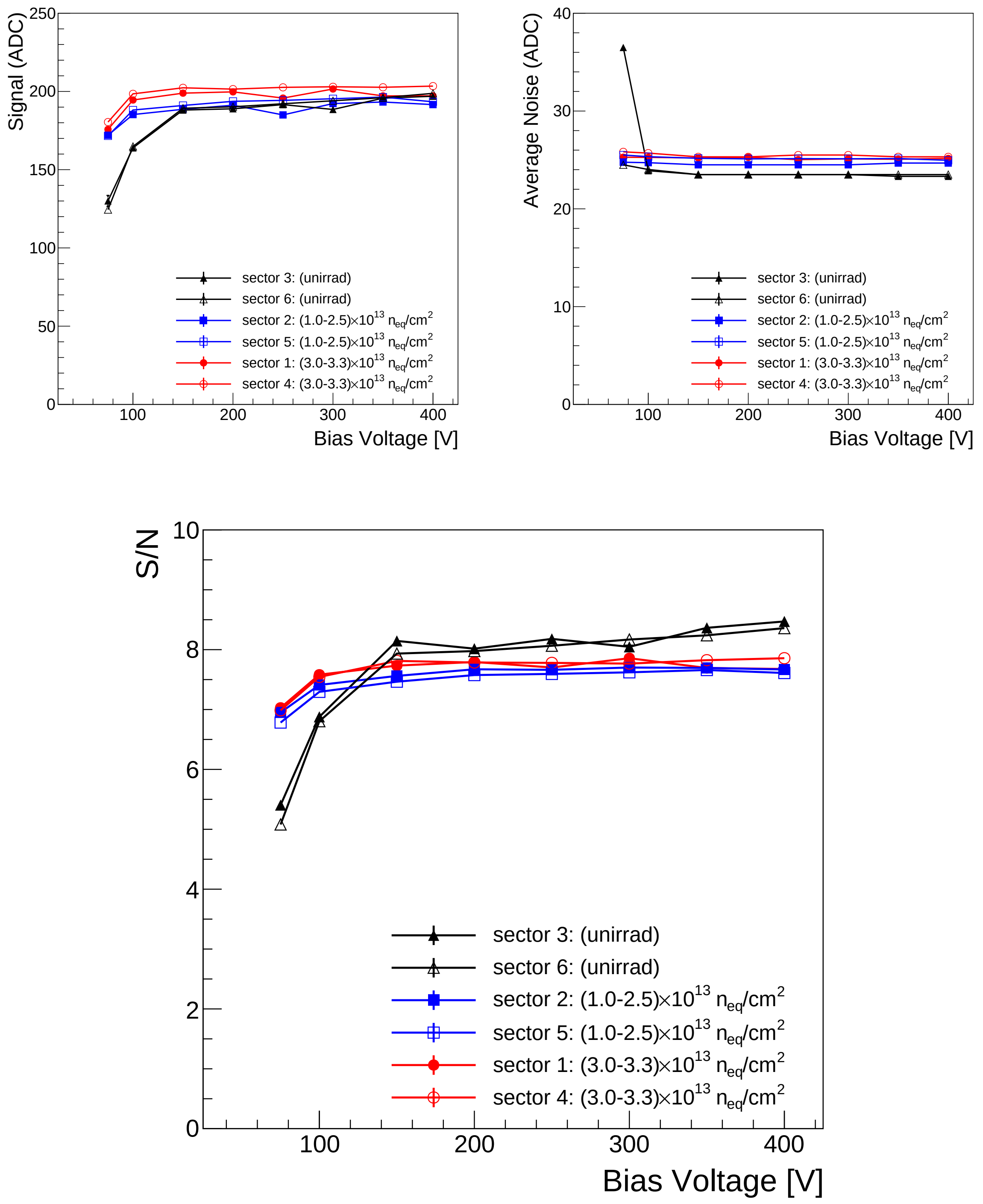

Figure 30: Signal, noise and S/N as a function of bias voltage for each of the 6 sectors, for Board A8 (FanUp).

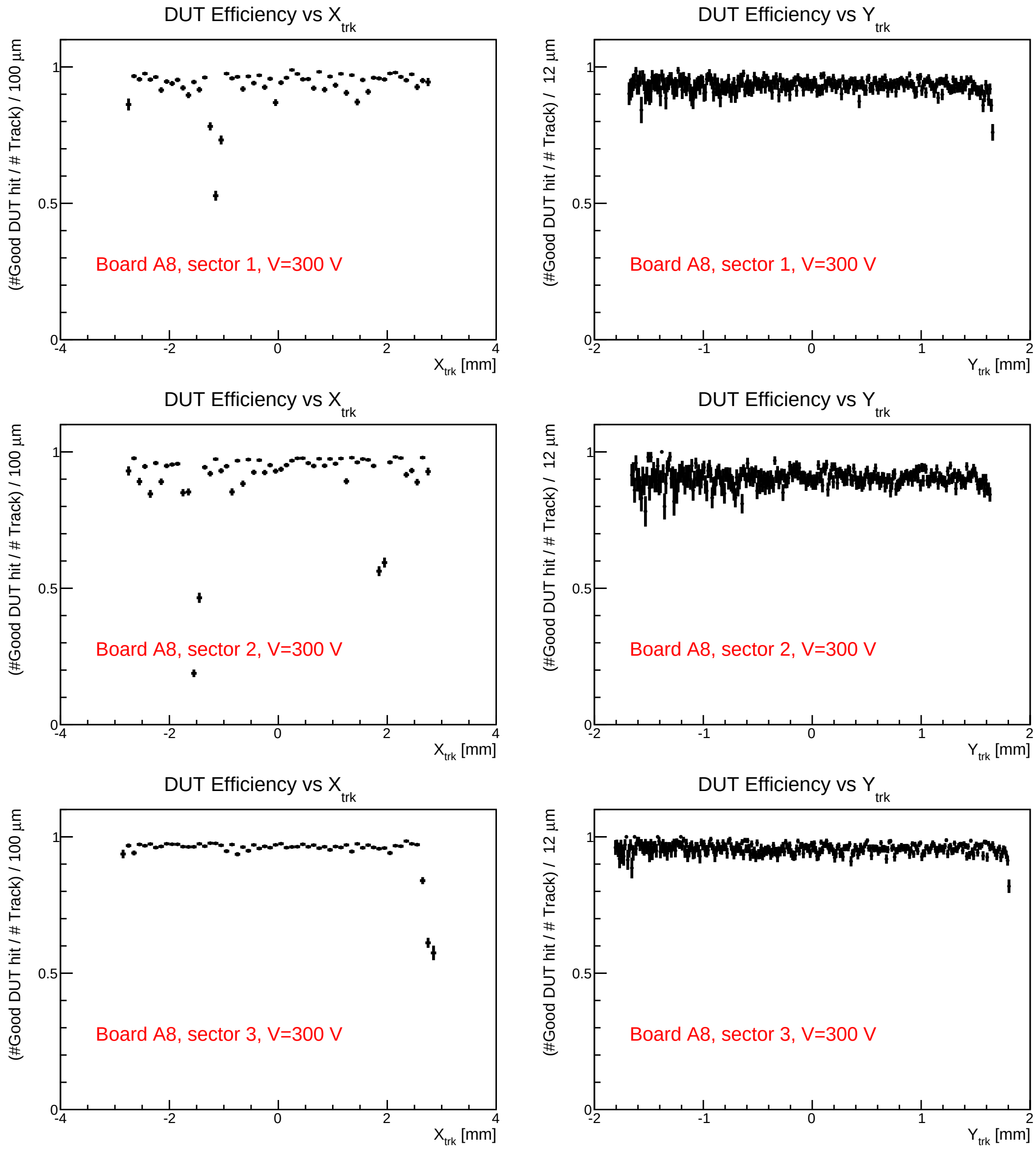

Figure 31: Efficiency as a function of the (left) X and (right) Y coordinate, for sectors 1, 2 and 3, as indicated, for the FanUp sensor.

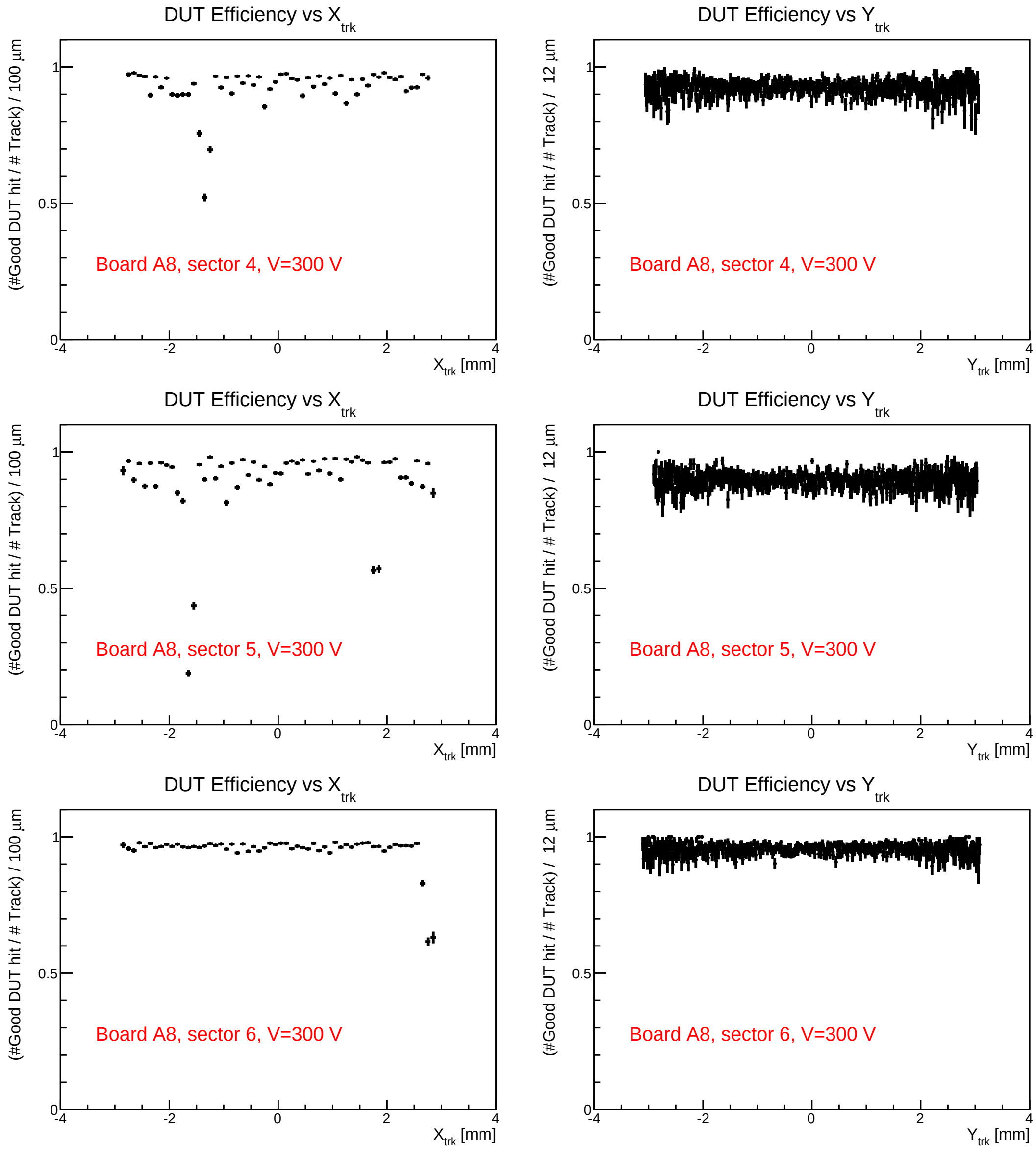

Figure 32: Efficiency as a function of the (left) X and (right) Y coordinate, for sectors 4, 5 and 6, as indicated, for the FanUp sensor.

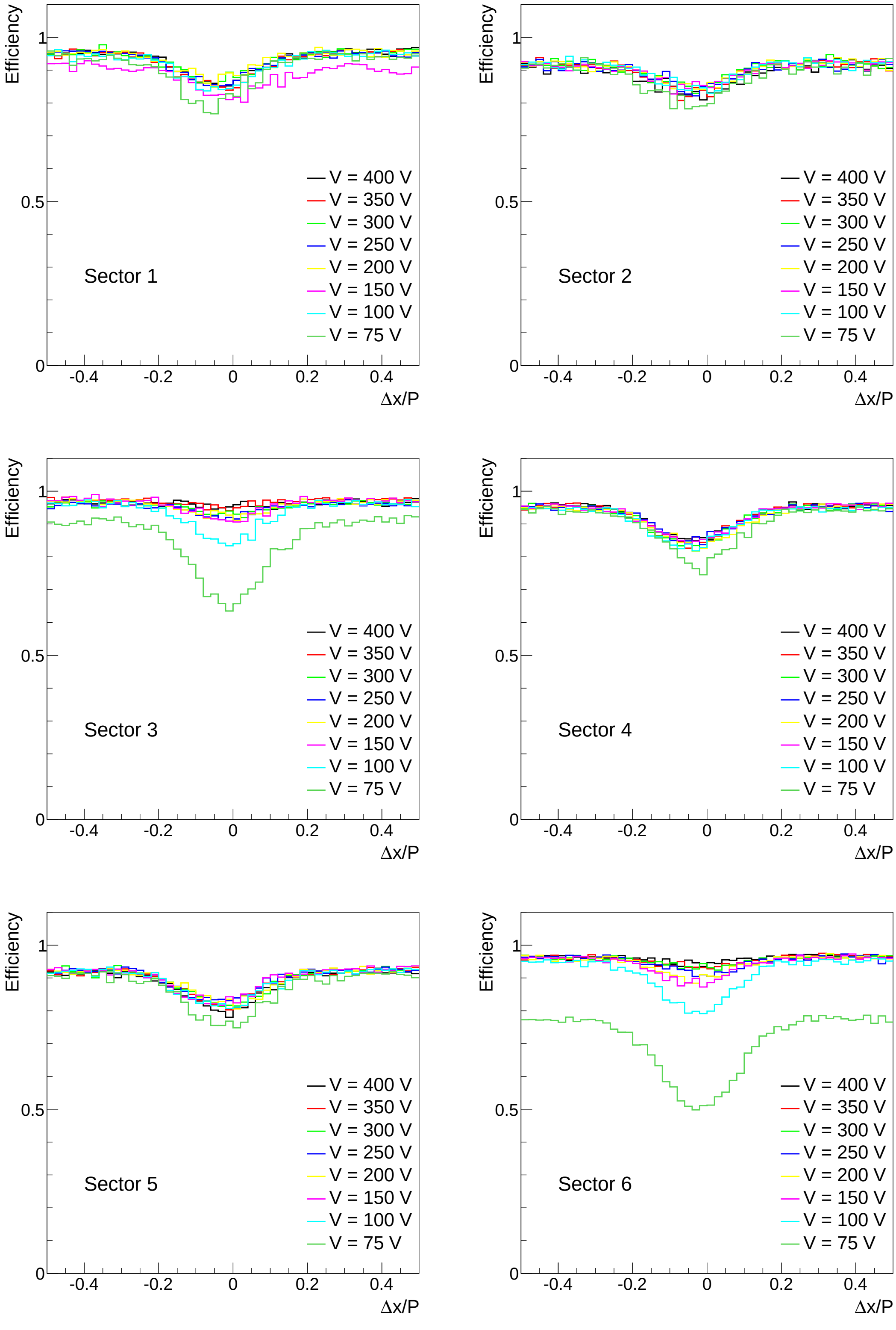

Figure 33: Efficiency versus interstrip position for several bias voltages, and each sector, for the FanUp sensor.

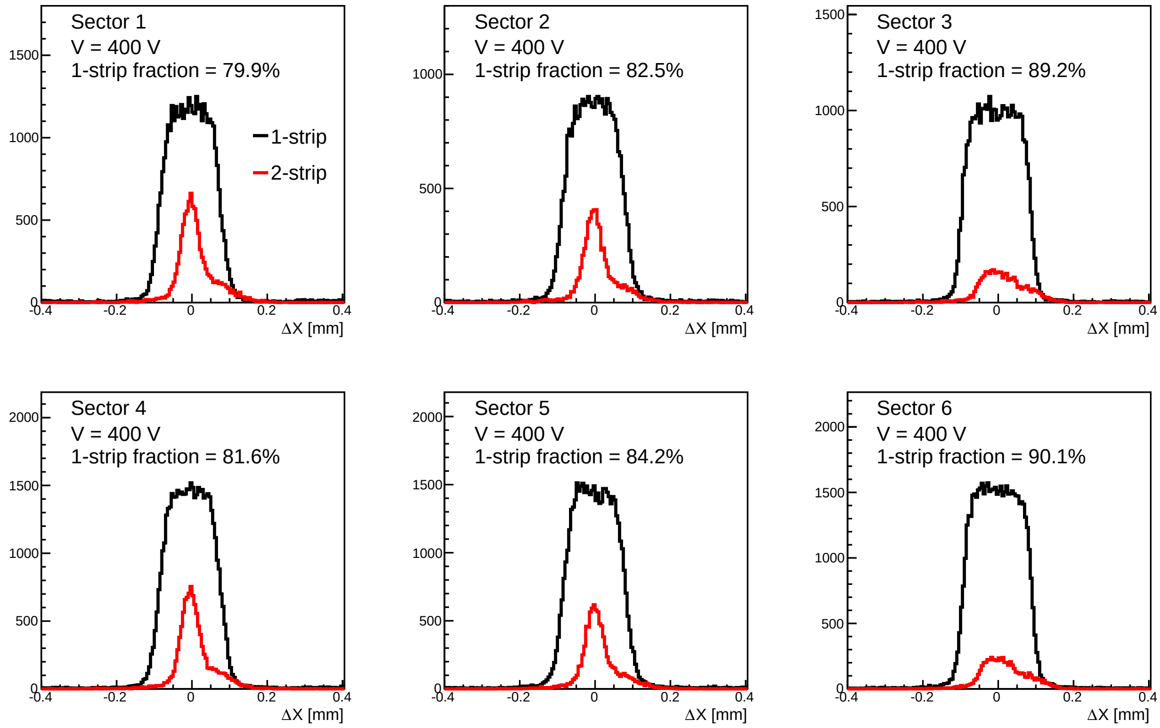

Figure 34: Residuals for 1 and 2-strip clusters for the 6 sectors of the FanUp sensor for tracks at normal incidence.

4.3 Type 1/2A - NoFan sensor (A4)

For this sensor, which we refer to as the NoFan sensor, the readout was on the FanUp side, but the connection was made directly to the 190 μm strips, not through the 75 μm embedded PA. Here we show the same set of plots as shown for the FanUp, but omit the individual Landau fits. The corresponding plots are shown in Figs. 35, 36, 37, 38 and 39. The data for this sensor was also collected in the July 2015 testbeam.

In Fig. 35, it is interesting to note that the signal for sector 6 is lower than all the rest, but so is the noise, so that the S/N is actually in agreement (actually a bit larger) than that of sector 3. This provides additional circumstantial evidence that the gain is somehow not perfectly stable. The S/N though is quite consistent with what is seen in the FanUp and FanIn sensors.

Figures 36 and 37 do not exhibit any dips in efficiency near the top edge, similar to the FanUp readout. The efficiency versus interstrip position also show similar trends to what is seen in the FanUp sensors.

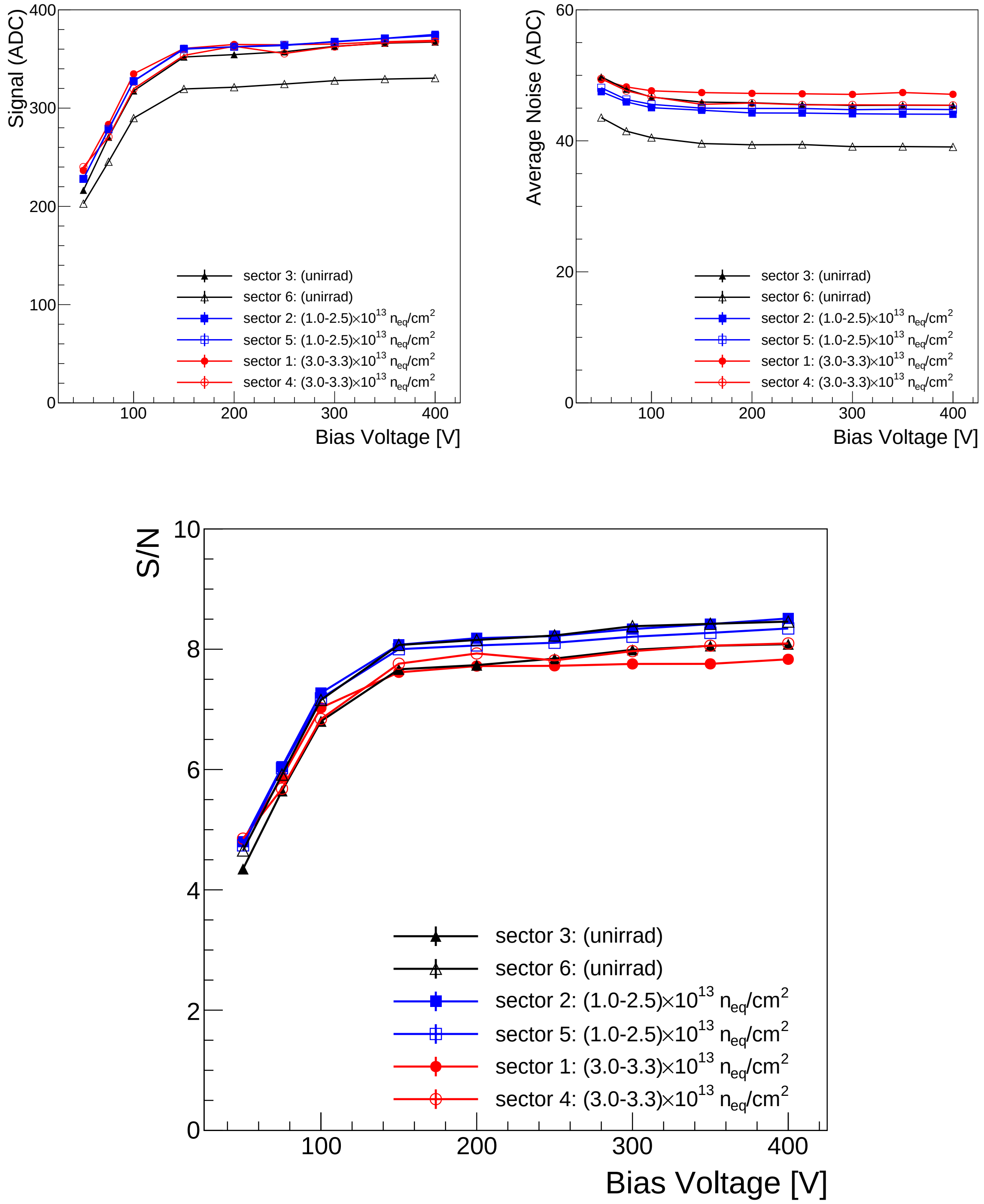

Figure 35: Signal, noise and S/N as a function of bias voltage for each of the 6 sectors, for Board A4 (NoFan).

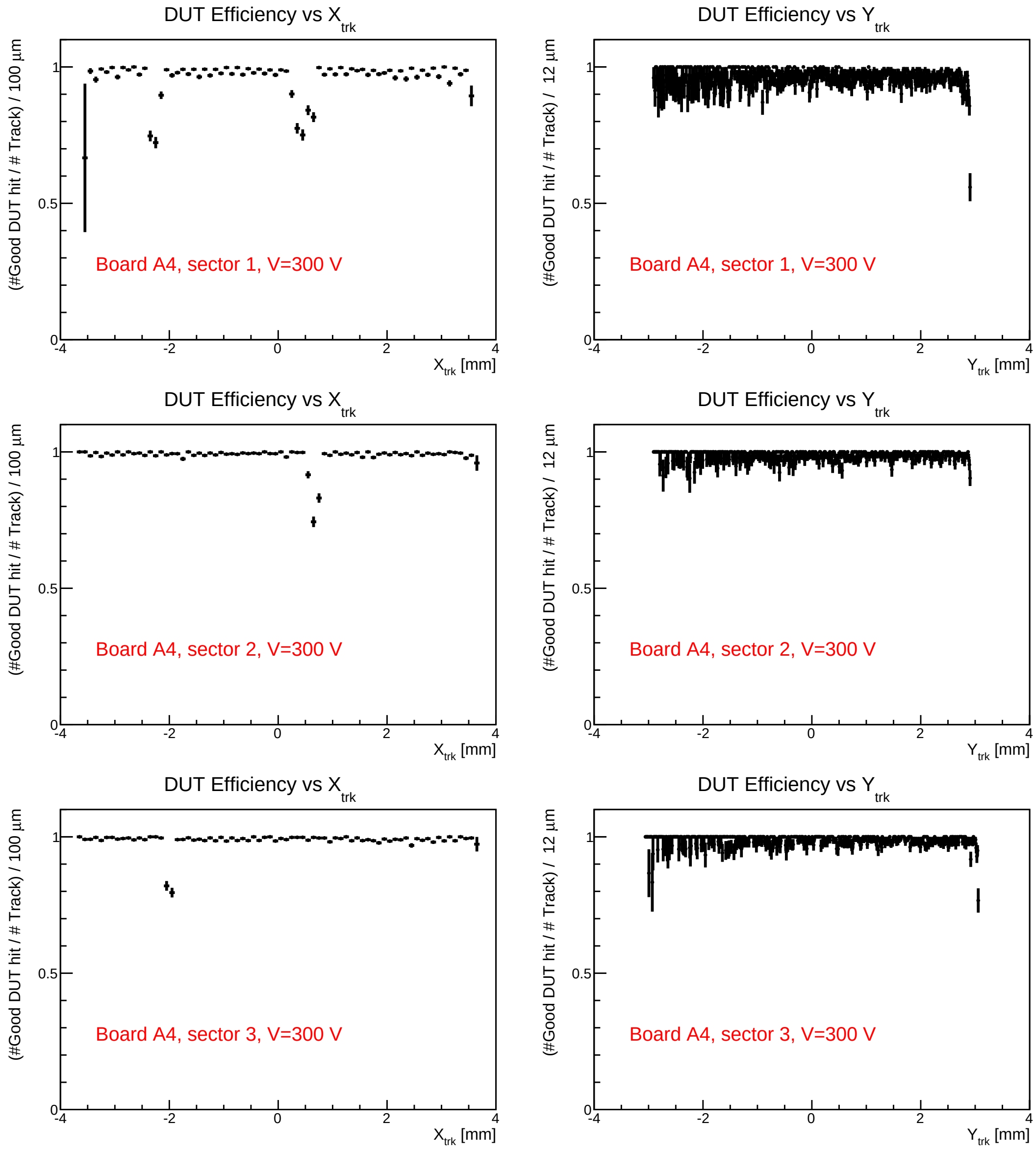

Figure 36: Efficiency as a function of the (left) X and (right) Y coordinate, for sectors 1, 2 and 3, as indicated, for the NoFan sensor.

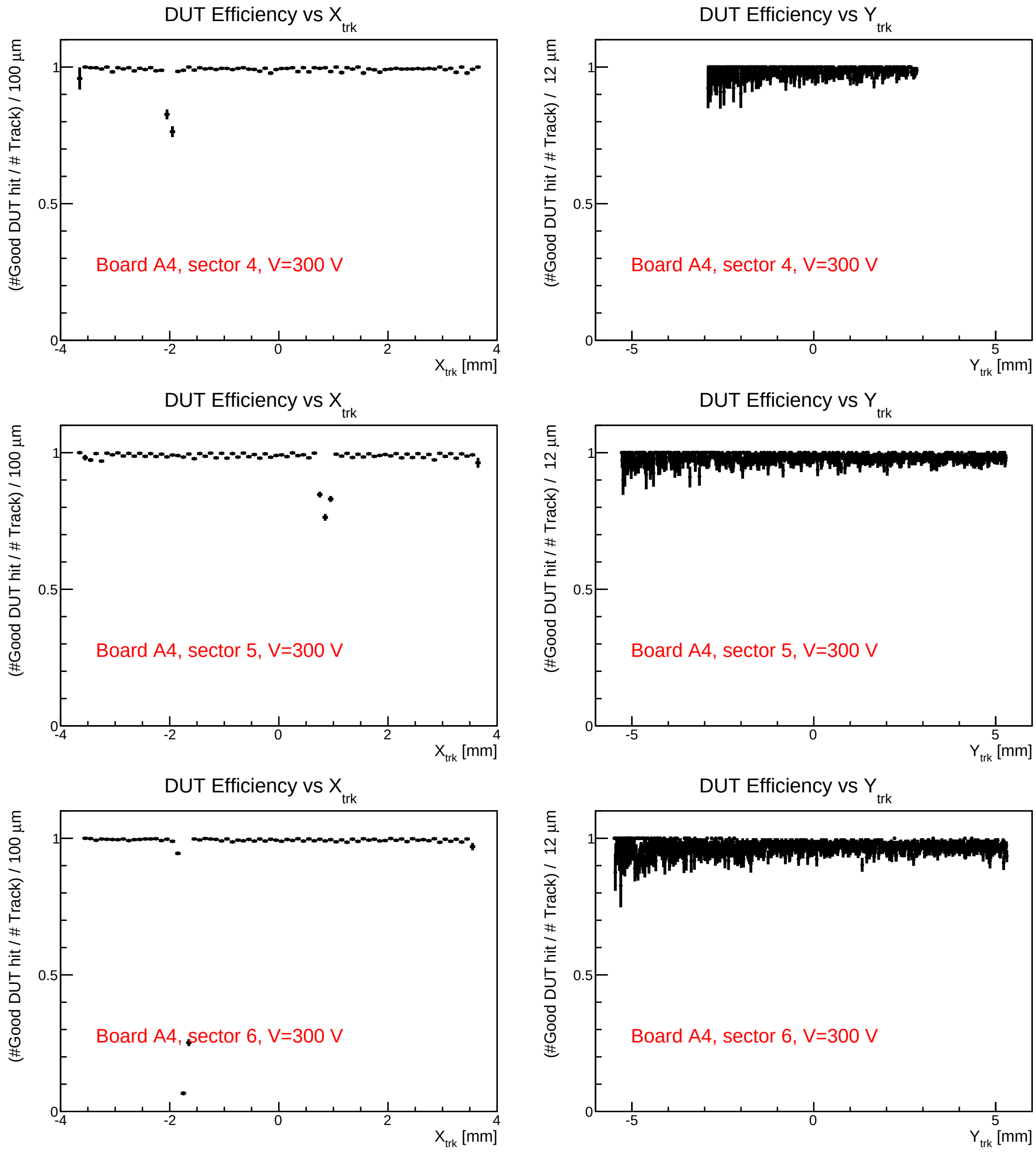

Figure 37: Efficiency as a function of the (left) X and (right) Y coordinate, for sectors 4, 5 and 6, as indicated, for the NoFan sensor.

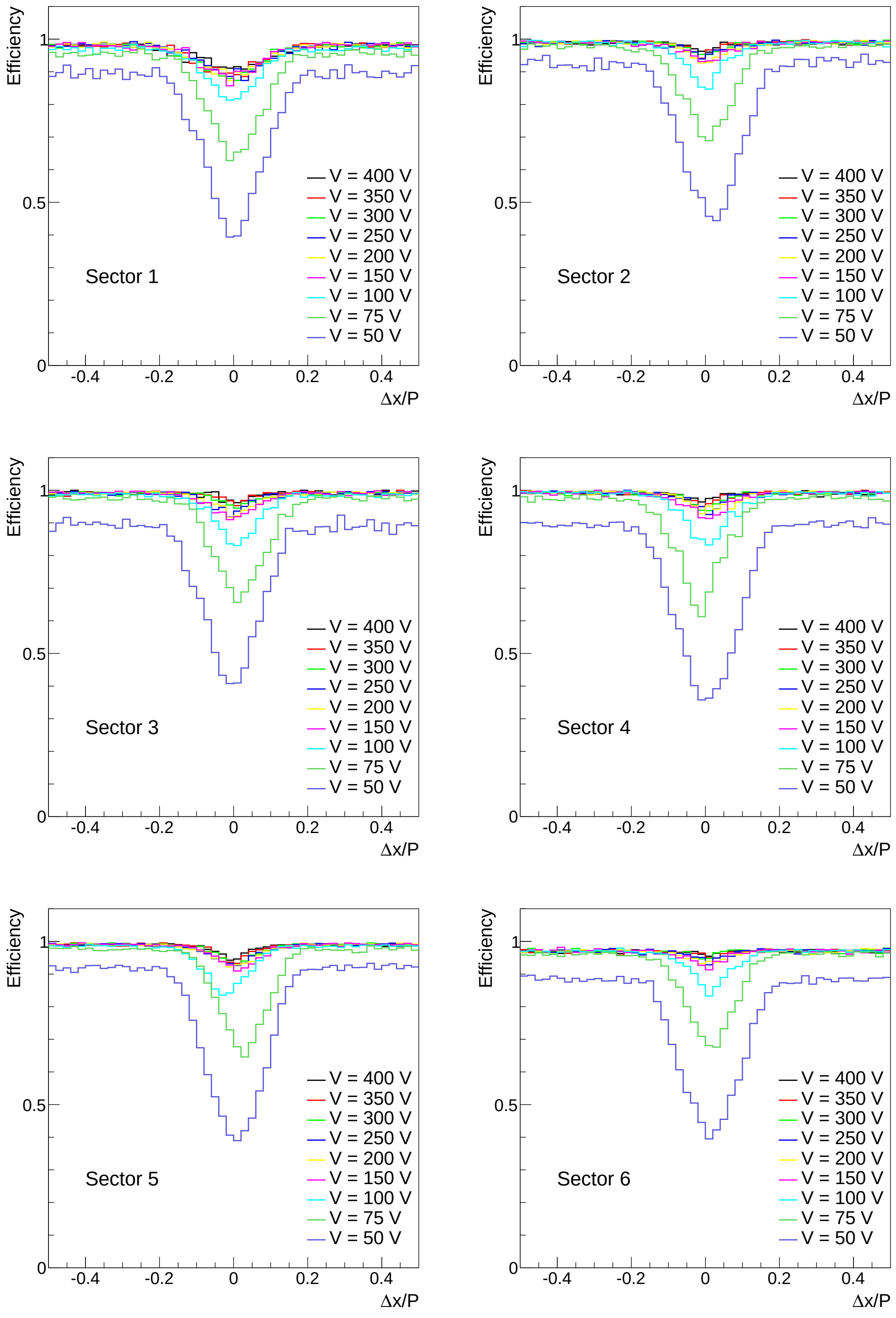

Figure 38: Efficiency versus interstrip position for several bias voltages, and each sector, for the NoFan sensor.

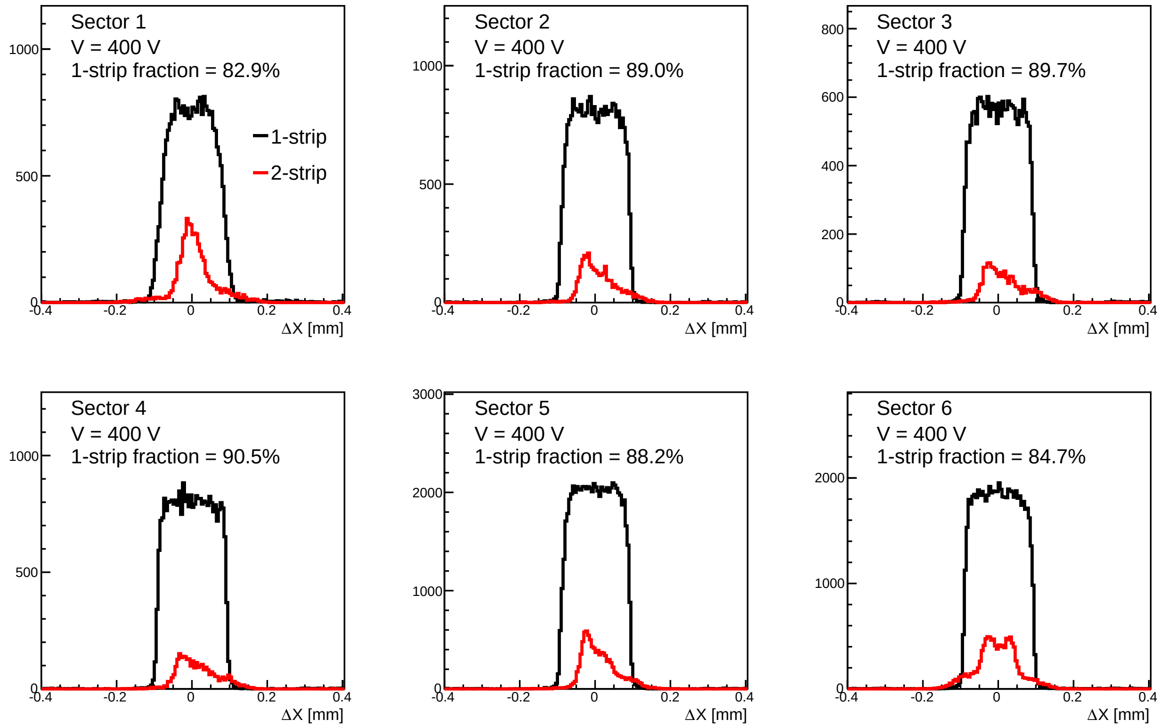

Figure 39: Residuals for 1 and 2-strip clusters for the 6 sectors of the NoFan sensor for tracks at normal incidence.

4.4 Type D sensors

The Type D sensors are the ones closest to the beam pipe, and must withstand the highest radiation fluence, In addition they feature a quarter-circle cutout in order to get as close as possible to the beam pipe. So, the two key features to test for the Type D sensors are the evolution of the S/N as a function of fluence, and the efficiency close to the quarter-circle cutout.

Two irradiated Type D sensors were tested, one in July testbeam (D7), and one in the October (D5) testbeam. First, we do a *side-by-side* comparison of the signal, noise, and S/N, as shown in Fig. 40.

Again, we note that the signal (in ADC counts) is quite different between the D7 and D5 sensors; the former plateaus at about 230 ADC counts, and the latter at about 280. Moreover, on D7, we see that sector 3, which is unirradiated, has a lower signal than sector 2. However, if one looks at the corresponding noise levels, we see that also the noise is considerably lower. As a result, the S/N in the unirradiated section is actually maximum, as one would expect. Focusing only on the S/N results, we see that the unirradiated sensor achieves a S/N of about 17–17.5. A couple of examples of the Landau distributions for D7 sectors 3 and 4 are shown in Figs. 41 and 42.

To compare to the October 2014 testbeam, we simply scale by the ratio of sensor thicknesses of 1.25 (250 μm/ 200 μm), which would imply a S/N of about 21. This is quite consistent with the S/N seen in the unirradiated n-in-p Micron mini sensors tested in the October 2014 testbeam (using the Alibava system).

4.4.1 Efficiency versus interstrip position of Type D sensor

Figure 43 shows the efficiency versus interstrip position for D5 sensor. In general, there is very little loss in the middle between two strips, since the S/N is much higher. Only at low bias voltages, when the S/N is low, does one see a loss in efficiency in this region.

4.4.2 Cluster size and residuals for Type D sensor

Figure 44 shows the residuals between the DUT hit and track for 1 and 2-strip clusters, for each sector. The fraction of 2-strip clusters is larger than for the A-type sensors, as one would expect, here about 30% of the total of 1 plus 2 strip clusters.

4.4.3 Cutout region

Another important aspect to test on the Type D sensors is the efficiency near the cutout region. Figure 45 shows (left) the position (Y vs X of tracks at the DUT when there is a DUT hit within 200 μm of the track's projection for sectors 1, 2 and 3. Note that the cutout region is inverted with respect to what one would find in Fig. 8, since x position increases as you move from right to left in that diagram. Sectors 1 and 3 show some regions where there are noise strips, which results in some entries in the hole region.

The clear absence of hits which form the cutout region is evident. The edge is fit to a second order polynomial; the precision to which this edge is determined is limited by the number of tracks that illuminate the cutout region. For each track, we compute the distance of closest approach to this edge, and then look at the efficiency of finding a hit within 200 μm of the track's projection, as a function of the distance to the fitted edge. Those results are shown on the right. The data are fit to an Error function, and the parameters are shown. The widths of the edge are small, only about 30 μm for sectors 2 and 3, and about 50 μm for sector 1. The larger width of sector 1 is related to the steepness of the edge at sector 1. In either case, there is no indication of a significant region of inefficiency near the cutout region. Also, sector 1, which is the highly irradiated region, has an efficiency that plateaus at about the same value as the less irradiated sector 2 and unirradiated sector 3.

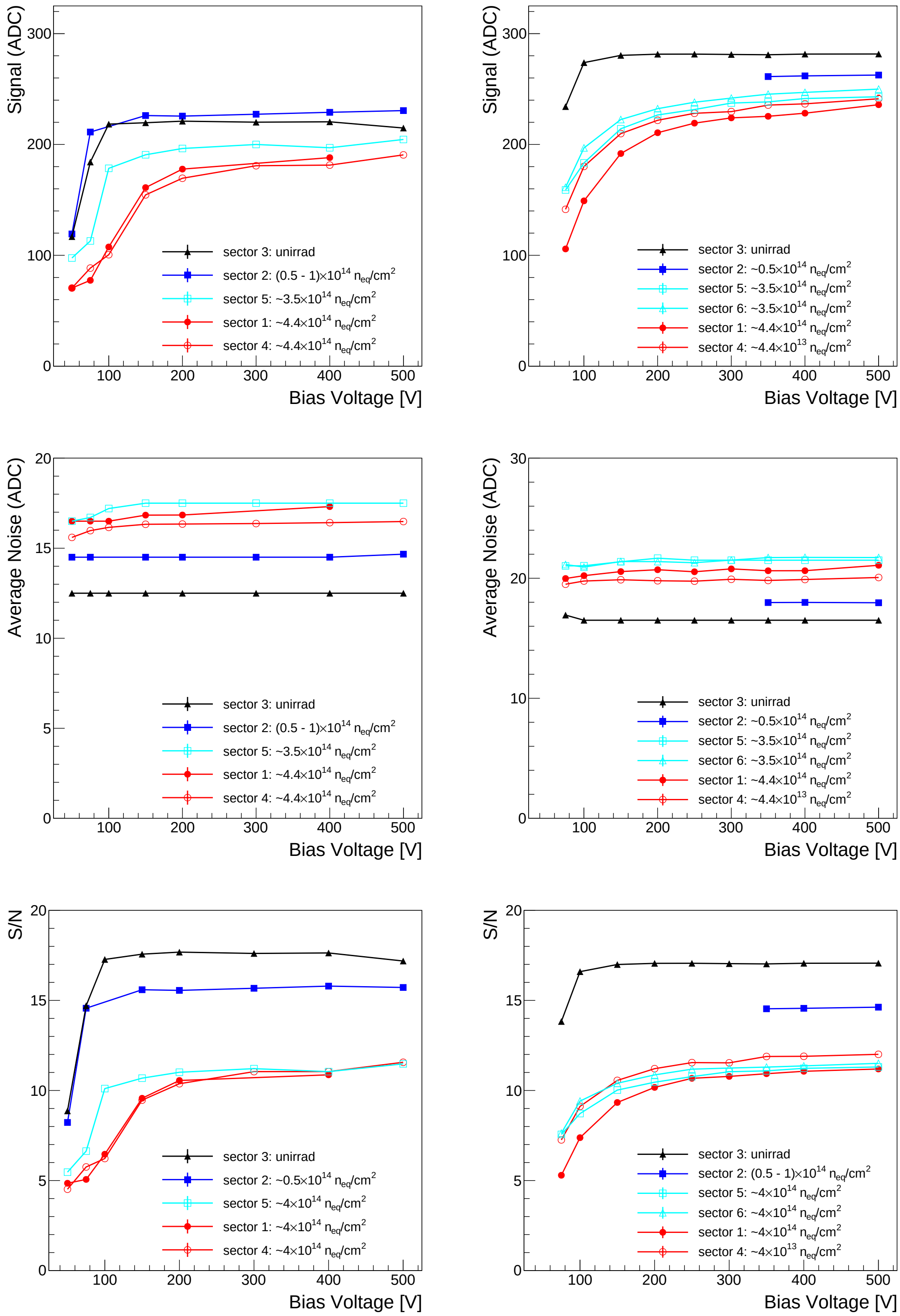

Figure 40: Signal (top), noise (middle) and S/N (bottom) for the sensors D7 (left), and D5 (right).

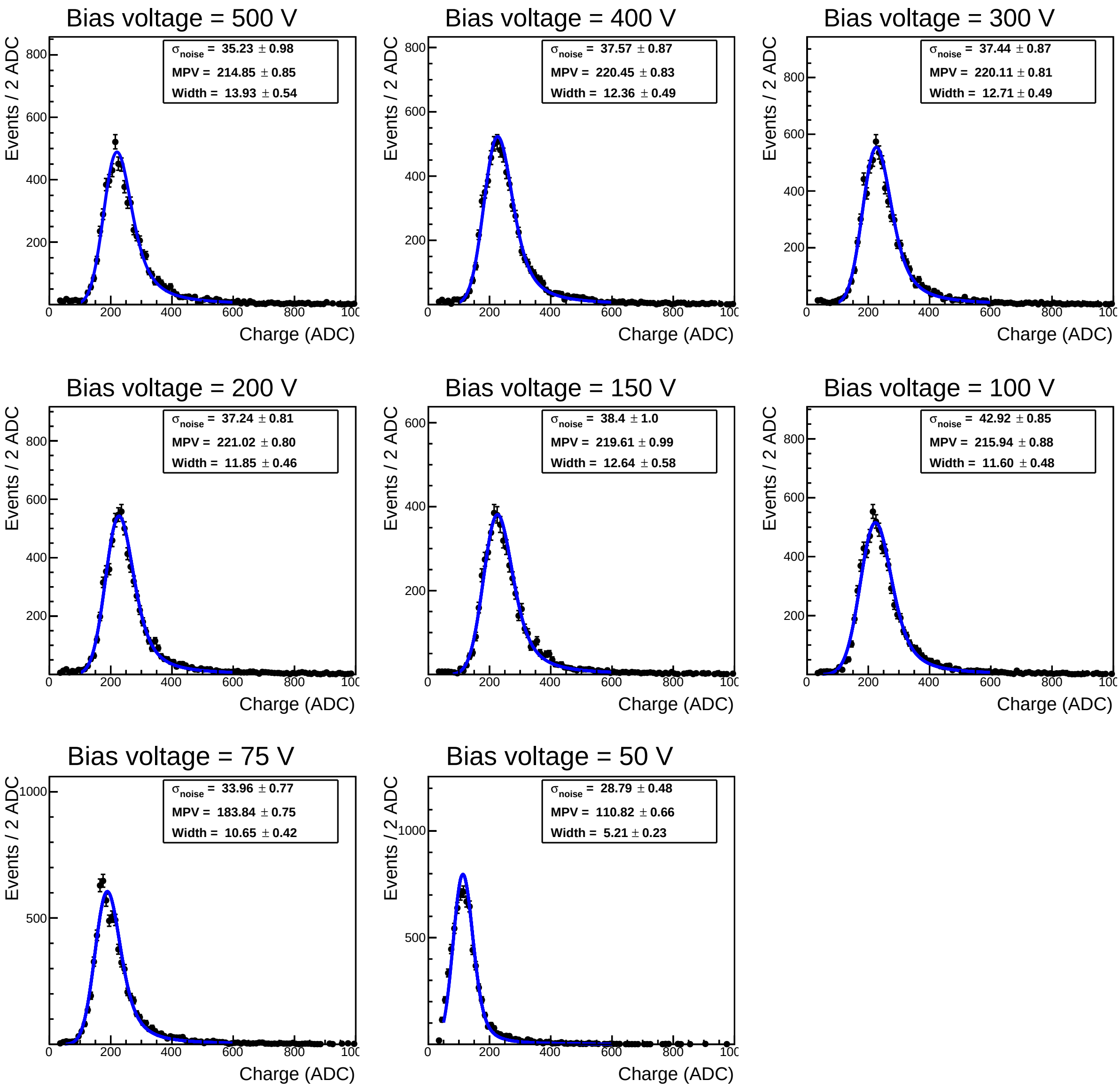

Figure 41: Charge collected in sector 3 of the Type D sensor (D7) for several bias voltages from 50 V to 500 V. Fits to the data using a Landau distribution convolved with a Gaussian function are overlaid.

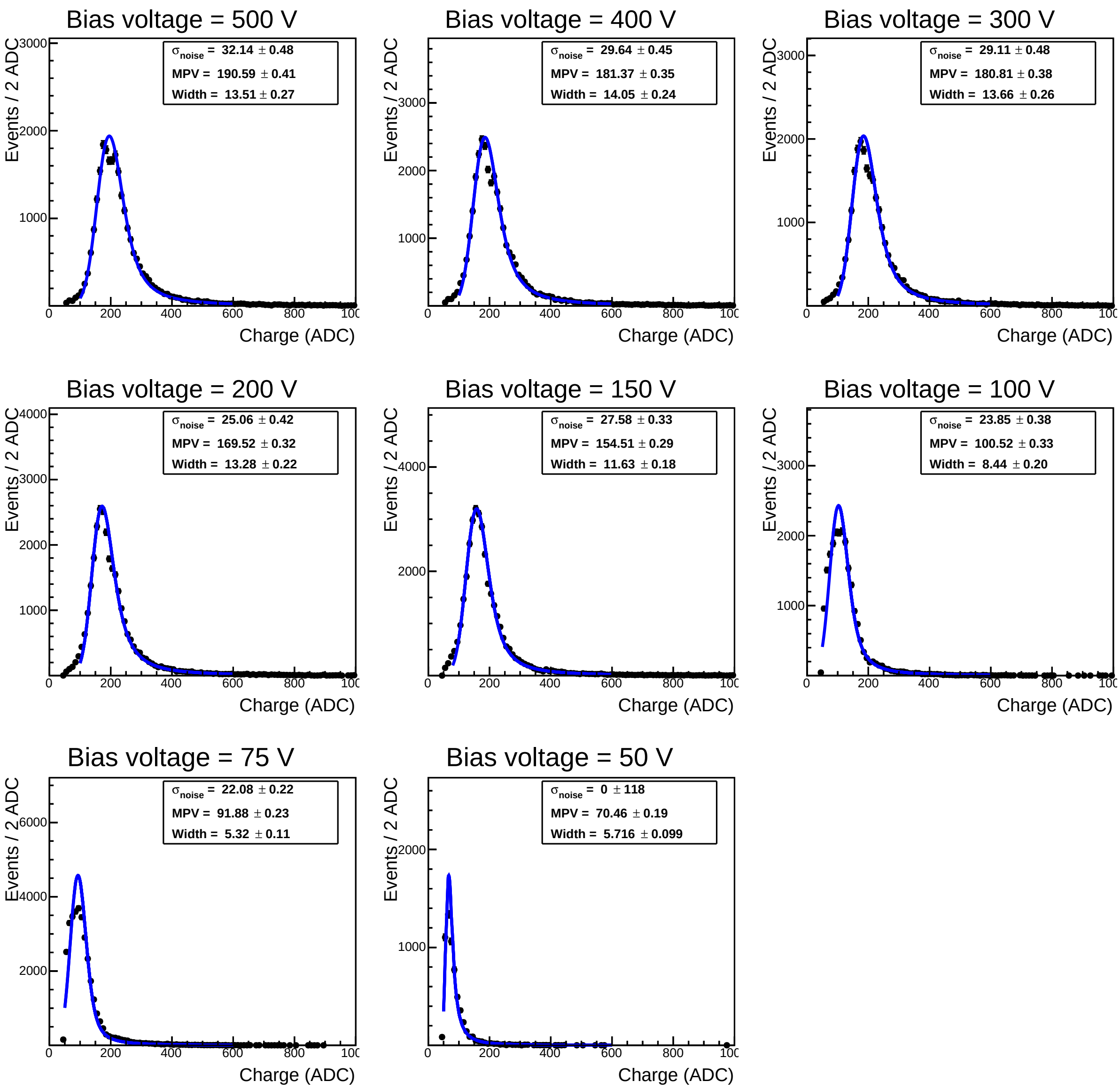

Figure 42: Charge collected in sector 4 of the Type D sensor (D7) for several bias voltages from 50 V to 500 V. Fits to the data using a Landau distribution convolved with a Gaussian function are overlaid.

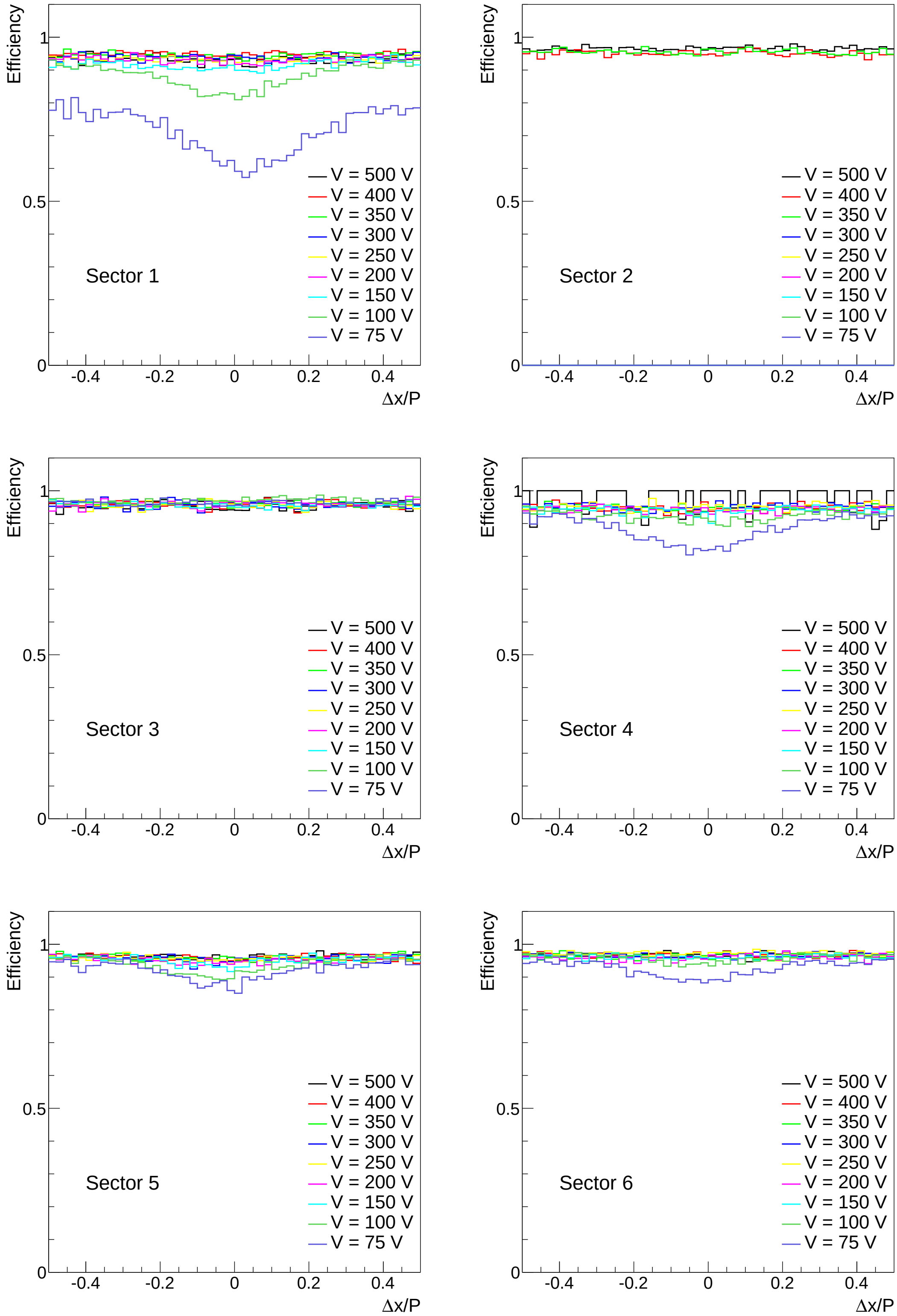

Figure 43: Efficiency versus interstrip position for several bias voltages, and each sector, for Type D (D5) sensor.

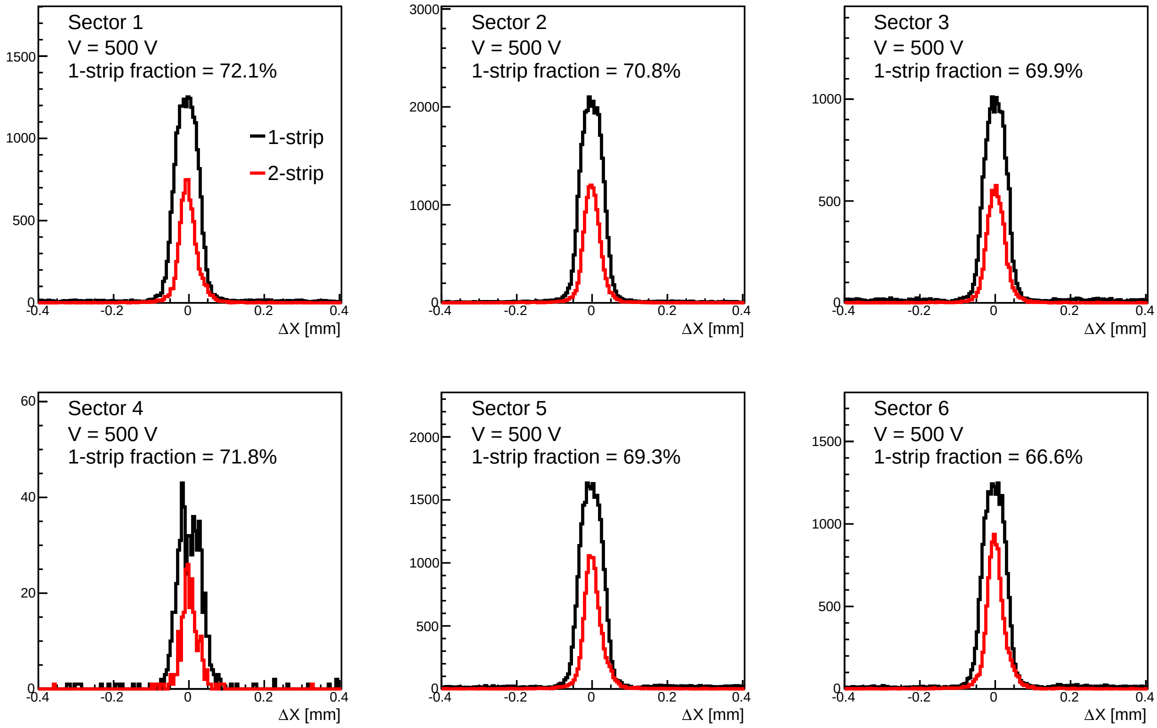

Figure 44: Residuals for 1 and 2-strip clusters for the 6 sectors of the Type D sensor for tracks at normal incidence for board D5.

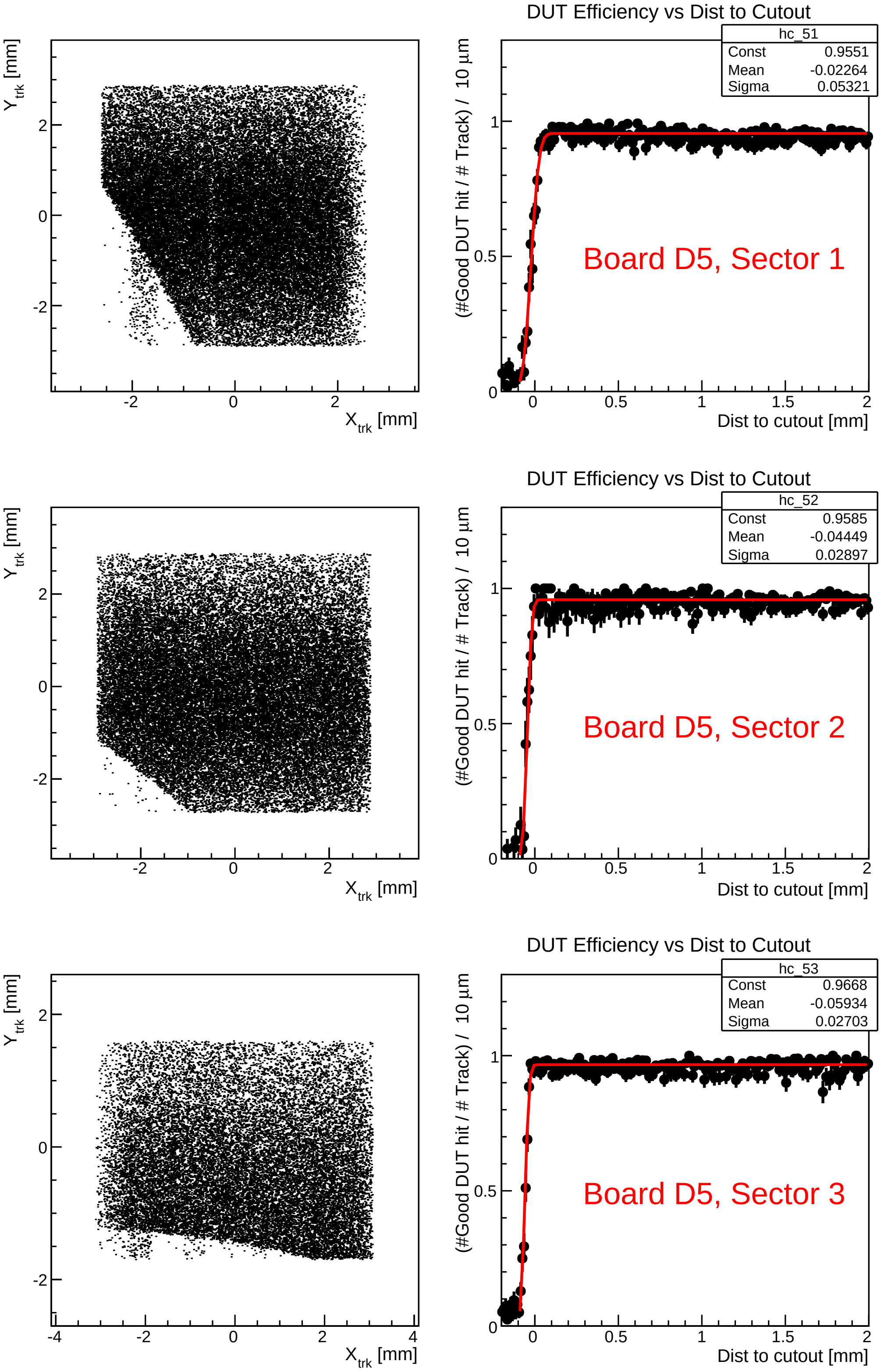

Figure 45: (Left) Position of tracks (Y vs X) when there is DUT hit within 200 µm of the track's projection, for (top) sector 1, (middle) sector 2, and (bottom) sector 3. On the right are the corresponding plots of efficiency versus distance to the cutout region.

4.5 Topside vs backside biasing

One of the design features to test was the performance of irradiated sensors biased via the backside of the sensor (backside biasing) versus biasing via the topside contact (topside biasing). For the topside biasing, the bias is brought to the back side of the detector by making the edge of the sensor conducting. For backside biasing, the back must be unpassivated, and the connection is made through direct contact of the back side of the sensor with a gold contact that is at voltage.

Thus far, all tests shown are for sensors using the topside contact, but the sensors are only irradiated in a specific region, which is not near the topside contact.

Many sensors, both Hamamatsu and Micron, were irradiated in October 2015, but due to time and manpower constraints, only a couple were able to be tested. In the November 2015 testbeam we were able to put Type A mini-sensors from Hamamatsu in the beam. The mini-sensors are about 1.8 cm long and about 1.4 cm wide, and 250 μm thick. They are all Type A detectors, and are wirebonded view the FanUp PA side to Beetle chips on TT hybrids. The FanIn side was on the opposite end, and that area was not moved into the beam due to limited manpower and time.

The four sensors tested are:

- 2 sensors irradiated to 1.1×10^{14} n_{eq} cm^{-2}, one biased by the topside contact, and the other via direct connection to the backside metallization.
- 2 sensors irradiated to 6.4×10^{14} n_{eq} cm^{-2}, one biased by the topside contact, and the other via direct connection to the backside metallization.

Upon inspection, it was found that most of the bias scan runs for the backside biasing at 6.4×10^{14} n_{eq} cm^{-2} are corrupted. In particular, the bias runs from 25 V to 250 V have clearly corrupted header bits. The runs at 300 and 350V look reasonable, at least the header bits seem to not show anything strange.

We also found that for the backside biasing runs at 1.1×10^{14} n_{eq} cm^{-2}, the DUT and TimePix do not appear to be synchronized in time, and therefore we cannot use tracking information for cluster selection. Therefore, to make a *like-for-like* comparison for the topside ve backside biasing at 1.1×10^{14} n_{eq} cm^{-2}, we carry out the analysis without using tracks to select clusters. In practice, the bias due to using all clusters, which does include some noise clusters, is small.

4.5.1 Backside vs topside bias at 1.1×10^{14} n_{eq} cm^{-2}

Figure 46 shows the signal, noise and S/N as a function of bias voltage for the (left) backside biasing and (right) topside biasing schemes for the n-in-p Hamamatsu mini-sensor. The S/N reaches a bit over 16 in both cases. The shapes are very similar. As can be seen, the S/N in the topside bias scheme is slightly larger than in the backside biasing, but this is well within the systematic uncertainties of the measurements.

The Landau distributions for each of the voltage points are shown in Figs. 47 and 48.

4.5.2 Backside vs topside bias at 6.4×10^{14} n_{eq} cm^{-2}

As mentioned above, we can only get a full bias scan for the topside biasing scheme at the fluence of 6.4×10^{14} n_{eq} cm^{-2}. The signal, noise and S/N as a function of bias voltage are shown in Fig. 49. The S/N reaches about 10-11. The drop at the highest of voltage seems to be due to an increase in the noise. Thus, we see a sizable drop in S/N at this fluence, which is about 30 times larger than the maximum expected dose in the Type A sensors, and about 50% larger than expected in the Type D sensors. The Landau distributions are shown in Fig. 50.

For the backside biasing, only a few runs at the maximum voltage were not corrupted. We have looked at three runs, all at a bias of 300 V. In the nominal case, the normal to the detector has a nominal angle of 0^o with respect to the beam; the other two had nominal angles of $\pm 1^o$. These angles are small enough such that the path length through the silicon should not increase the charge significantly. The resulting signal, noise and S/N are indicated in Table 3. The S/N is in the same range as was seen for the topside biasing scheme.

Table 3: The signal, noise and S/N in the sensor A2, sector 1, at 300 V, which is biased directly on the backside of the sensor. The sensor was irradiated to a fluence of 6.4×10^{14} n_{eq} cm^{-2}.

Angle	Signal (ADC)	Noise (ADC)	S/N
-1	250	24.6	10.2
0	256	24.1	10.6
+1	261	23.8	11.0

We can semi-quantitatively compare the S/N we get here in the mini-sensors with the Type D sensors. If we assume the decrease in S/N is approximately linear from 16.5 at 1.1×10^{14} n_{eq} cm^{-2}. to 10.5 at 16.4×10^{14} n_{eq} cm^{-2}, we would estimate a S/N of 13.8 at 4.0×10^{14} n_{eq} cm^{-2}. This is consistent with the value of about 13.1 found for the D Type sensors, after multiplying the S/N found in those studies by 1.25 to account for the fact that these mini-sensors are 250 µm thick, versus 200 µm for the Type D. The sensors here are 190 µm pitch and 1.8 cm long, versus 5 cm long and 95 µm pitch, so one would not expect them to have the same performance. However, it is interesting to note that the two do give similar S/N performance.

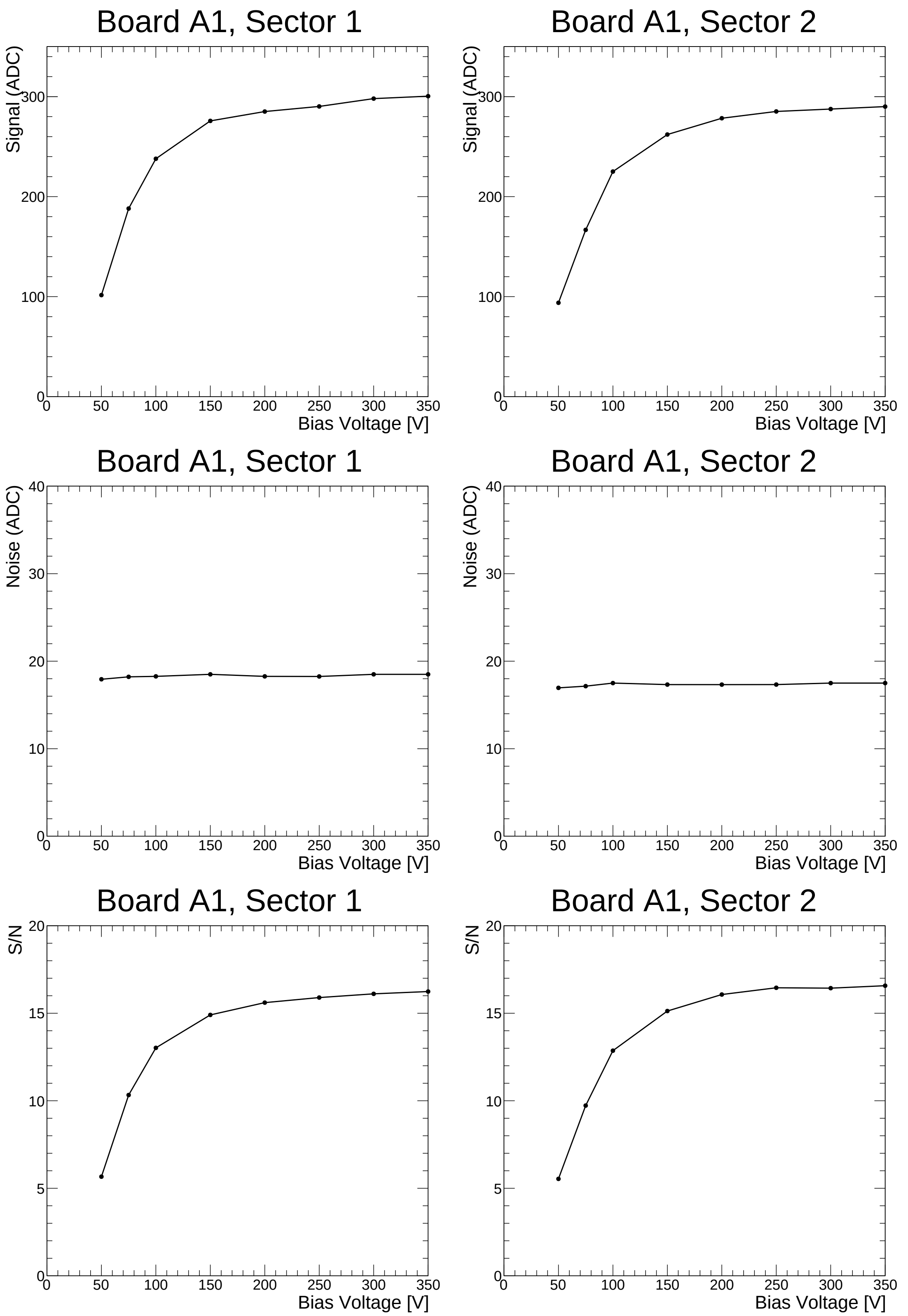

Figure 46: Signal (top), noise (middle) and S/N (bottom) for the Hamamatsu mini-A sensor, irradiated to a fluence of 1.1×10^{14} n_{eq} cm^{-2}, using (left) backside biasing, and (right) topside biasing.

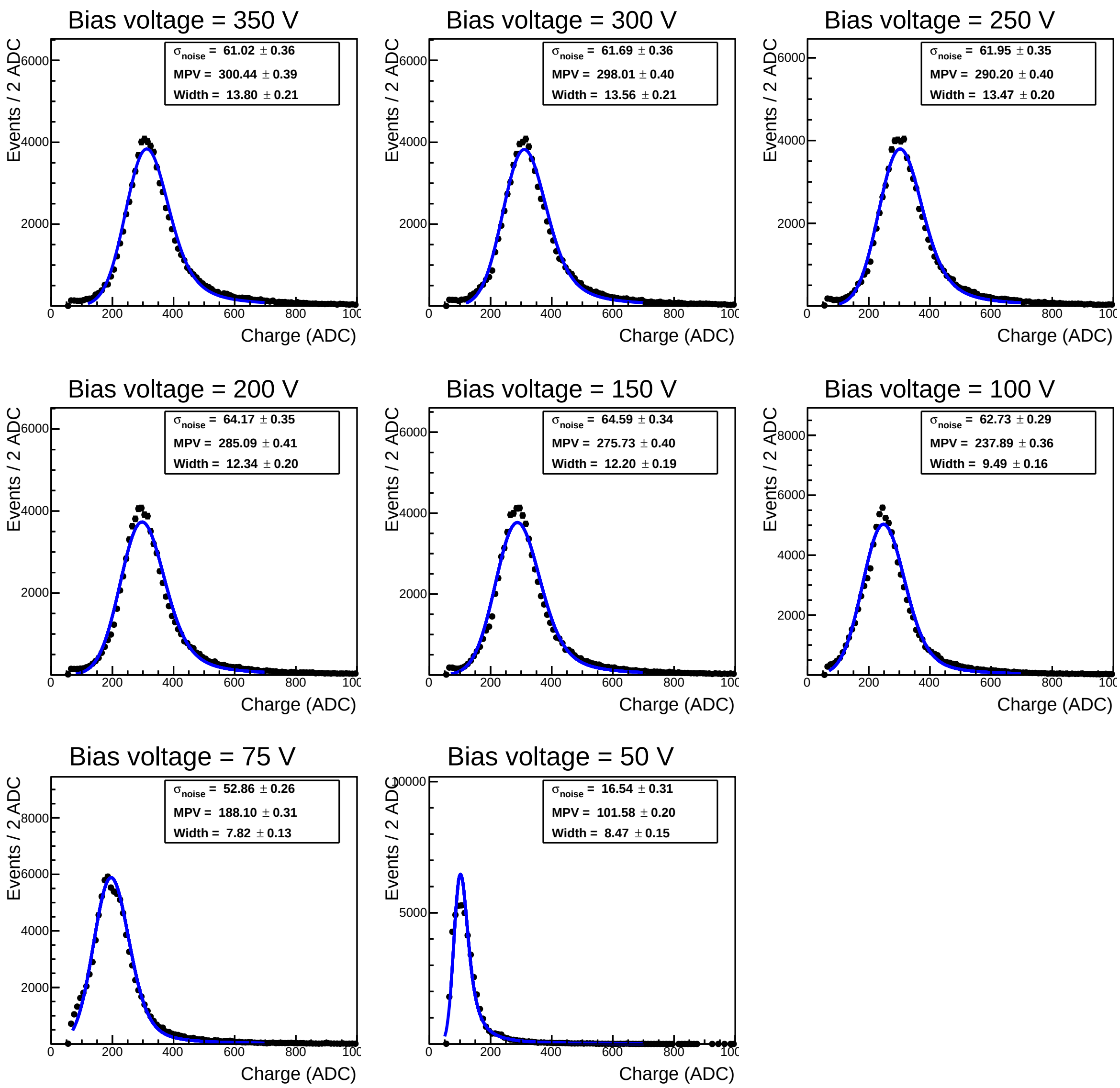

Figure 47: Landau distributions for the sensor A1 sector 1, which is biased via a direct contact to the backside of the sensor. The sensor has been irradiated to $1.1 \times 10^{14}\ n_{eq}\ cm^{-2}$.

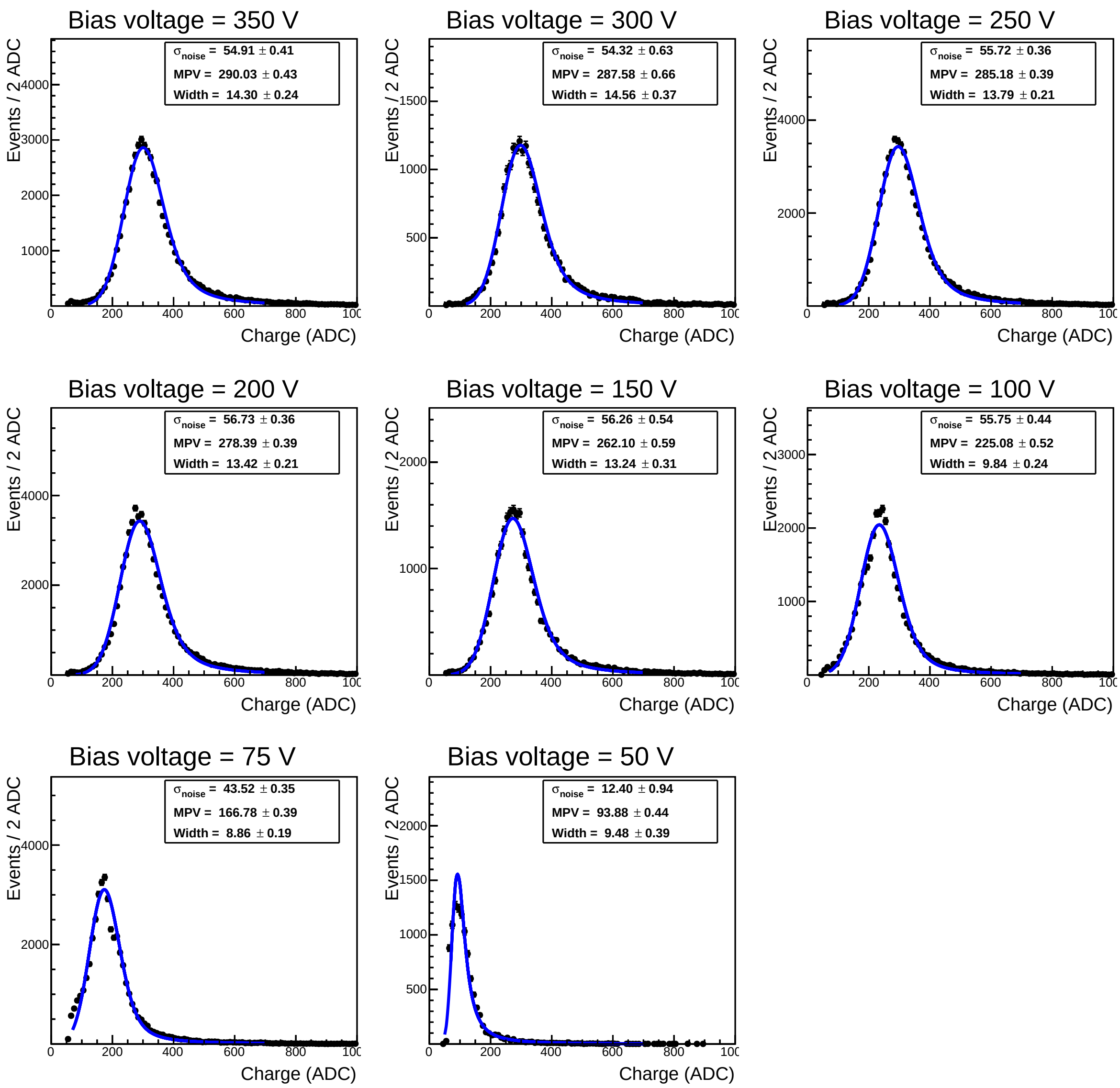

Figure 48: Landau distributions for the sensor A1 sector 2, which is biased via the topside contact. The sensor has been irradiated to $1.1 \times 10^{14}\ n_{eq}\ cm^{-2}$.

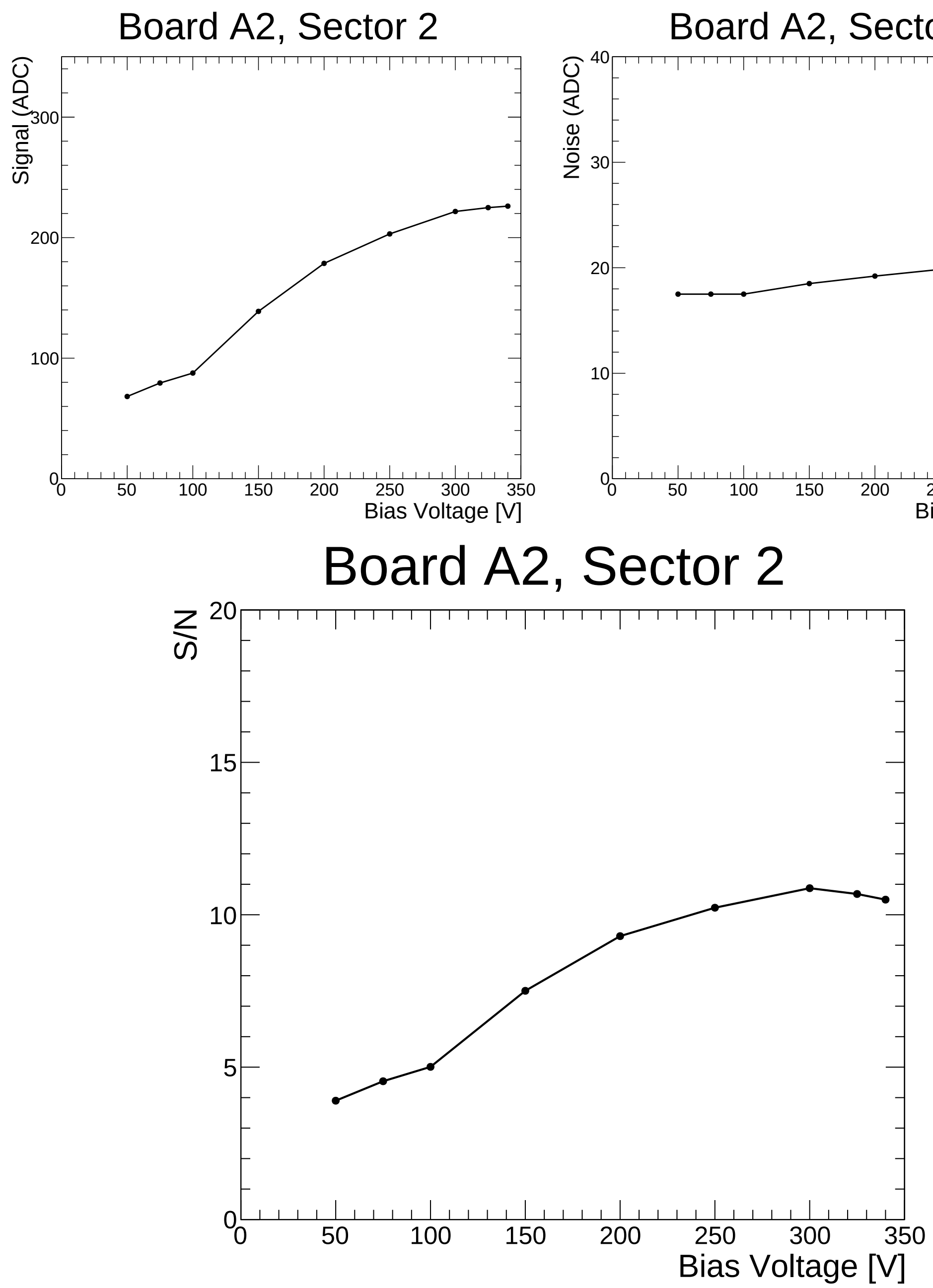

Figure 49: Signal (top), noise (middle) and S/N (bottom) for the Hamamatsu mini-A sensor, irradiated to a fluence of $6.4 \times 10^{14}\ n_{eq}\ cm^{-2}$, using topside biasing.

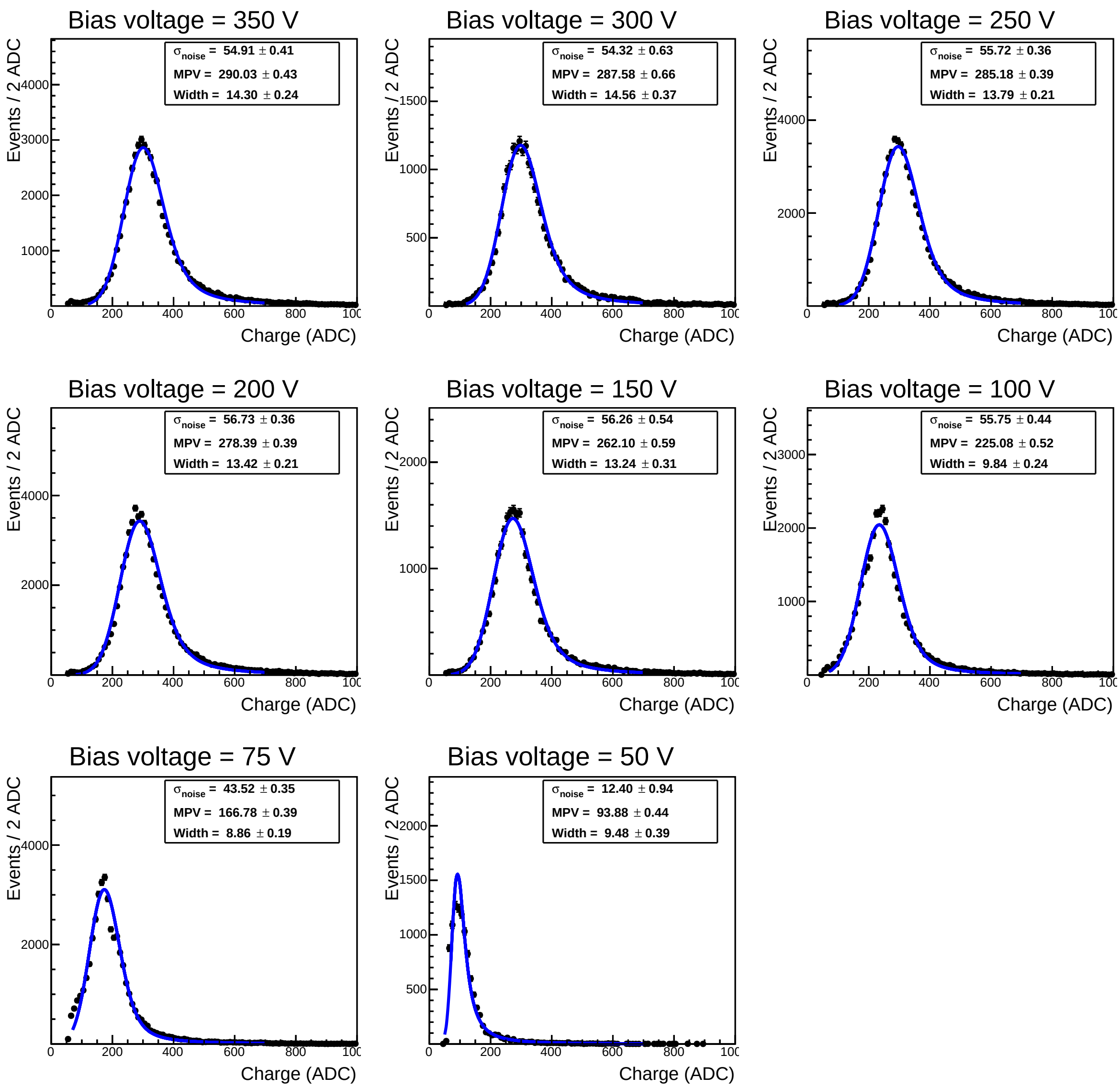

Figure 50: Landau distributions for the sensor A2 sector 2, which is biased via the topside contact. The sensor has been irradiated to $6.4 \times 10^{14}\ n_{eq}\ cm^{-2}$.

5 Discussion and summary of results

Several types of n-in-p prototype UT sensors were tested during three 2015 testbeam campaigns. These included 1/2-width Type A and full size type D sensors, both of 200 μm thickness, and mini sensors that were 250 μm thick. We have learned the following from these studies:

- The n-in-p FanIn Type A sensor suffers from an inefficiency in the middle region between adjacent strip, precisely where the second metal layer crosses the strips. The charge is picked up on other strips, but generally the amount collected in any strip is below the clustering threshold. As a result we have almost zero efficiency in this region.
- The n-in-p FanUp sensor does not suffer any observable inefficiency near the top edge of the sensor.
- The Type A sensors show a S/N of about 8.5 for unirradiated portions, and 7.5 at 0.3×10^{14} n_{eq} cm^{-2} fluence. These values are substantially lower than the Type D, which gives S/N values from about 16 (unirradiated) to 11 (4.0×10^{14} n_{eq} cm^{-2}). Another way to view this is to consider that the signal in a 200 μm thick sensor should peak at about 15,000 e^-. Thus a S/N of 8.5 would imply the Type A sensors have a noise of about 1900 e^-, and the Type D sensors have a noise of about 940 e^-.
- The Type D sensors show good S/N performance, which ranges from about 17 (no irradiation) to about 11 (maximum fluence). Scaling to 250 μm thickness implies a S/N that is at least 14, which would give good performance over the life of the sensor.
- In the Type D sensors, we see no long range inefficiency near the 1/4-circle cutout.
- Preliminary tests of topside vs backside biasing show no difference in performance between the two biasing schemes.

A few questions remain, which will be the focus of the 2016 testbeams, particularly the first one in May. They include:

- Does the inefficiency seen in the n-in-p FanIn sensor in the region of the embedded PA also occur for p-in-n sensors? This is an important question to answer since the p-in-n technology can be used for the Type A sensors, and knowing that both the FanIn and FanUp are equally good would provide better more options for UT. It is also of academic interest to better understand the loss in efficiency observed in the n-in-p sensors, since it was unexpected.
- Why is the S/N of the Type A sensors only about 7.5–8.5? It appears that the noise in the Type A sensors is significantly larger than in the Type D, and it seems unlikely to be just due to the larger capacitance of the type A sensors. Is there a significant

contribution from the second embedded PA on the Type A? Also, the Type A sensor when paced on the Aluminum holder has a substantial amount of aluminum behind the sensor backplane. Could this be contributing additional capacitance/noise? We plan to remove much of the aluminum behind the Type A sensor in case this is an issue. More bench tests prior to the testbeam are critical to understand and reduce any additional coherent noise sources.

- We need to perform additional testing of the topside versus backside biasing on p-in-n sensors.

The results of the 2015 testbeam and the anticipated studies in the 2016 testbeams should provide us with the key information needed to move forward with the UT sensor quotations in mid-2016.

Acknowledgements

We express our gratitude to our colleagues in the CERN accelerator departments for the excellent performance of the SPS, which allowed this data to be collected. We also are grateful to the TimePix group for providing support for usage of the TimePix telescope, with which some of the studies presented here would not have been possible. Among the TimePix group, we espeically thank Heinrich Schindler, Martin van Beuzekom for their tireless efforts during the testbeam period, and Tim Evans for his support in using the offline Kepler software.

A Static properties of Hamamatsu and Micron sensors

Described in this section is the measurements of the static properties of irradiated Hamamatsu and Micron silicon micro-strip sensors. The details of the irradiation campaigns of these sensors at the IRRAD facility at CERN is described in Section 2.2. Table 4 describes the various detector geometries and technologies tested. In total, 15 Hamamatsu “full” size and mini-sensors and 28 Micron mini-sensors were irradiated up to 2.1E15 1MeV neutron equivalent per cm^2 and tested of its static properties the laboratory. In the following sections there is no separation of the various TTT8 designs unless explicitly noted.

Table 4: Summary of Hamamatsu and Micron mini-sensors tested after irradiation. Note here the full size D sensors and several TTT8 mini-sensors also include a 1/4 circular beampipe cutout (MBP=mini beam pipe cutout)

Manufacturer	Name	Type	Backside Passivation	Thickness (μm)	Pitch (μm)	Width (μm)
Hamamatsu	1/2A	n-in-p	Yes	200	190	80
Hamamatsu	Full size D	n-in-p	Yes	200	95	60
Hamamatsu	mini-A	n-in-p	Yes	250	190	80
Hamamatsu	mini-A	n-in-p	No	250	190	80
Hamamatsu	mini-D	n-in-p	Yes	250	95	60
Hamamatsu	mini-D	n-in-p	No	250	95	60
Micron	TTT8	p-in-n	No	300	40	8
Micron	TTT8	p-in-n	No	300	80	30
Micron	TTT8 MBP	p-in-n	No	300	80	30
Micron	TTT9	n-in-p	No	250	80	16

A.1 Experimental setup

Measurements of pre-irradiation leakage currents and capacitance versus voltage were performed at the Syracuse university laboratory. The Syracuse probe station is enclosed in a light tight box. Sensors are held to the probe chuck using a vacuum pump. There is no temperature control of the Syracuse setup but the temperature is measured at each measurement for reference. Dry air is pumped into the box to produce a dry environment and the relative humidity is also monitored during each measurement. Leakage current measurements are done using a Keithley 237 SMU. Capacitance measurements are done using a Quadtech 7600 model b LCR meter, while the Keithley 237 is used to bias the detector. Measurements are automated using LabView software.

All post-irradiation measurements were performed at the RD50 laboratory at CERN. The RD50 probe station is enclosed also in a light tight box. Sensors are held down to the probe chuck using a vacuum chuck. The chuck is manufactured by systems ATT and is liquid cooled, able to reach temperatures less than -20C. Dry air is flushed in the box to produce a dry environment before and during cooling. Leakage currents are performed using a Keithley 237 SMU to bias the detector and a Keithley 2410 picometer to measure the leakage current. Capacitance measurements are performed using a Keithley 237 to bias the detector and a Agilent E4980A precision LCR meter. Measurements are automated using LabView software.

A.2 Leakage current

To compare leakage current measurements before and after irradiation, and between the Syracuse and RD50 measurements, leakage currents pre-irradiation were scaled to T=-5C using the conventional leakage current scaling equation [12]:

$$I_2 = I_1(\frac{T_2}{T_1})^2 \cdot e^{-\frac{E_{gap}}{2k_b}(\frac{1}{T_1}-\frac{1}{T_2})}, \quad (1)$$

where $I_{1,2}$ and $T_{1,2}$ are the leakage current and temperature (in Kelvin), respectively, before and after scaling, and E_{gap} and k_b are the bandgap energy and Boltzmann's constant, respectively. Here a value of 1.21 for the bandgap energy is used to scale leakage currents measurements. A temperature of T=-5C was chosen for comparison because this is the nominal operating temperature of the sensors in the UT detector, and this is the temperature all post-irradiated detectors were measured at. All measurements were made to at least a bias of 500V, as this is maximum operating voltage of the UT system.

Leakage current measurements of Hamamatsu mini, and 1/2A and full size D sensors, before and after irradiation, are shown in Figures 51 and 52, respectively. All mini-sensor pre-irradiation currents were on the order of a few nano Amps up to 500V, with the exception of a two detectors that had an onset of soft breakdown beforehand. 1/2A and full size D detectors had a pre-irradiation current of around 10 nA up to the depletion voltage (≈200V) then have a slight turn on after 200V and increase almost an order of magnitude at 800V. After irradiation, both 1/2A and full size D, and all mini-sensors have leakage currents that scale as expected with the average dose received over the detector. There is no sign of (soft) breakdown in all the detectors up to the maximum operating voltage. The splitting of the leakage current of 1/2A and full size D detectors is assumed to be an effect of small differences in the vertical irradiation profile due to the stacking and rotating of detectors during irradiation.

Leakage currents of Micron mini-sensors after irradiation can be seen in Figure 53. Leakage currents per individual fluences are shown in Figure 55. One can see in general a better performance of the p-type detectors over n-type after irradiation, particularly at the highest fluence where the n-type detectors behave almost linearly after a bias voltage of 100V. This was expected as p-type detectors are know to be more radiation hard. All pre-irradiation currents ranged from a few nA to several 10nA and nearly all mini-sensors had (soft) breakdown before 500V (See Figure 54).

In a later section the change in leakage current versus integrated dose will be studied in more detail.

A.3 Capacitance versus voltage

Capacitance versus voltage measurements were measured using a frequency of 1000Hz at both Syracuse and RD50 laboratories.

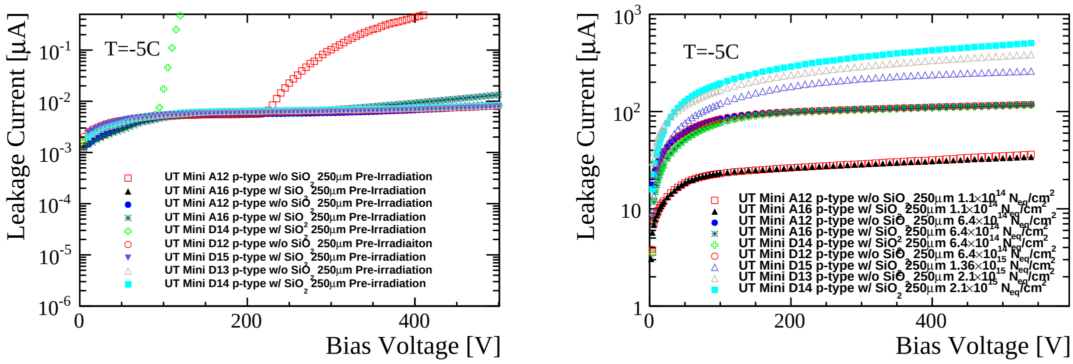

Figure 51: Leakage current of Hamamatsu 1/2A (left) and D (right) sensors. Each plot shows the leakage current before and after irradiation. Here the post-irradiation leakage current is measured at T=-5C where the pre-irradiation measurement is done at room temperature and scaled to T=-5C using equation 1. In the post-irradiation plot, each band shows the different level of irradiation (1.1E14, 6.4E14, 1.36E15, and 2.1E15 n_{eq}/cm^2).

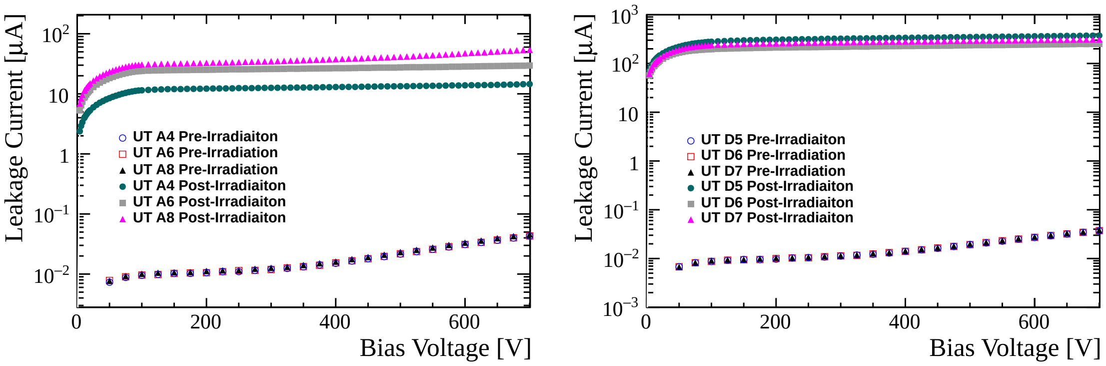

Figure 52: Leakage current of Hamamatsu mini-sensors before (left) and after (right) irradiation. Here the post-irradiation leakage current is measured at T=-5C where the pre-irradiation measurement is done at room temperature and scaled to T=-5C using equation 1. Type 1/2A and full size D detectors were irradiated to a maximum fluence of 2.0E13 and 4.6E14 n_{eq}/cm^2, respectively.

Shown in Figure 56 is the CV measurements made on pre and post-irradiated type 1/2A and D detectors. In these detectors it is clear that they reach depletion around 145V pre-irradiation, but post-irradiation curves don't show a clear indication when the detector is full depleted. This is expected since these detectors were irradiated non-uniformly and most of the detector is not irradiated at all. CV measurements of Hamamatsu mini-sensors irradiated to all fluences are shown in Figure 57. While the depletion voltage as a function of dose will be evaluated below for all sensors, one feature to be noted is the "inverse" behavior of capacitance versus bias voltage of sensors with backside passivation at moderate

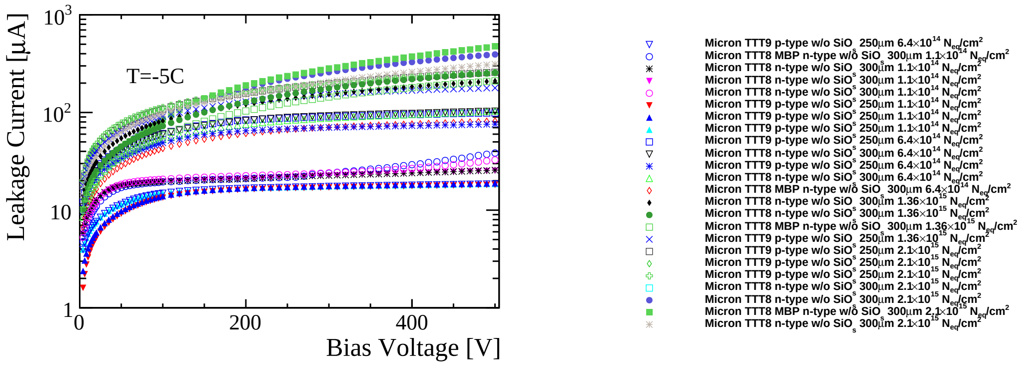

Figure 53: Leakage current of Micron mini-sensors after irradiation. Here the post-irradiation leakage current is measured at T=-5C and all irradiation levels, and sensor geometries and technologies are shown.

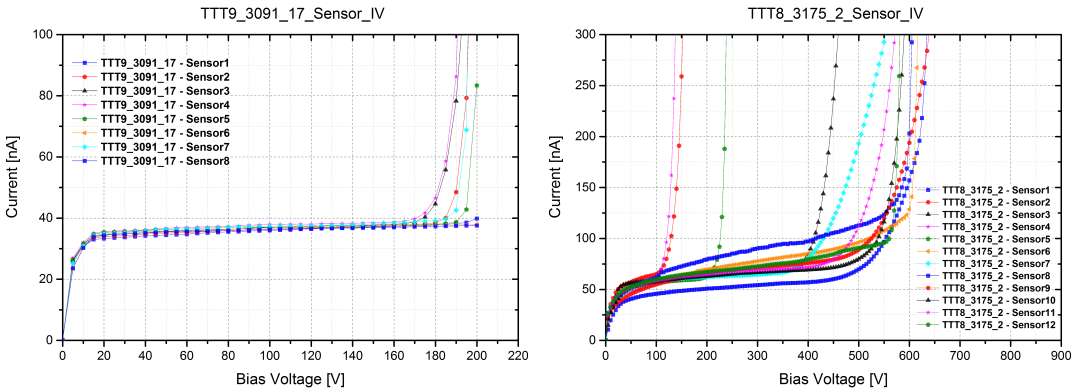

Figure 54: Pre-irradiation leakage current of Micron mini-sensors. Shown on the left is several TTT9 mini-sensors from one wafer and on the right TTT8 mini-sensors from one wafer.

fluences. It is expected that capacitance decreases with voltage due to the increase in space-charge region of the p-n junction, and levels off as the detector reaches full depletion, but sensors with backside passivation, and hence biased from the top, rapidly drop off and slowly increase until leveling off at full depletion. This effect was tested and reproduced on an irradiated detector without backside passivation but biased from the topside contact. Figure 58 shows the this measurement on a Hamamatsu mini-sensor irradiated to 2.1E15 n_{eq}/cm^2. This effect is not completely understood and deserves more attention in future studies/simulations. CV measurements on Micron mini-sensors are shown in Figure 59. Measurements of all unirradiated detectors are not all shown as they consistent with each other and is, therefore, redundant showing all CV plots. One CV curve of each type is given below.

The depletion voltage for each sensor type was estimated from fitting the log(C) versus

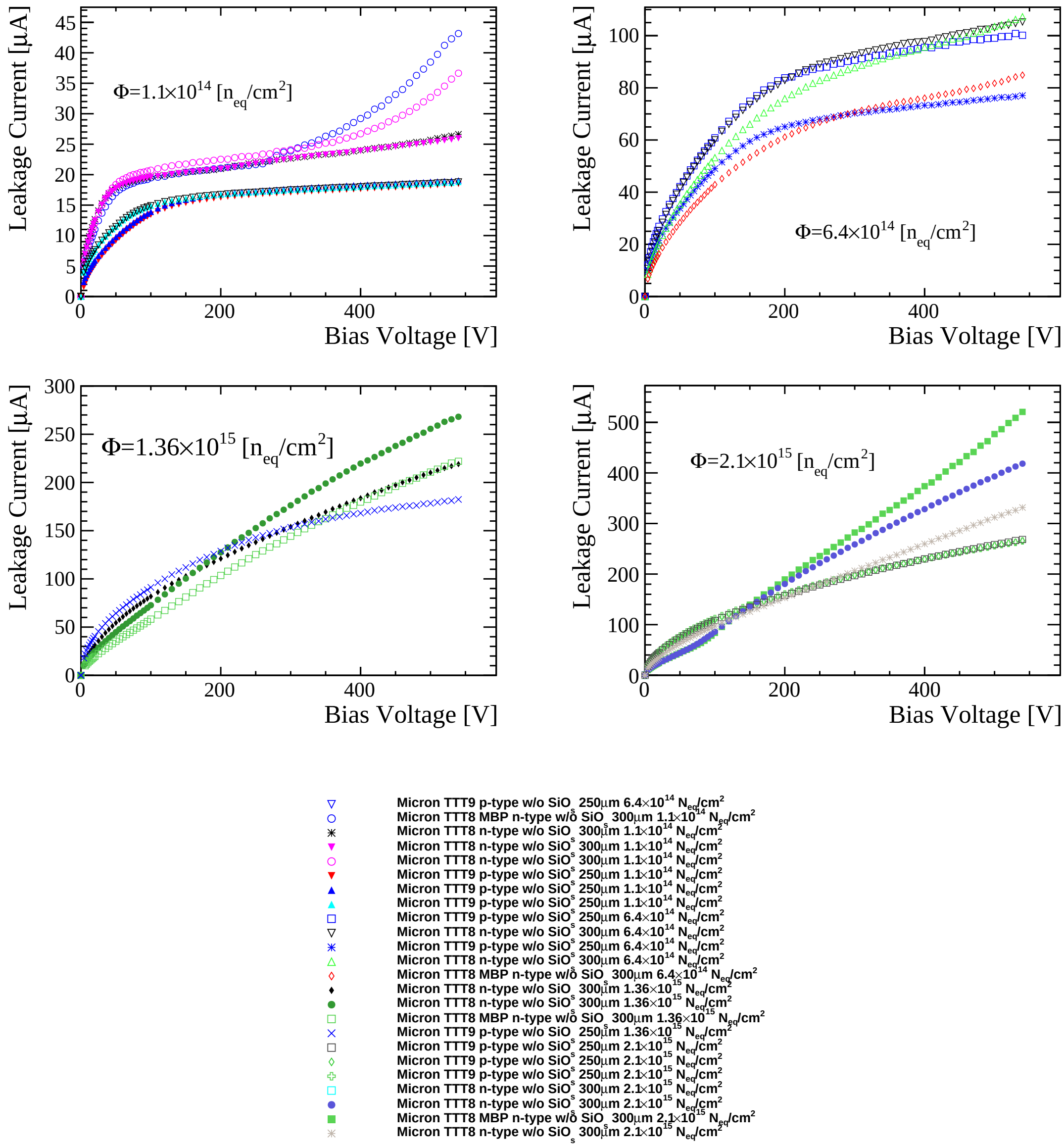

Figure 55: Leakage current of Micron mini-sensors after irradiation split into each fluence. Starting from top left to bottom right, the fluence shown (in 1 MeV neutron equivalent) is 1.1E14, 6.4E14, 1.36E15, and 2.1E14. Here the post-irradiation leakage current is measured at T=-5C and all irradiation levels, and sensor geometries and technologies are shown.

log(V) curve with two linear functions before and after the "kink" in the curve, and then computing their intercept. While at lower fluences this method is straight forward, at higher fluences this becomes slightly difficult because the "kink" in the distribution is not as apparent. A conservative uncertainty of ≈40V is estimated for these data points.

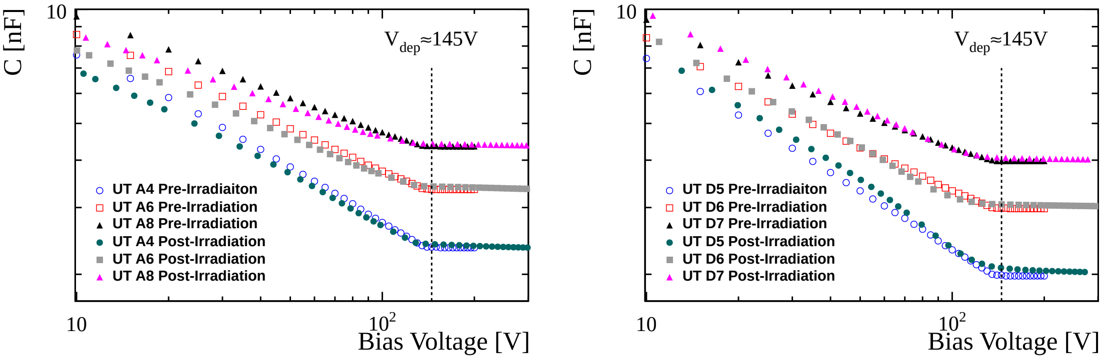

Figure 56: Capacitance versus voltage measurements of 1/2A (left) and full size D (right) Hamamatsu detectors. Pre-irradiation it is clear that around 145V the detectors reach full depletion, but post-irradiation curves don't show a clear indication when the detector is full depleted. This is expected since these detectors were irradiated non-uniformly and most of the detector is not irradiated at all. Note in the plot individual sensors are offset in Y from each other to make viewing easier.

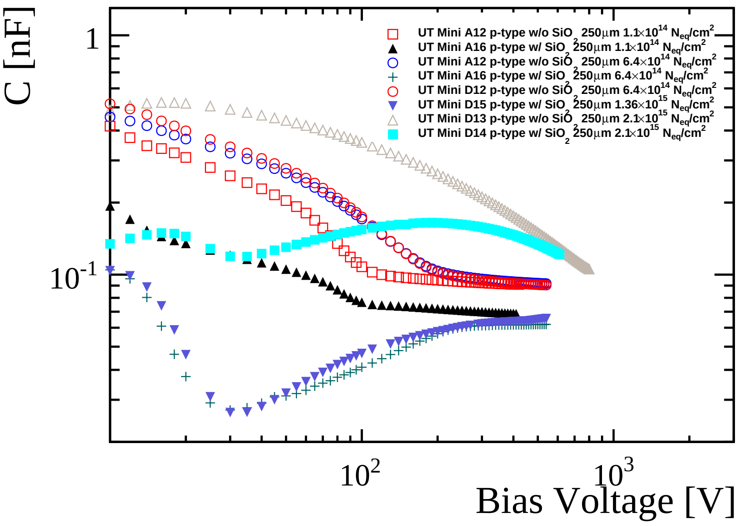

Figure 57: Capacitance versus voltage measurements of Hamamatsu mini-sensors.

The depletion voltage is not reached for sensors irradiated to the highest fluence and are therefore not shown here. For sensors with backside passivation, and thus show the "inverse" effect described above, it is assumed that when full depletion is reached the CV curve flattens out as in unpassivated detectors. Fits of log(C) versus log(V) curves can be viewed in Figures 60 and 61 for Micron and Hamamatsu mini-sensors, respectively. 1/2A and full size D detectors are not included here. A summary of all the depletion voltages

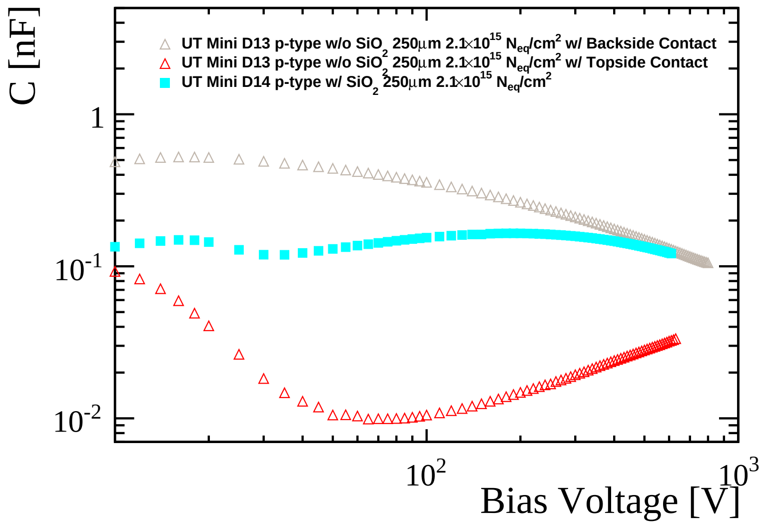

Figure 58: Capacitance versus voltage measurement on a Hamamatsu mini-sensor irradiated to 2E15 n_{eq}/cm^2. The gray data points show the CV dependence when biasing the detector through the backplane and the red data points shown when the same detector is biased via the topside contact. The Cyan data points show a detector with backside passivation biased via the topside contact for reference.

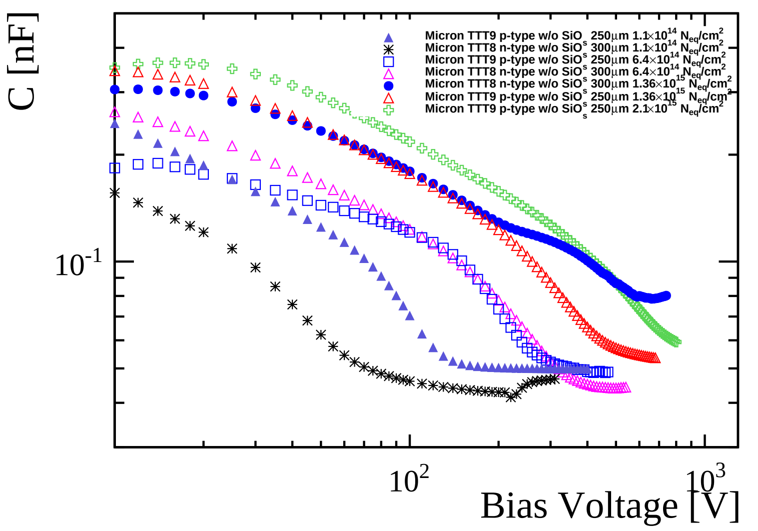

Figure 59: Capacitance versus voltage measurements of Micron mini-sensors.

782 as a function of fluence is shown in Figure 62 for all Hamamatsu and Micron mini-sensors.

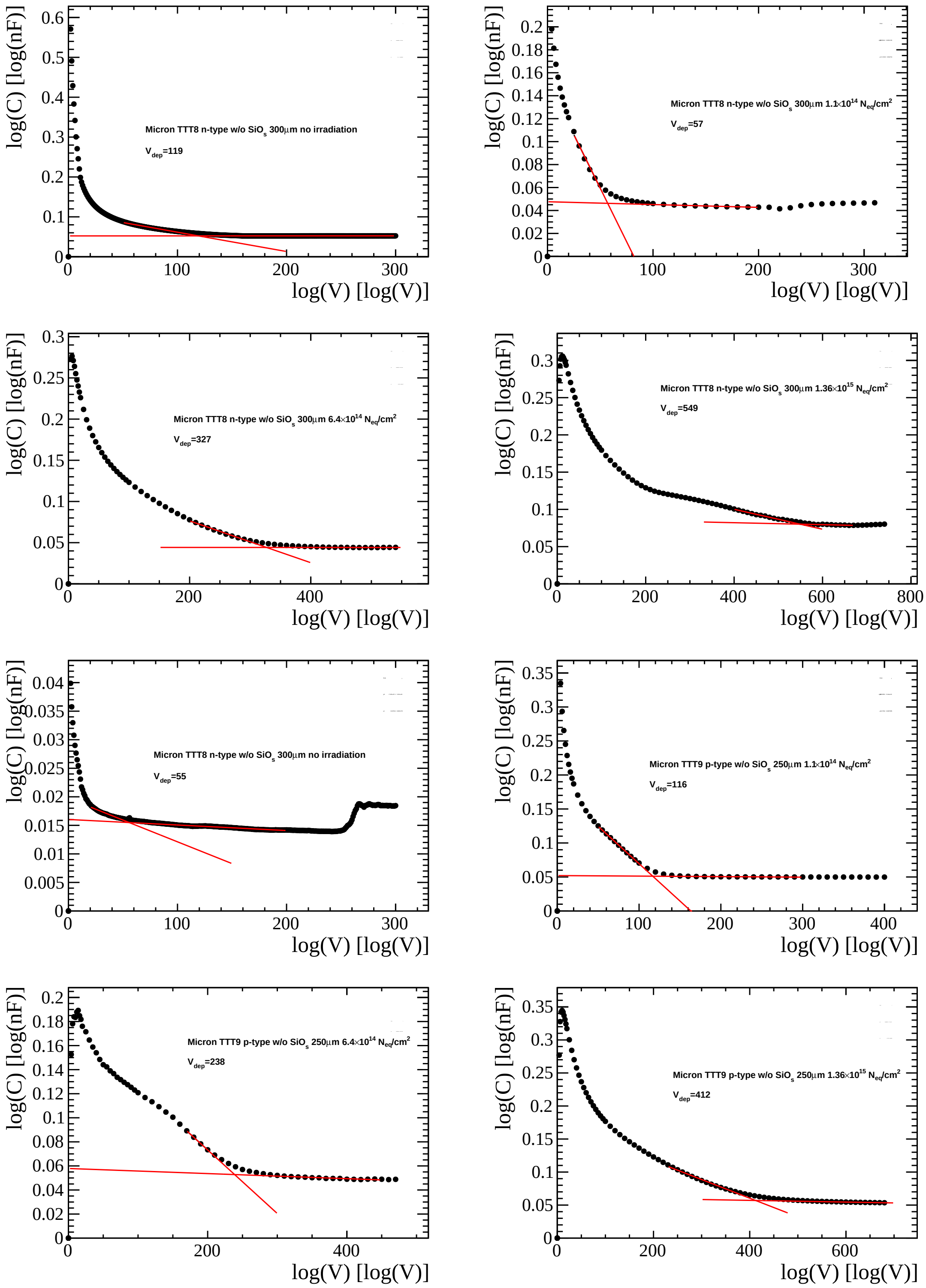

Figure 60: Capacitance versus voltage fits of Micron mini-sensor. The irradiation levels and types are given in each plot.

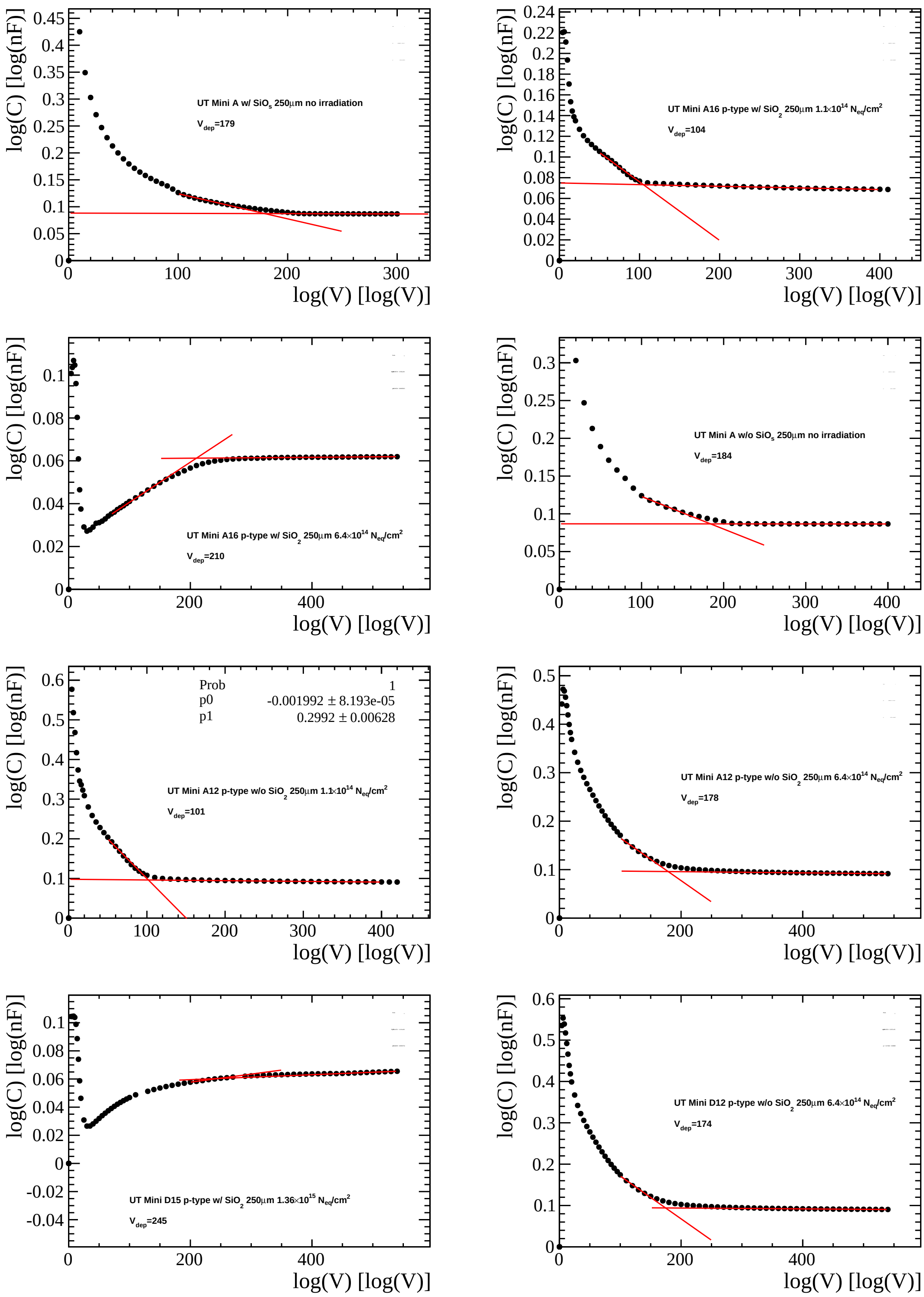

Figure 61: Capacitance versus voltage fits of Hamamatsu mini-sensors. The irradiation levels and types are given in each plot.

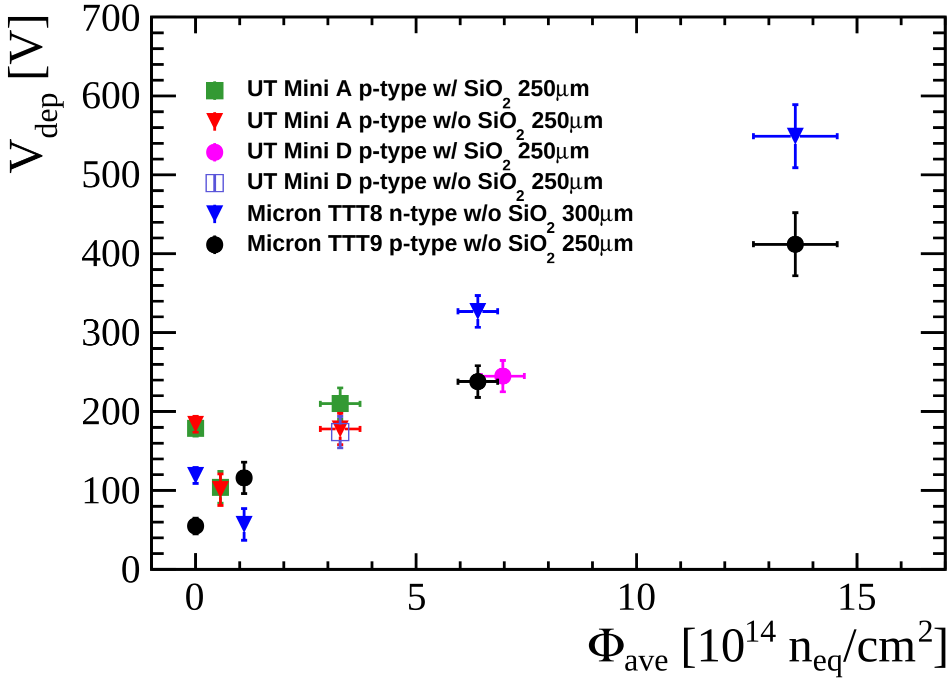

Figure 62: Summary of the depletion voltages as a function of fluence for all Hamamatsu and Micron mini-sensors

A.4 Effective bandgap

Measurements of $E_{g,eff}$ on a subset of Hamamatsu and Micron mini-sensors were carried out at the RD50 lab at CERN, after irradiation. A measurement on each type of sensor at each fluence would of been ideal but due to testbeam priorities, Hamamatsu mini-sensors at the first two fluences were already being tested in 2015 testbeams. To determine the bandgap, leakage current measurements were measured at two temperatures. Rearranging Equation 1, we get

$$E_{g,eff} = -2k_b \frac{T_1 T_2}{T_1 - T_2} \cdot ln(\frac{I_2 T_1^2}{I_1 T_2^2}), \tag{2}$$

where $I_{1,2}$ and $T_{1,2}$ are the leakage current and temperature (in Kelvin), respectively, at two different temperatures, and k_b is Boltzmann's constant. For this measurement T=-5C and -20C were used and correspond to I_1 and T_1, and I_2 and T_2, respectively.

Figure 63 shows the result of $E_{g,eff}$ as a function of bias voltage for all mini-sensors considered. For bulk generation current, $E_{g,eff}$ is expected to be independent of bias voltage. There are a few detectors in Figure 63 that seem not to constant over the bias scan. For low bias voltages ($< V_{dep}$) two explanations for the non-constant behavior of $E_{g,eff}$ can be due to other sources of current other than bulk current (e.g., surface current), which dominates after depletion, and the other being that the sensor temperature is not completely constant. Sensors cool exponentially and if they haven't sufficiently settled that would affect the measurement. Each data point along the bias scan was sufficiently delayed such that the temperature had enough time to settle after a few data points were taken. For the following analysis only data points above 100V are considered. There are three other curves that show non-uniformity over a large portion of the bias scan. One Micron sensor, irradiated to the highest fluence, which shows large changes at voltages larger that 400. This is due to the sensor going into soft breakdown above 400C and for this particular sensor only data points between 100 and 400V are considered. The the other two Hamamatsu detectors, one possible explanation is self-heating of the sensors, but seems unlikely since they level off at higher bias voltages. Given that these detectors are highly irradiated and below depletion for most or all of the scan, and are biased via the topside contact, it is possible there are other sources of current. For these points only voltages above 200V are considered. In the collective determination of $E_{g,eff}$ these two Hamamatsu detectors are not considered as any unknown sources of current due to topside contact will bias the result, but are shown anyway for reference.

To determine $E_{g,eff}$ for each sensor, bias scan data points were projected onto $E_{g,eff}$ and the resulting histogram was fit with a Gaussian probability distribution function. The mean and sigma of the fit was then taken to be the central value and uncertainty for each sensor. The resulting fits can be seen in Figure 64. Finally, the measured value for $E_{g,eff}$ as a function of fluence for each sensor considered is shown in Figure 65. Also shown in green in Figure 65 is a combined fit to the data where the error represents the uncertainty in the fit. Combining both TTT8, TTT9, and mini-D sensors without backside passivation, we measure $E_{g,eff} = 1.180 \pm 0.002 \pm 0.003$ eV where the first error is the uncertainty on the fit and the second is determined by changing the binning on individual sensor fits and seeing how far the central value shifts in the overall determination of $E_{g,eff}$. Figure 66 shows separate determination of $E_{g,eff}$ for TTT8 and TTT9 sensors. From these separate fits, and the one value of $E_{g,eff}$ for the Hamamatsu detector without backside passivation, there is no significant deviation of the individual sensor designs from the combined value. There is also no significant deviation of $E_{g,eff}$ from the central value for sensors irradiated up to a fluence of 2.1×10^{15} $\mathrm{n_{eq}/cm^2}$

A.5 $\Delta I/V$ versus Φ

The measurement $\Delta I/V$ versus Φ presented here is not only useful in studying static irradiation effects in silicon sensors but also acting as a confirmation that sensors tested in testbeams have received the expected dose. It is expected that sensors obey the linear relationship

$$\frac{I_{post} - I_{pre}}{V} = \frac{\Delta I}{V} = \alpha\Phi, \tag{3}$$

where $I_{post,pre}$ are the post and pre-irradiation leakage currents, respectively, Φ is the fluence, and α is the slope parameter. Sensor not falling on the curve should indicate that its integrated dose is not properly known.

To determine ΔI of each sensor, a leakage current data point slightly above depletion

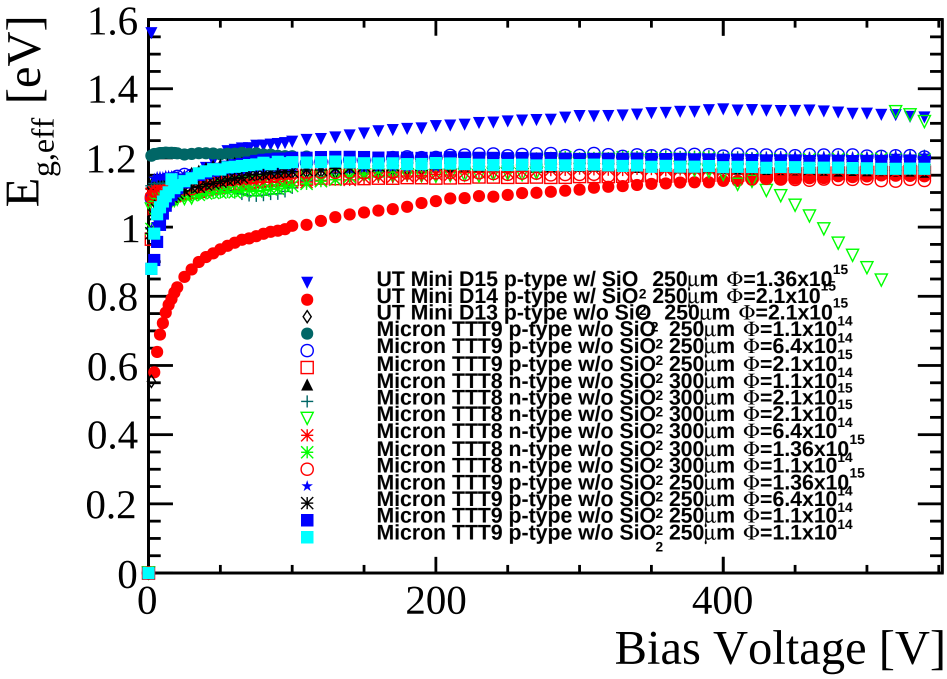

Figure 63: Summary of the $E_{g,eff}$ measurement as a function of voltage for all mini-sensors considered.

was chosen. Additionally, to compare to previous measurements, sensors were scaled to 21C using equation 1 where the value $E_{g,eff} = 1.180$ [eV], determined in the previous section, is used. Pre-irradiation current is considered negligible and set to zero as it is many orders of magnitude lower. For sensors irradiated to the highest dose the largest bias voltage data point was taken as they do not deplete within our given bias scans. There are a few other caveats to consider. Firstly for the larger area sensors, the dose is non-uniform, and thus the fluence was integrated over the entire detector, giving it a small average fluence. Secondly, several sensors have beampipe cutouts. These have to be taken into account carefully with calculated the volume of the detector and the integrated fluence. Figure 67 shows the results of $\Delta I/V$ versus Φ for all detectors.

From the fit to the data, we measure a value of $\alpha = 7.1 \pm 0.1$ [A/cm], which is expected for sensors with short term annealing [13].

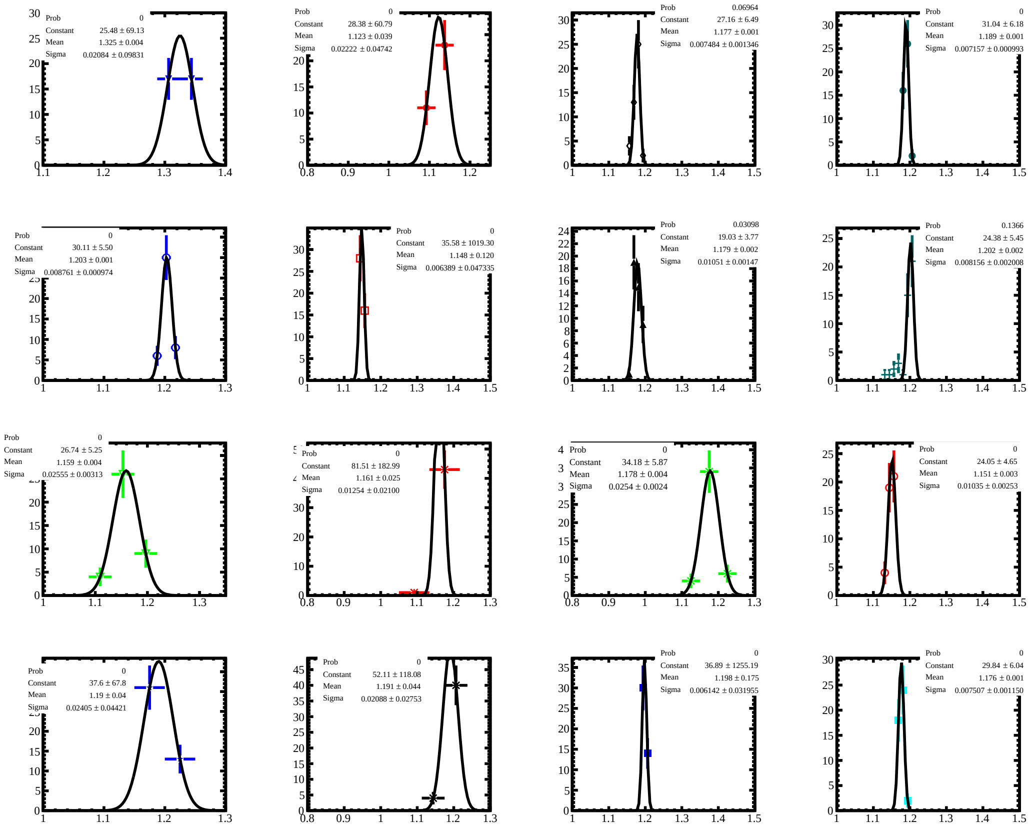

Figure 64: Fits of $E_{g,eff}$ for all mini-sensors considered. Note each histogram has the same data points given in the legend shown in Figure 63.

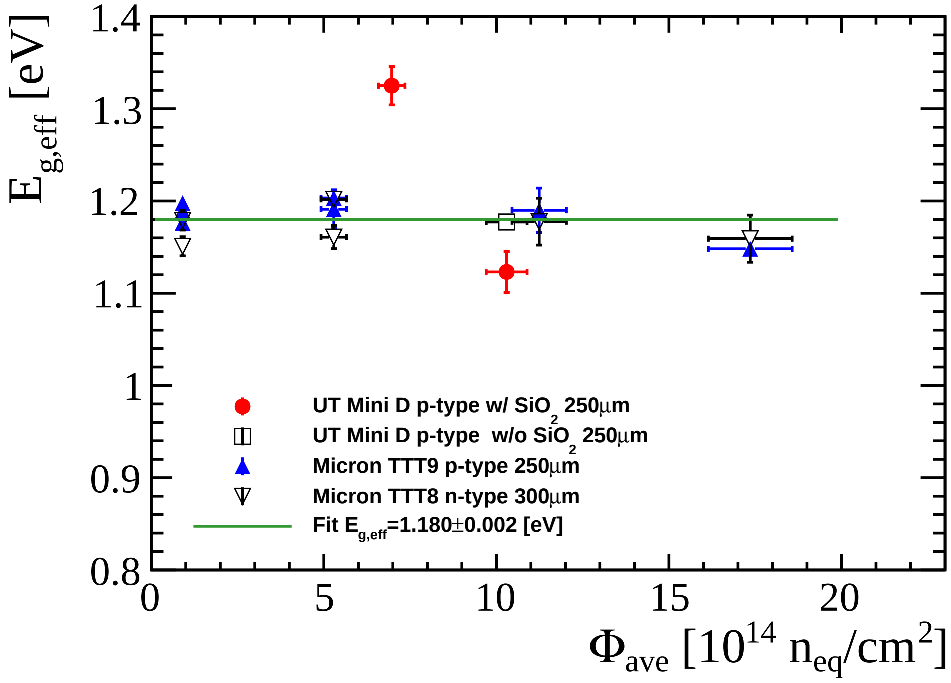

Figure 65: $E_{g,eff}$ as a function of fluence for all mini-sensors considered. A combined fit to the data is shown as the green line where the error represents the uncertainty of the fit.

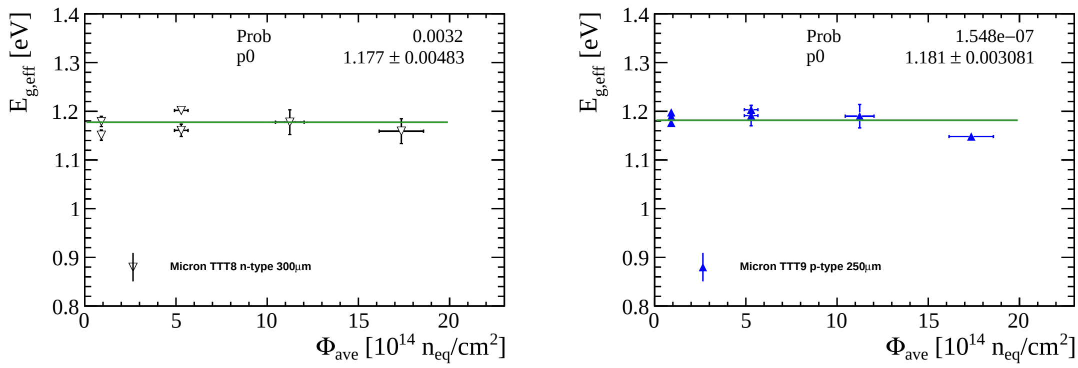

Figure 66: Measured values of $E_{g,eff}$ vs. fluence for TTT8 (left) and TTT9 (right) mini-sensors. Fits to the data is shown as the green line where the error represents the uncertainty of the fit.

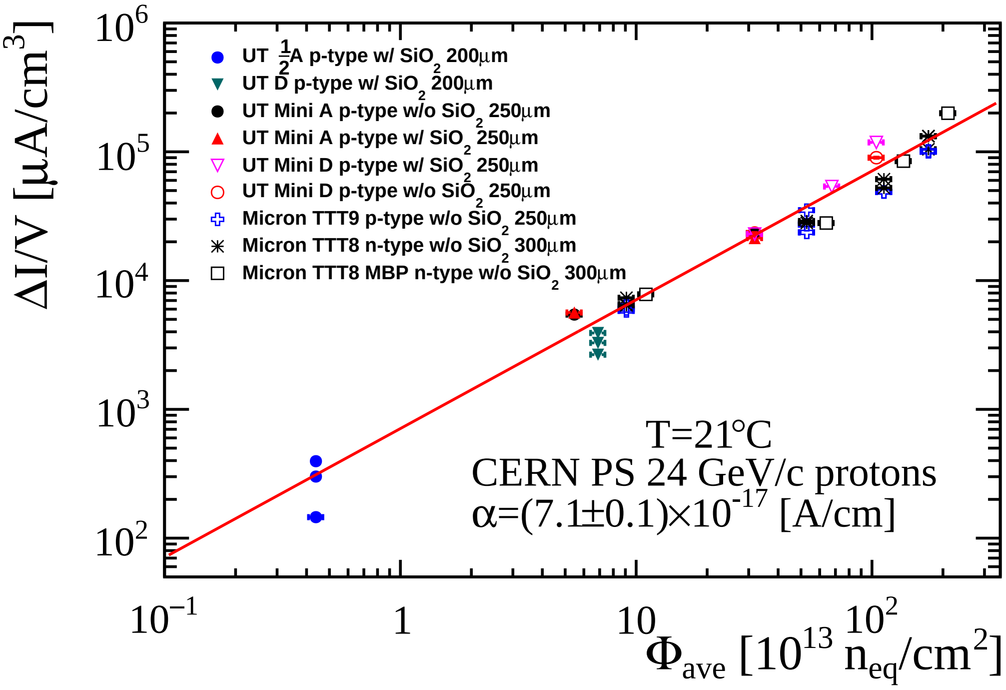

Figure 67: $\Delta I/V$ versus Φ for all Hamamatsu and Micron sensors. The red line shows a fit to all data.

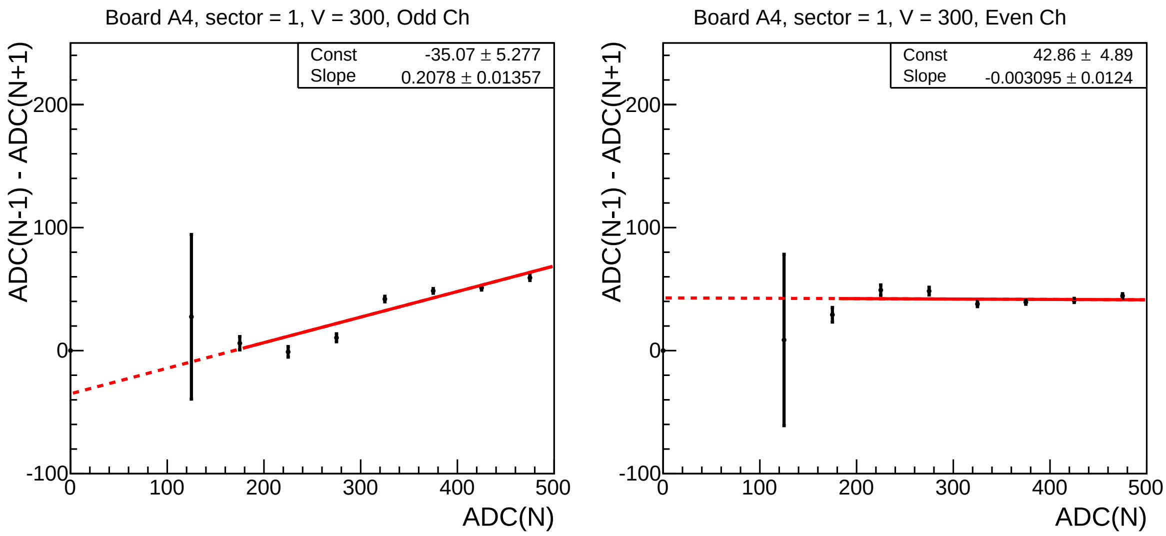

Figure 68: Graphs of $ADC(N-1) - ADC(N+1)$ versus $ADC(N)$, for (left) odd numbered Beetle channels and (right) even numbered Beetle channels, for Board A4, sector 1. A linear fit to each is overlaid.

B Cross talk plots

In this section, we show the graphs of t $ADC(N-1) - ADC(N+1)$ versus $ADC(N)$ for each board/sector. In some cases, the points have very large error bars. This signifies the χ^2/dof of the Gaussian fit was larger than 2.5, and the error was (arbitrarily) multiplied by 100 so not to pull the linear fit.

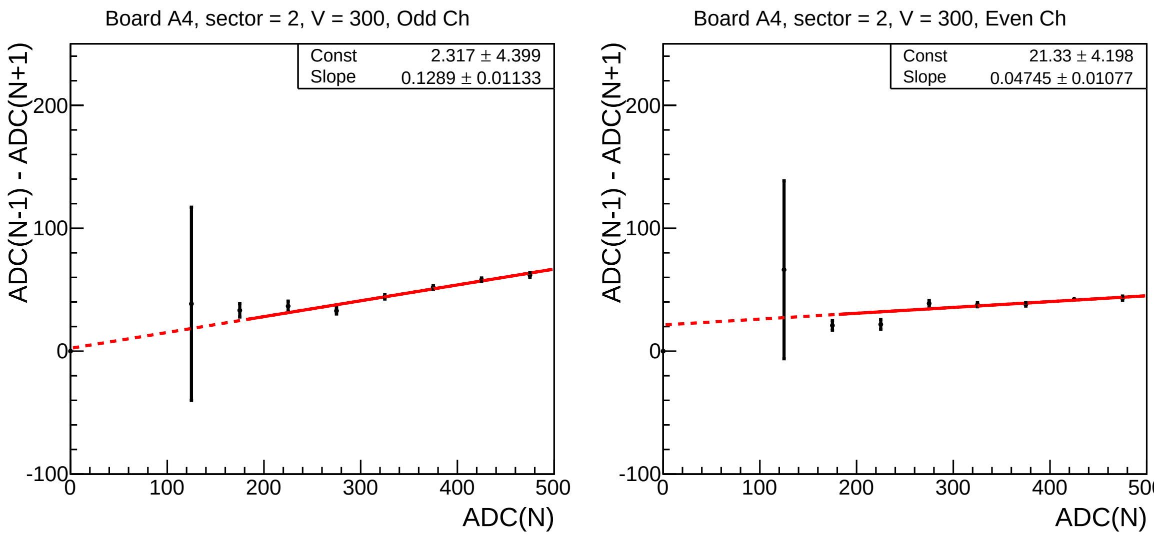

Figure 69: Graphs of $ADC(N-1) - ADC(N+1)$ versus $ADC(N)$, for (left) odd numbered Beetle channels and (right) even numbered Beetle channels, for Board A4, sector 2. A linear fit to each is overlaid.

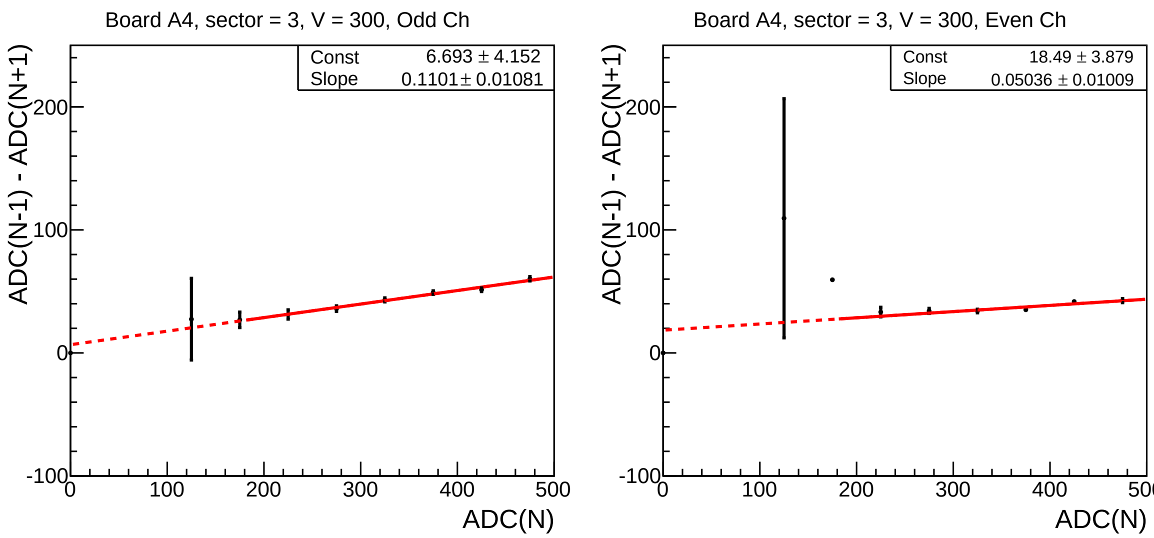

Figure 70: Graphs of $ADC(N-1) - ADC(N+1)$ versus $ADC(N)$, for (left) odd numbered Beetle channels and (right) even numbered Beetle channels, for Board A4, sector 3. A linear fit to each is overlaid.

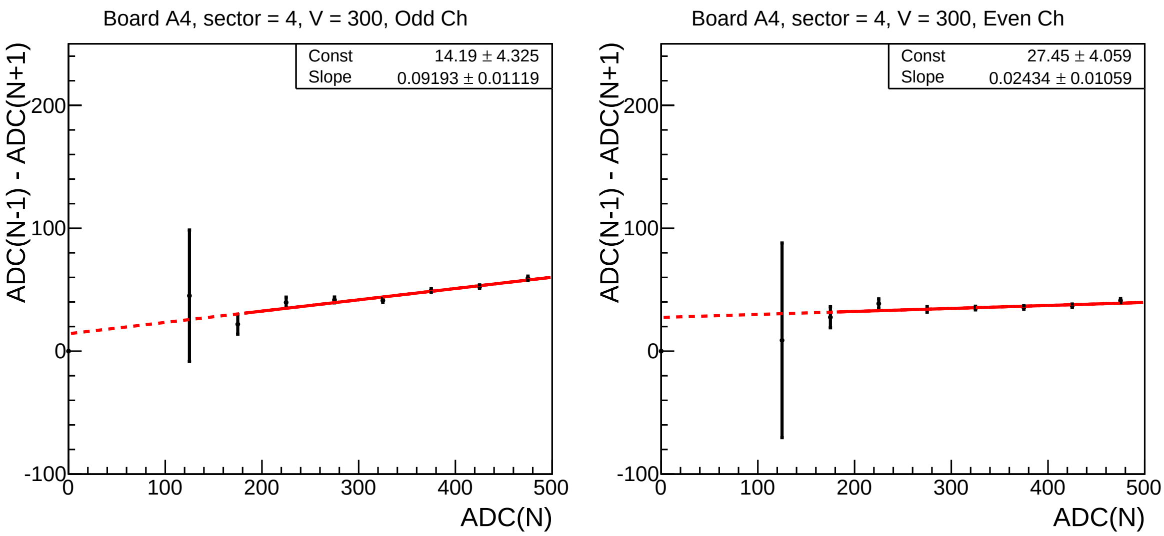

Figure 71: Graphs of $ADC(N-1) - ADC(N+1)$ versus $ADC(N)$, for (left) odd numbered Beetle channels and (right) even numbered Beetle channels, for Board A4, sector 4. A linear fit to each is overlaid.

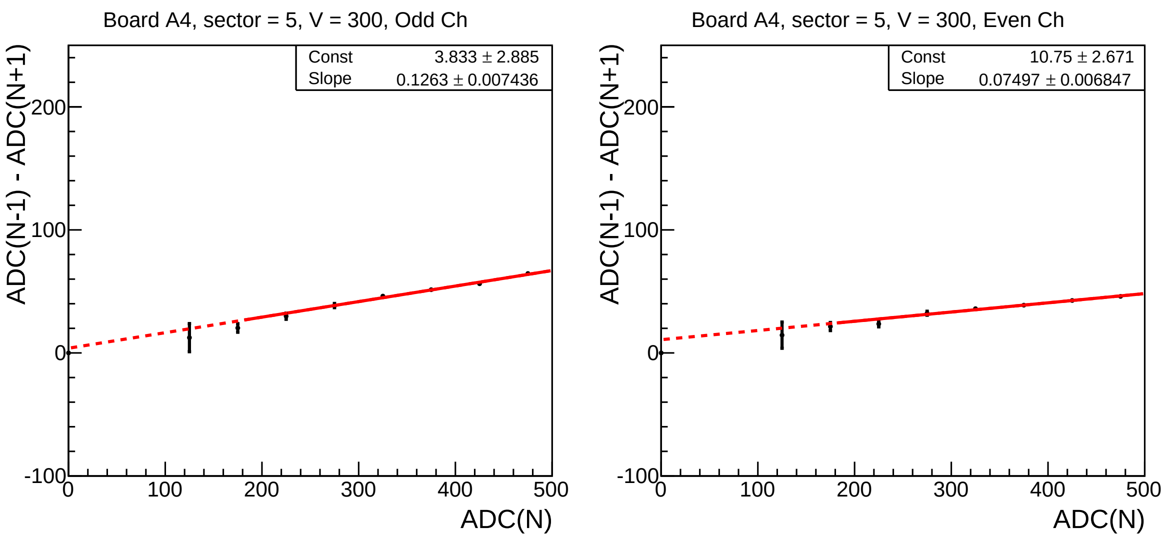

Figure 72: Graphs of $ADC(N-1) - ADC(N+1)$ versus $ADC(N)$, for (left) odd numbered Beetle channels and (right) even numbered Beetle channels, for Board A4, sector 5. A linear fit to each is overlaid.

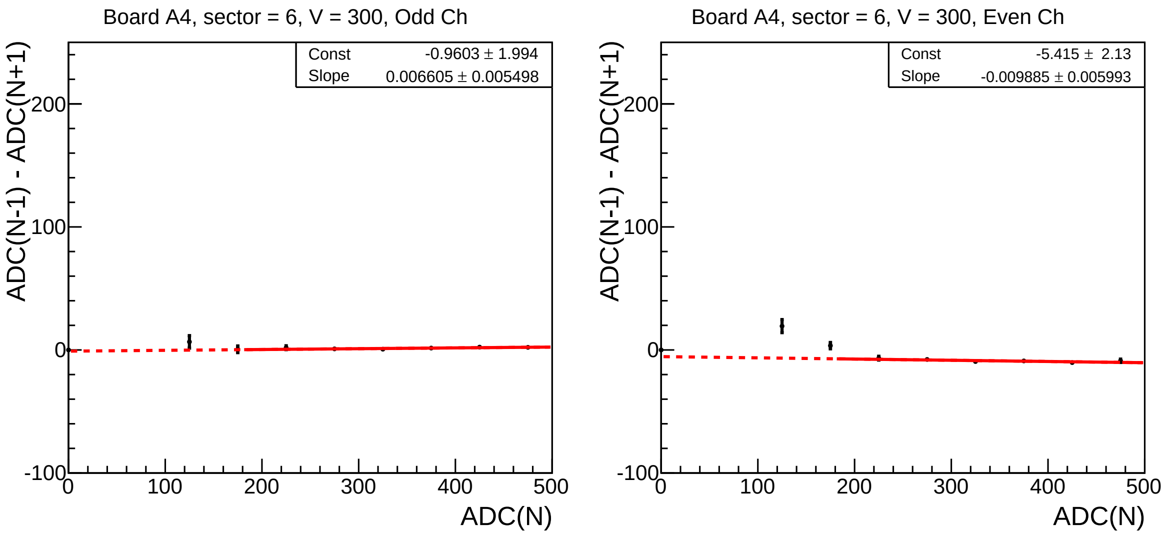

Figure 73: Graphs of $ADC(N-1) - ADC(N+1)$ versus $ADC(N)$, for (left) odd numbered Beetle channels and (right) even numbered Beetle channels, for Board A4, sector 6. A linear fit to each is overlaid.

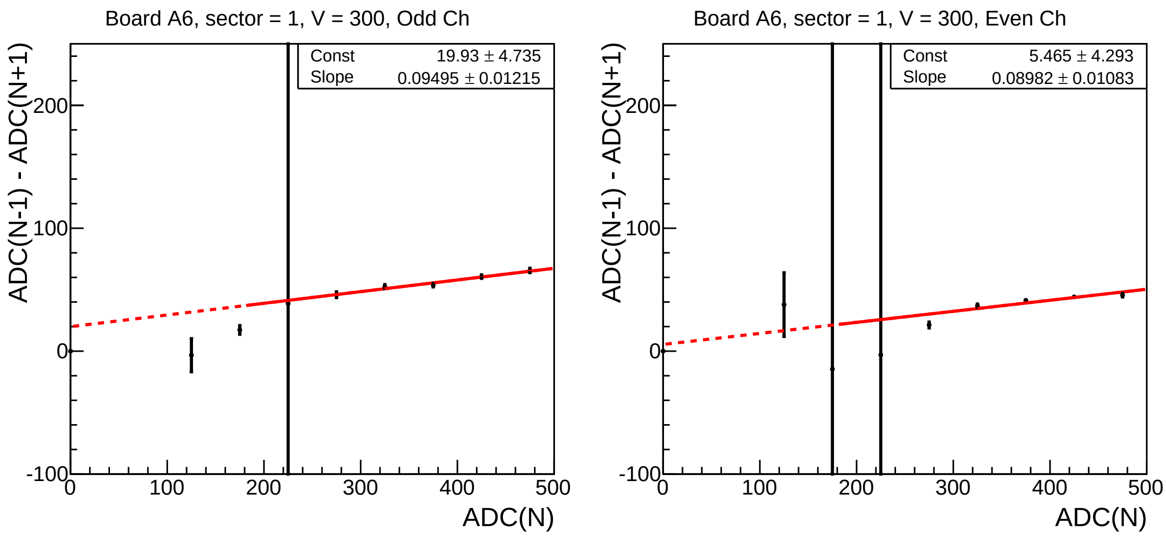

Figure 74: Graphs of $ADC(N-1) - ADC(N+1)$ versus $ADC(N)$, for (left) odd numbered Beetle channels and (right) even numbered Beetle channels, for Board A6, sector 1. A linear fit to each is overlaid.

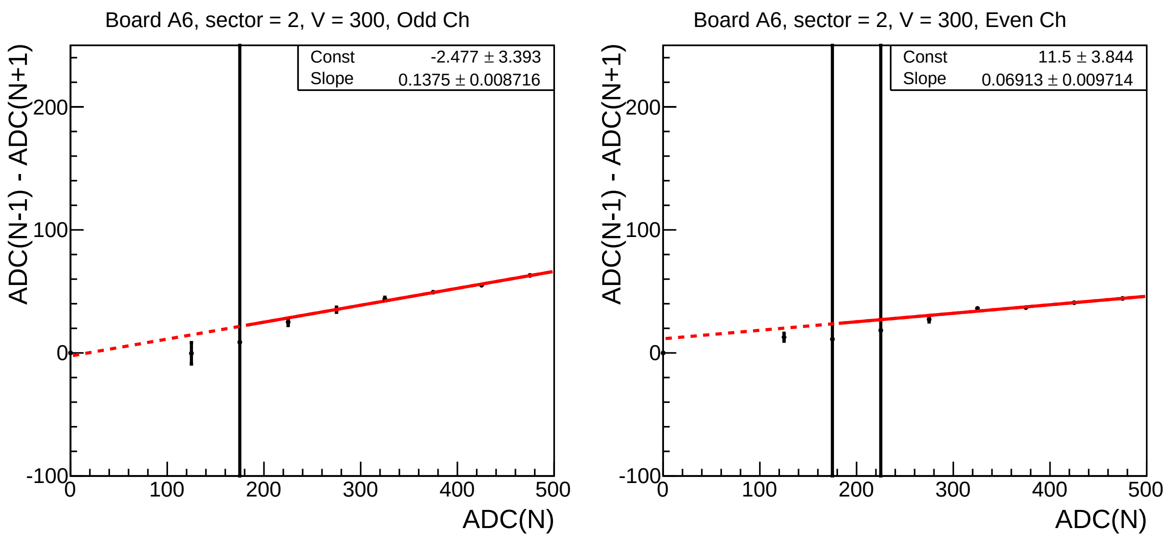

Figure 75: Graphs of $ADC(N-1) - ADC(N+1)$ versus $ADC(N)$, for (left) odd numbered Beetle channels and (right) even numbered Beetle channels, for Board A6, sector 2. A linear fit to each is overlaid.

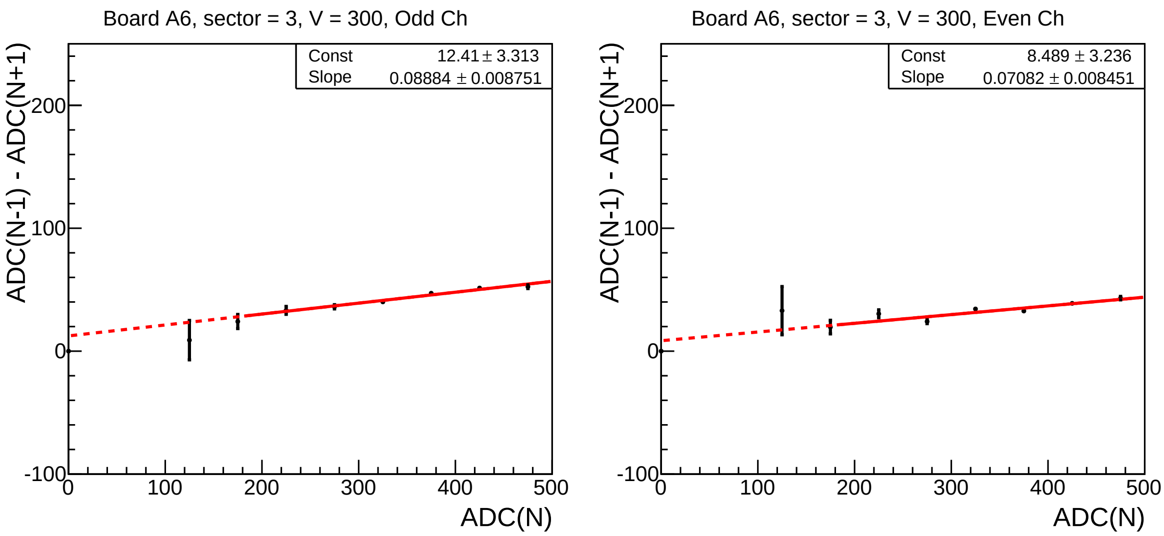

Figure 76: Graphs of $ADC(N-1) - ADC(N+1)$ versus $ADC(N)$, for (left) odd numbered Beetle channels and (right) even numbered Beetle channels, for Board A6, sector 3. A linear fit to each is overlaid.

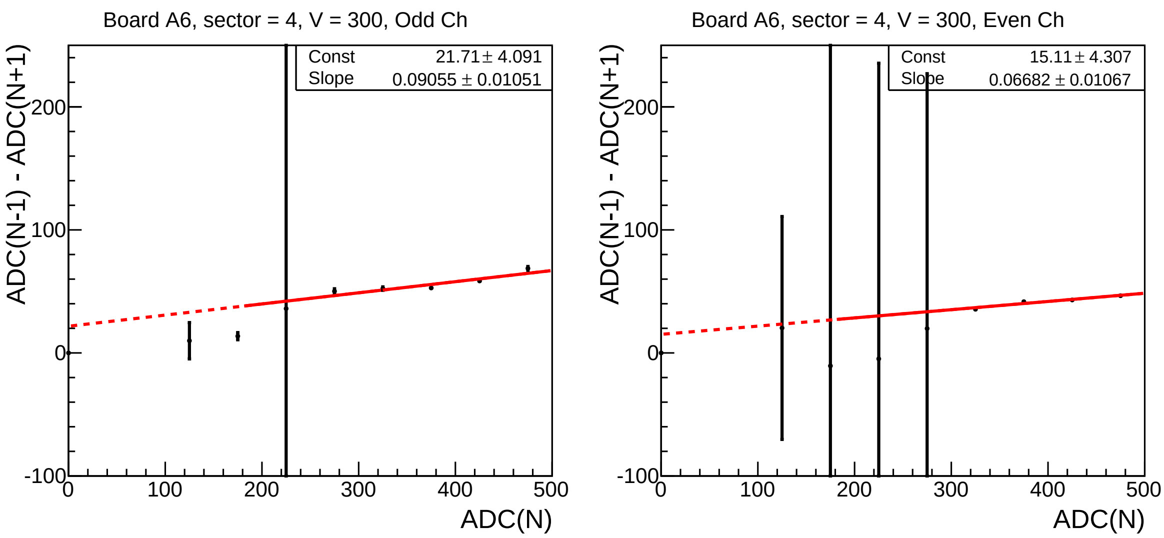

Figure 77: Graphs of $ADC(N-1) - ADC(N+1)$ versus $ADC(N)$, for (left) odd numbered Beetle channels and (right) even numbered Beetle channels, for Board A6, sector 4. A linear fit to each is overlaid.

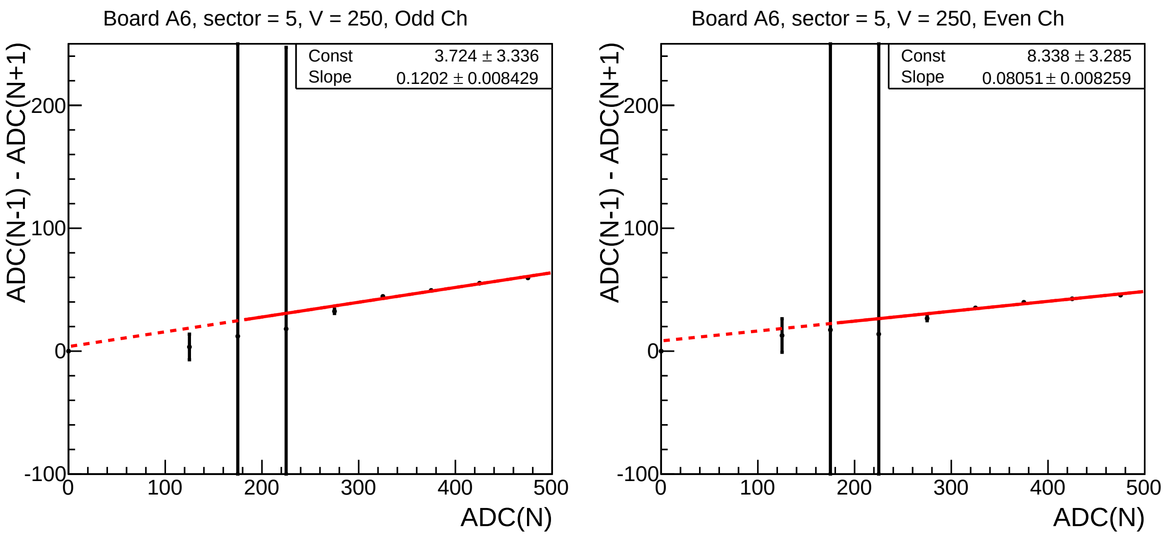

Figure 78: Graphs of $ADC(N-1) - ADC(N+1)$ versus $ADC(N)$, for (left) odd numbered Beetle channels and (right) even numbered Beetle channels, for Board A6, sector 5. A linear fit to each is overlaid.

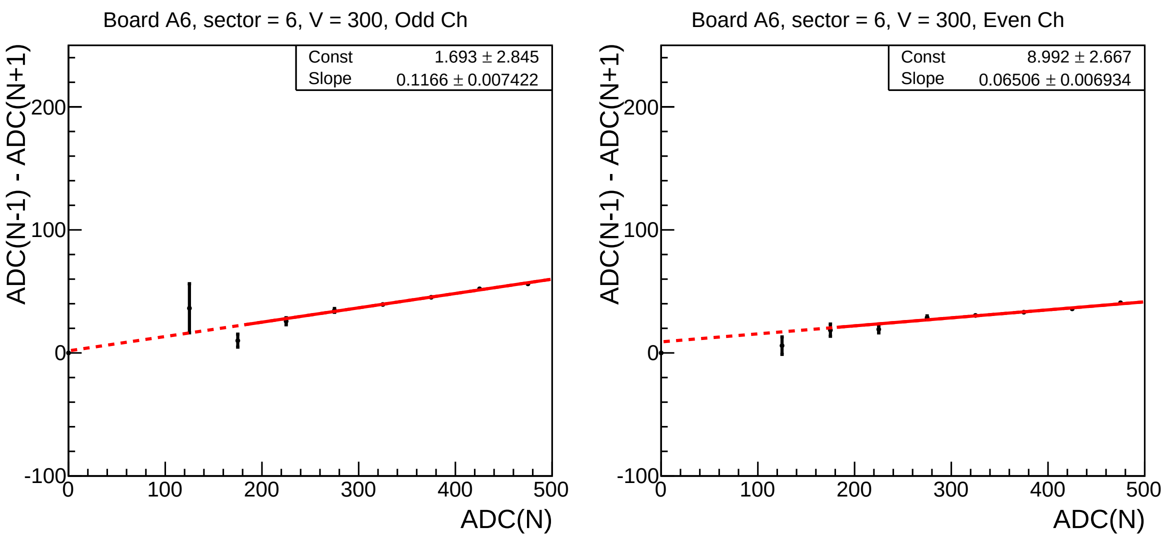

Figure 79: Graphs of $ADC(N-1) - ADC(N+1)$ versus $ADC(N)$, for (left) odd numbered Beetle channels and (right) even numbered Beetle channels, for Board A6, sector 6. A linear fit to each is overlaid.

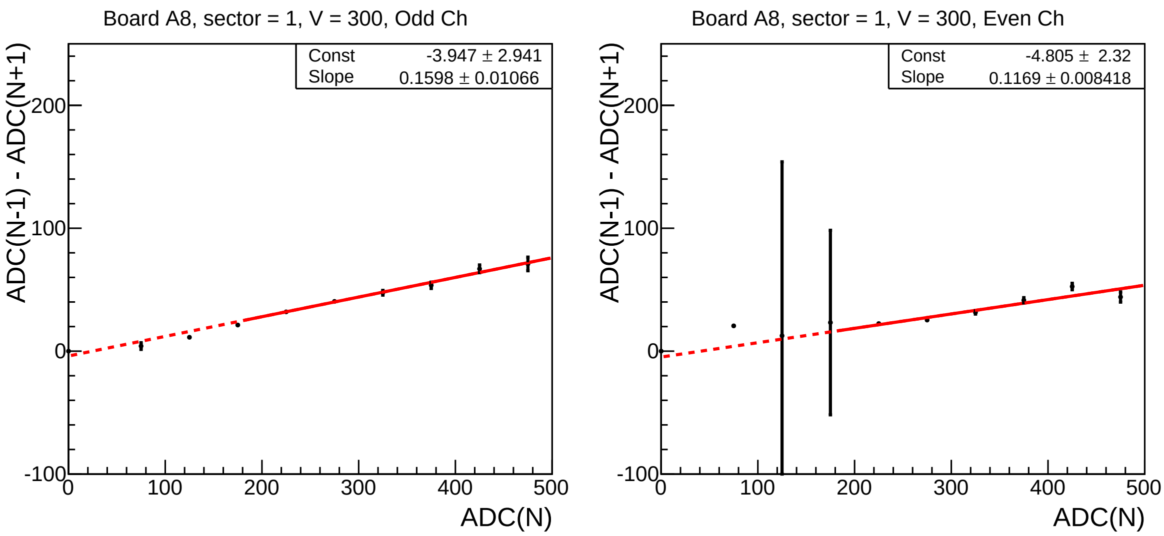

Figure 80: Graphs of $ADC(N-1) - ADC(N+1)$ versus $ADC(N)$, for (left) odd numbered Beetle channels and (right) even numbered Beetle channels, for Board A8, sector 1. A linear fit to each is overlaid.

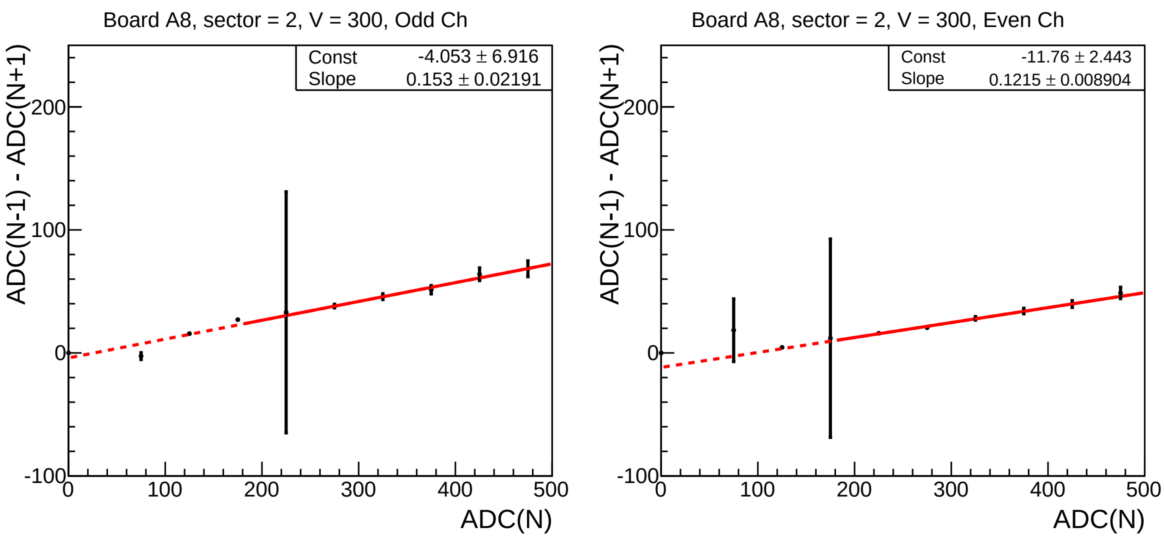

Figure 81: Graphs of $ADC(N-1) - ADC(N+1)$ versus $ADC(N)$, for (left) odd numbered Beetle channels and (right) even numbered Beetle channels, for Board A8, sector 2. A linear fit to each is overlaid.

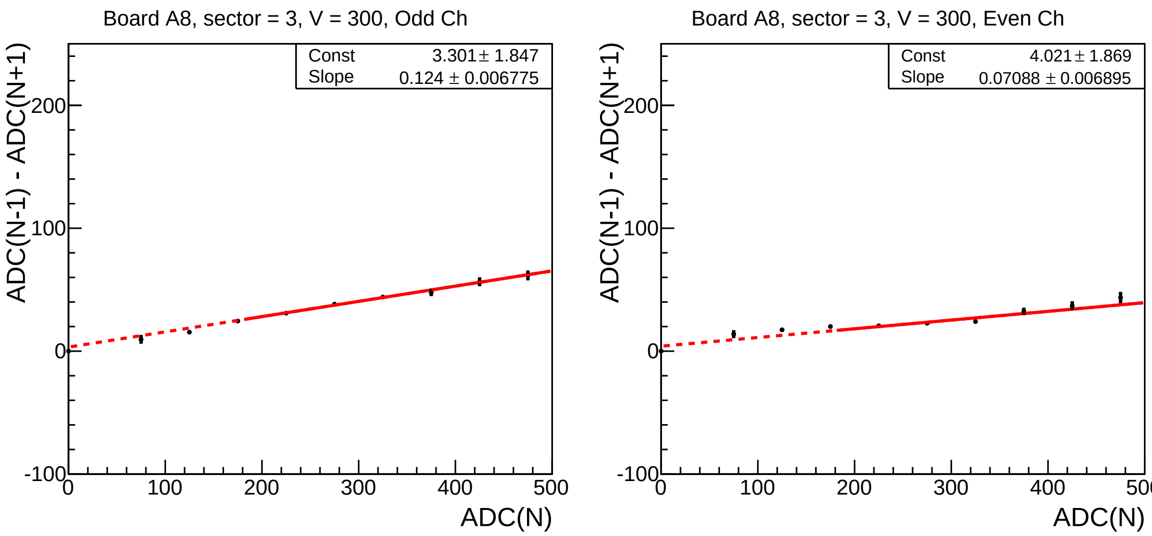

Figure 82: Graphs of $ADC(N-1) - ADC(N+1)$ versus $ADC(N)$, for (left) odd numbered Beetle channels and (right) even numbered Beetle channels, for Board A8, sector 3. A linear fit to each is overlaid.

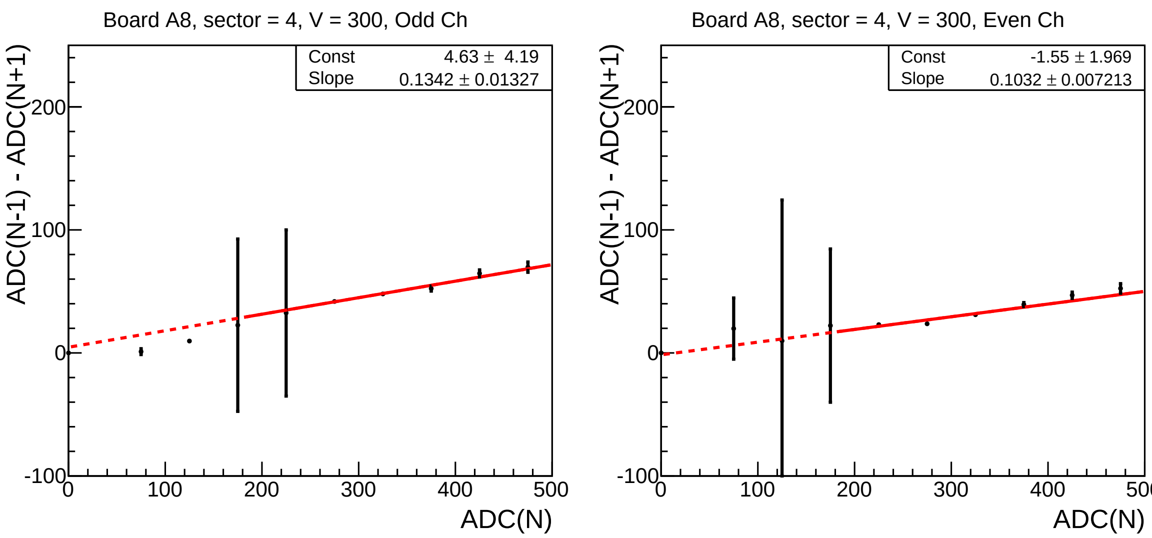

Figure 83: Graphs of $ADC(N-1) - ADC(N+1)$ versus $ADC(N)$, for (left) odd numbered Beetle channels and (right) even numbered Beetle channels, for Board A8, sector 4. A linear fit to each is overlaid.

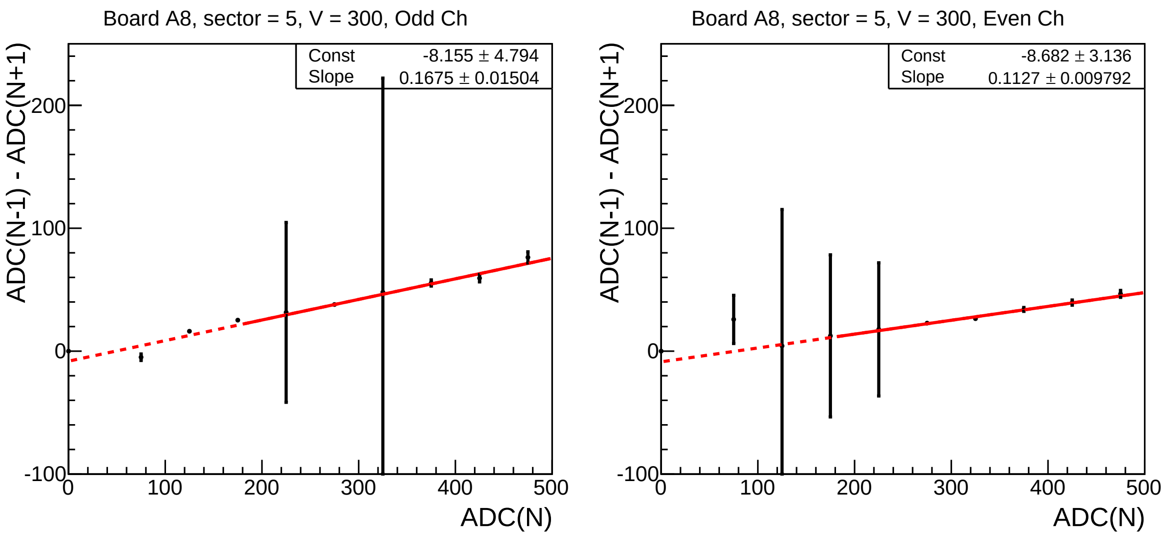

Figure 84: Graphs of $ADC(N-1) - ADC(N+1)$ versus $ADC(N)$, for (left) odd numbered Beetle channels and (right) even numbered Beetle channels, for Board A8, sector 5. A linear fit to each is overlaid.

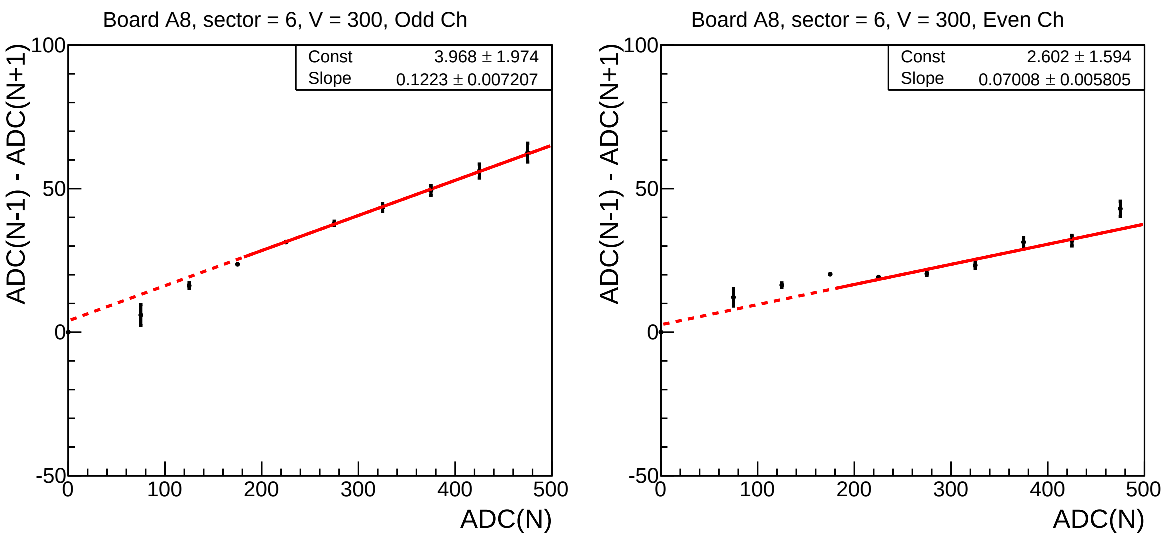

Figure 85: Graphs of $ADC(N-1) - ADC(N+1)$ versus $ADC(N)$, for (left) odd numbered Beetle channels and (right) even numbered Beetle channels, for Board A8, sector 6. A linear fit to each is overlaid.

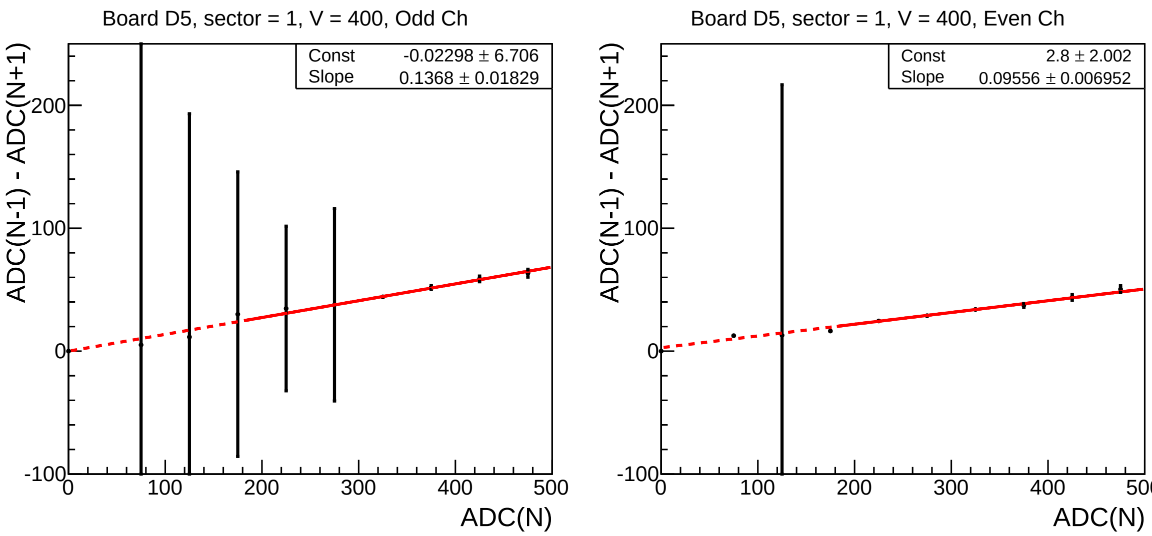

Figure 86: Graphs of $ADC(N-1) - ADC(N+1)$ versus $ADC(N)$, for (left) odd numbered Beetle channels and (right) even numbered Beetle channels, for Board D5, sector 1. A linear fit to each is overlaid.

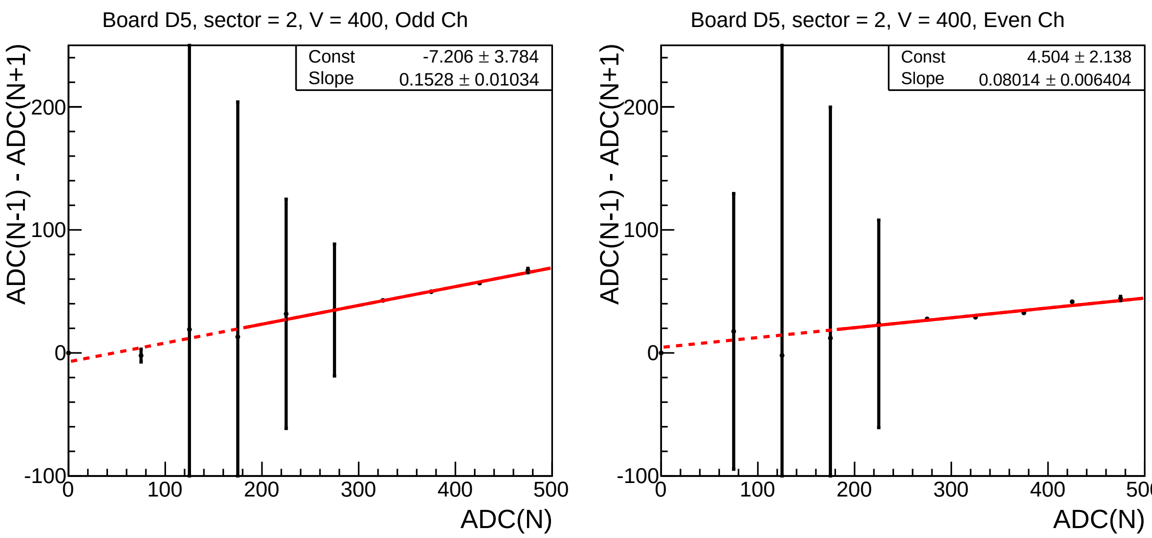

Figure 87: Graphs of $ADC(N-1) - ADC(N+1)$ versus $ADC(N)$, for (left) odd numbered Beetle channels and (right) even numbered Beetle channels, for Board D5, sector 2. A linear fit to each is overlaid.

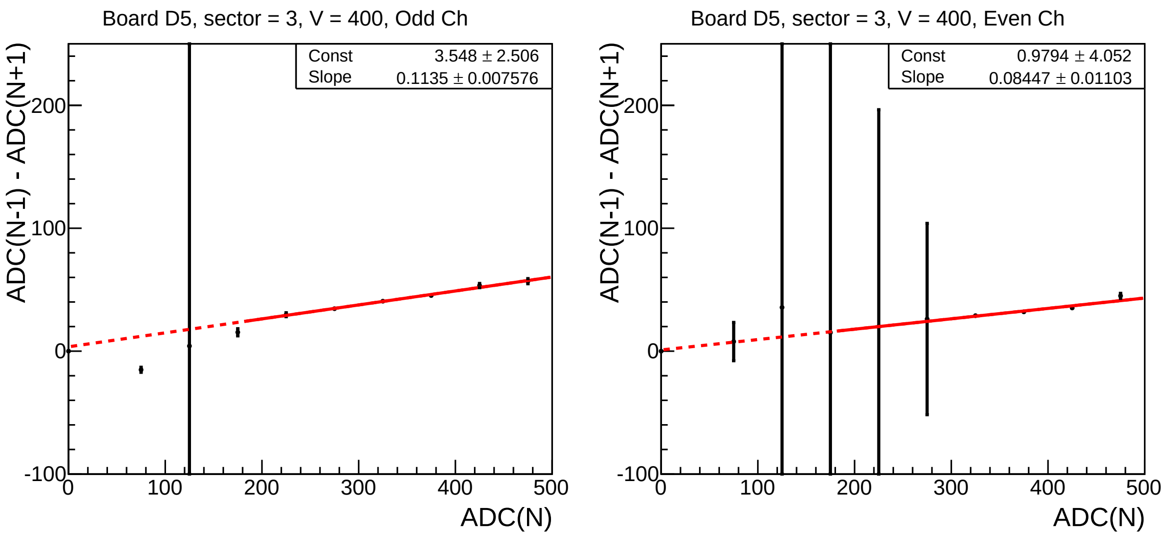

Figure 88: Graphs of $ADC(N-1) - ADC(N+1)$ versus $ADC(N)$, for (left) odd numbered Beetle channels and (right) even numbered Beetle channels, for Board D5, sector 3. A linear fit to each is overlaid.

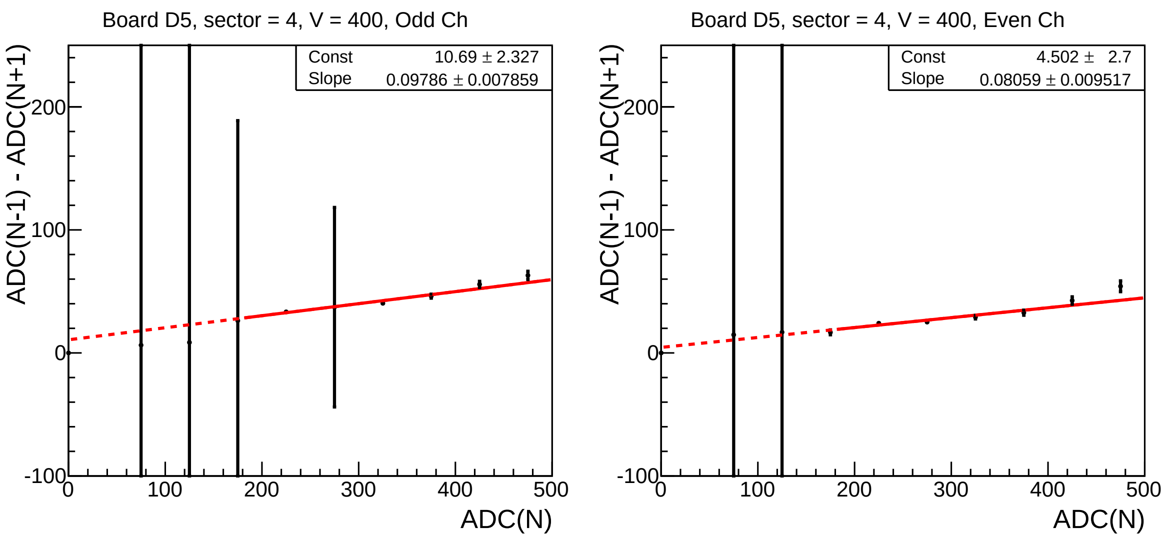

Figure 89: Graphs of $ADC(N-1) - ADC(N+1)$ versus $ADC(N)$, for (left) odd numbered Beetle channels and (right) even numbered Beetle channels, for Board D5, sector 4. A linear fit to each is overlaid.

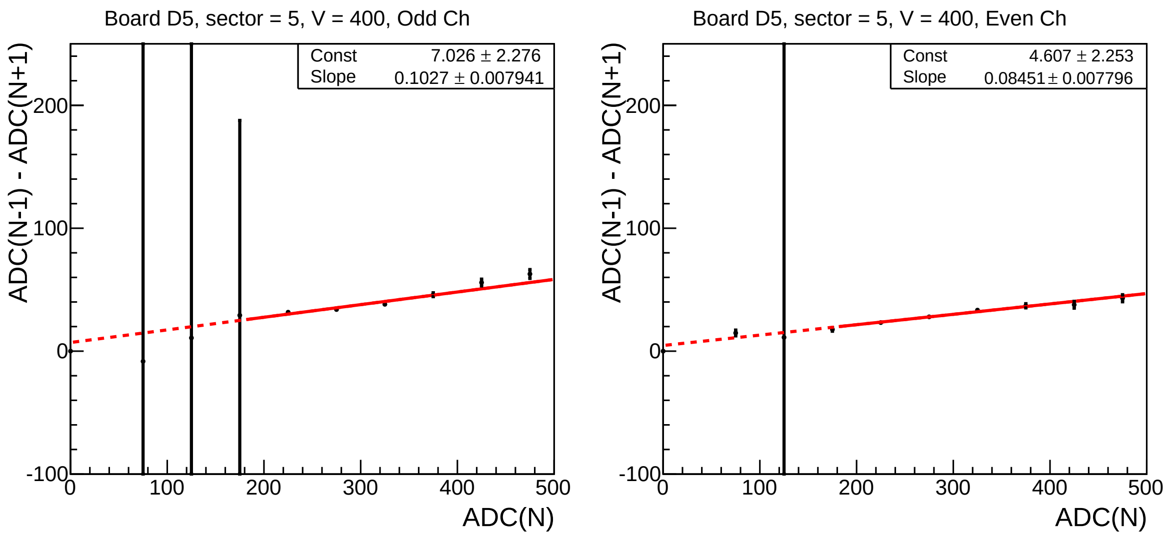

Figure 90: Graphs of $ADC(N-1) - ADC(N+1)$ versus $ADC(N)$, for (left) odd numbered Beetle channels and (right) even numbered Beetle channels, for Board D5, sector 5. A linear fit to each is overlaid.

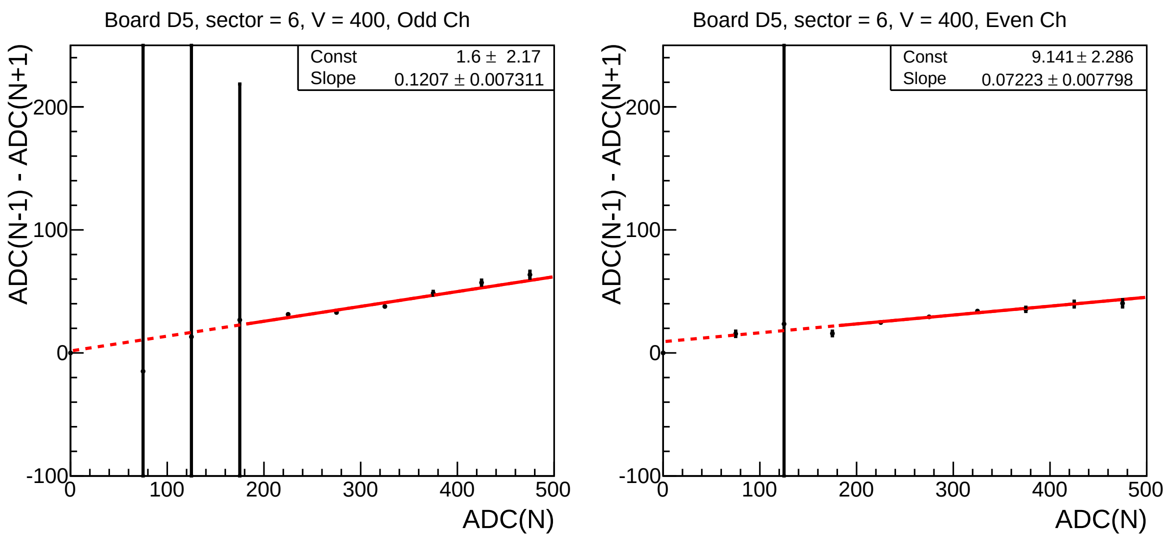

Figure 91: Graphs of $ADC(N-1) - ADC(N+1)$ versus $ADC(N)$, for (left) odd numbered Beetle channels and (right) even numbered Beetle channels, for Board D5, sector 6. A linear fit to each is overlaid.

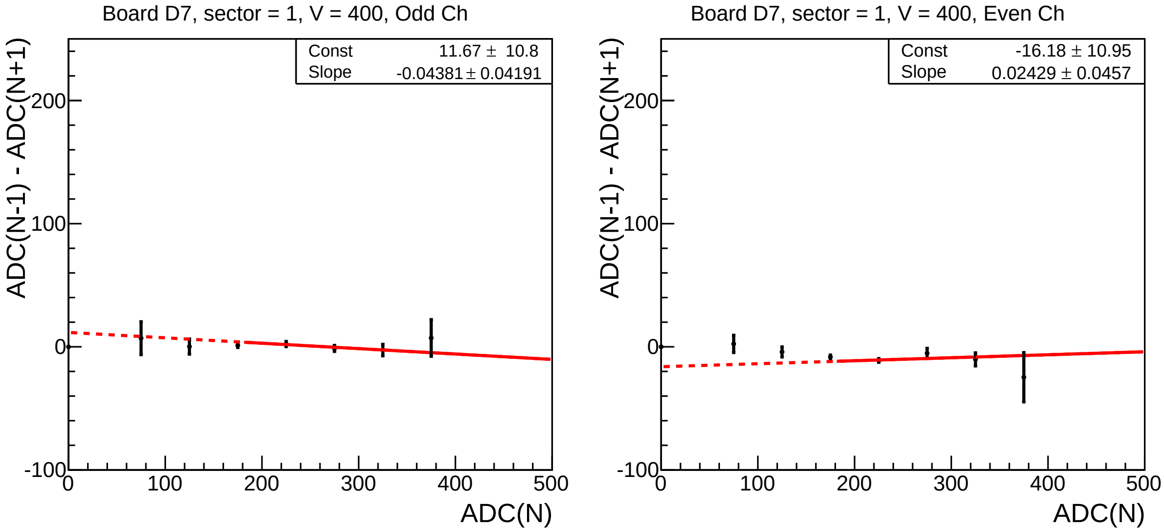

Figure 92: Graphs of $ADC(N-1) - ADC(N+1)$ versus $ADC(N)$, for (left) odd numbered Beetle channels and (right) even numbered Beetle channels, for Board D7, sector 1. A linear fit to each is overlaid.

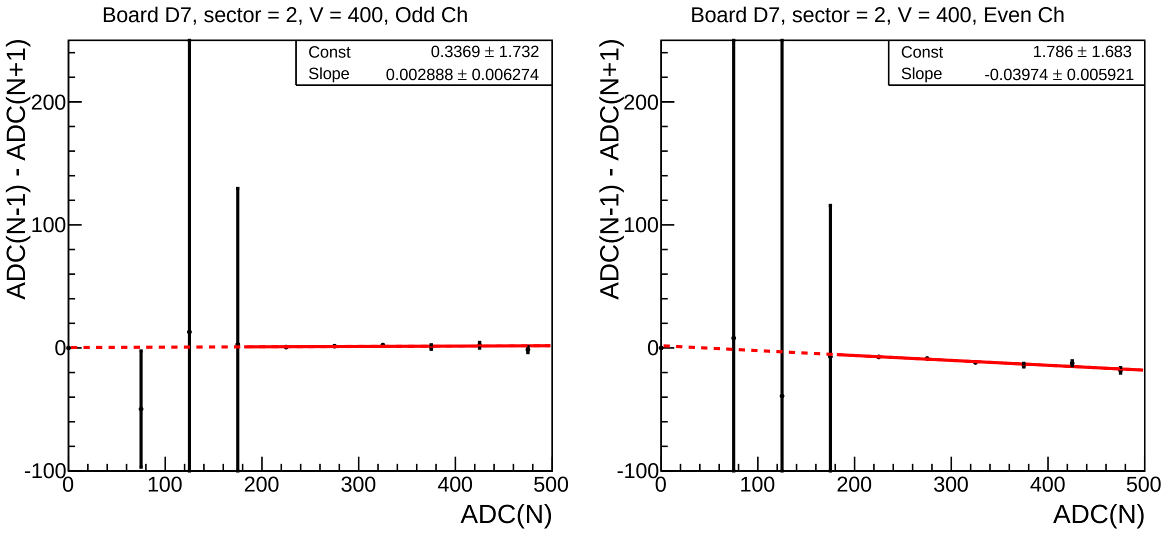

Figure 93: Graphs of $ADC(N-1) - ADC(N+1)$ versus $ADC(N)$, for (left) odd numbered Beetle channels and (right) even numbered Beetle channels, for Board D7, sector 2. A linear fit to each is overlaid.

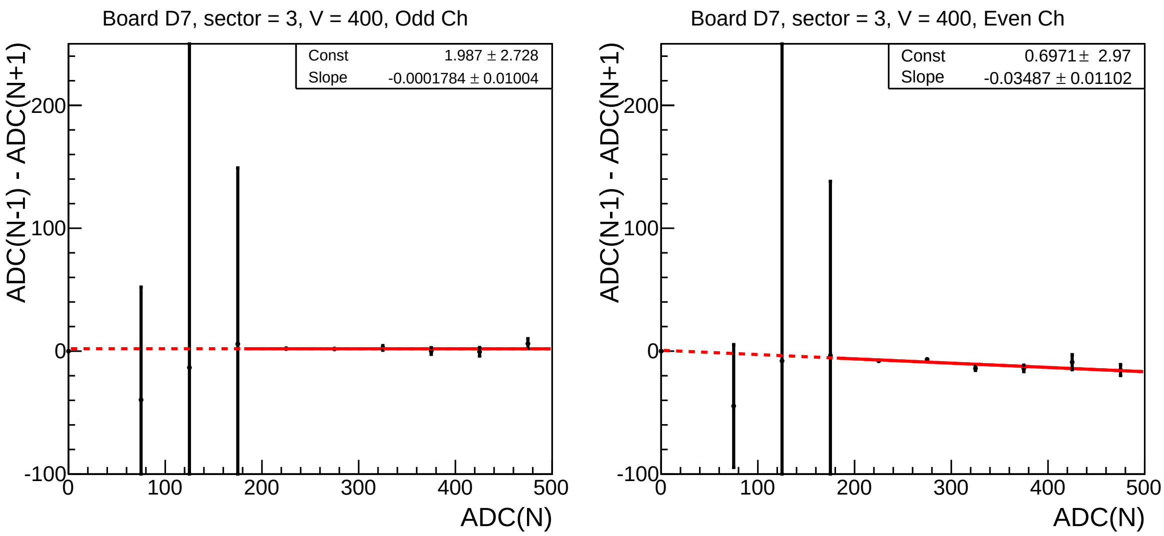

Figure 94: Graphs of $ADC(N-1) - ADC(N+1)$ versus $ADC(N)$, for (left) odd numbered Beetle channels and (right) even numbered Beetle channels, for Board D7, sector 3. A linear fit to each is overlaid.

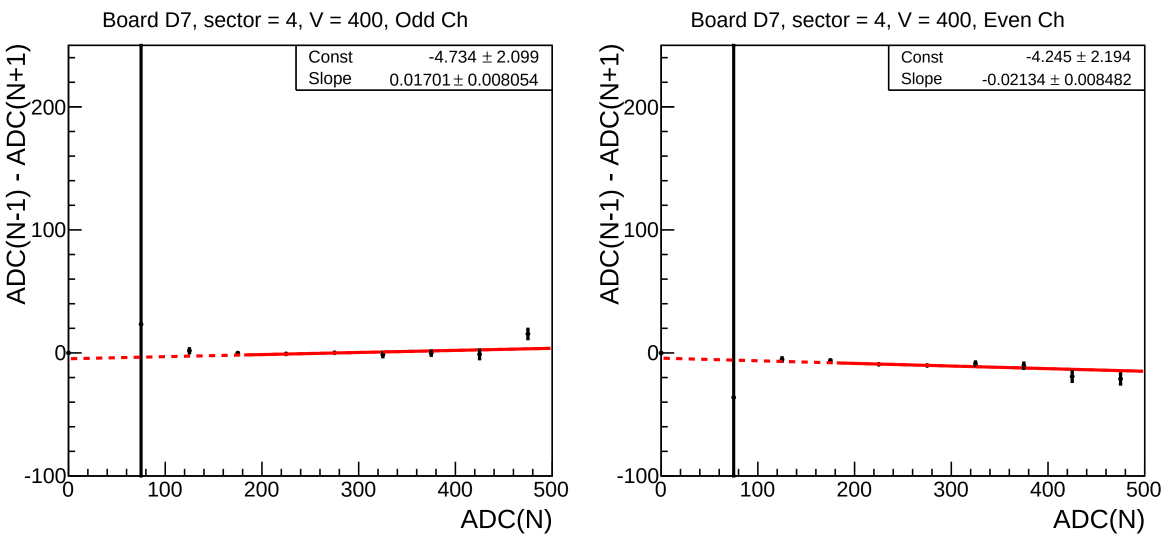

Figure 95: Graphs of $ADC(N-1) - ADC(N+1)$ versus $ADC(N)$, for (left) odd numbered Beetle channels and (right) even numbered Beetle channels, for Board D7, sector 4. A linear fit to each is overlaid.

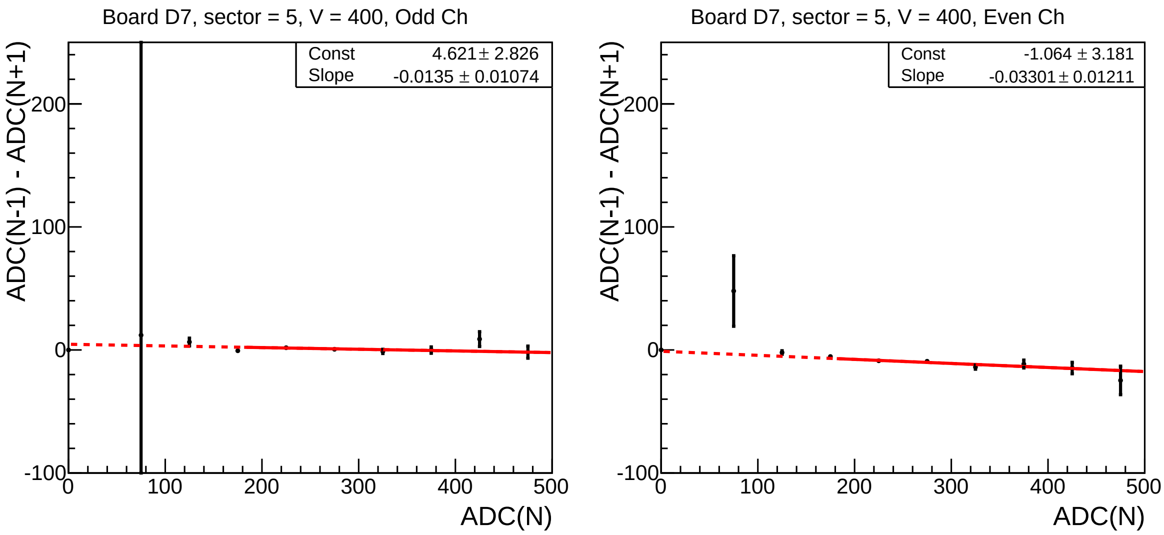

Figure 96: Graphs of $ADC(N-1) - ADC(N+1)$ versus $ADC(N)$, for (left) odd numbered Beetle channels and (right) even numbered Beetle channels, for Board D7, sector 5. A linear fit to each is overlaid.

References

[1] LHCb collaboration, *LHCb Tracker Upgrade Technical Design Report*, CERN-LHCC-2014-001. LHCb-TDR-015.

[2] A. Abba *et al.*, *Testbeam studies of pre-prototype silicon strip sensors for the LHCb UT upgrade project*, Nucl. Instrum. Meth. **A806** (2016) 244, `arXiv:1506.00229`.

[3] See Alibava systems web page at http://www.alibavasystems.com.

[4] J. Bernabeu *et al.*, *A portable telescope based on the ALIBAVA system for test beam studies*, Nucl. Instrum. Meth. **A732** (2013) 130.

[5] ALIBAVA Collaboration, R. Marco-Hernandez, *Development of a beam test telescope based on the ALIBAVA readout system*, JINST **6** (2011) C01002.

[6] More information about the IRRAD facility can be found at https://irradiation.web.cern.ch/irradiation/.

[7] For more information, see talks by S. Wonsak and M. Wiehe, at the 27^{th} RD50 Workshop, Dec 2–4, 2015. Talks are available at https://indico.cern.ch/event/456679/.

[8] Nuclear Instruments srl, IT-22045 Lumbrugo (CO), Italy, http://www.nuclearinstruments.eu/.

[9] A. Abba *et al.*, *Studies of pre-prototype sensors for the UT Upgrade project*, April, 2015. LHCb-PUB-2015-006.

[10] K. Akiba *et al.*, *The Timepix telescope for high performance particle tracking*, Nucl. Instrum. Meth. **A723** (2013) 47, `arXiv:1304.5175`.

[11] See Beetle manual http://www.kip.uni-heidelberg.de/lhcb/Publications/BeetleRefMan_v1_3.pdf.

[12] A. Chilingarov, *Temperature dependence of the current generated in Si bulk*, Journal of Instrumentation **8** (2013) P10003.

[13] M. Moll, *Radiation damage in silicon particle detectors*, tech. rep., DESY-THESIS-1999-040, 1999.